Exploring RE-MOFs with spn Topology and their Stimuli-Responsive Structural Properties

by

Felix Saraci

A thesis submitted to the Department of Chemistry and Biochemistry

Presented in partial fulfillment of the requirements for

the degree of Master of Science (Chemistry)

Concordia University

Montreal, Quebec

December 2020

CONCORDIA UNIVERSITY

School of Graduate Studies

This is to certify that the thesis prepared

By: Felix Saraci

Entitled: Exploring RE-MOFs with **spn** Topology and their Stimuli-Responsive Structural Properties

and submitted in partial fulfillment of the requirements for the degree of

Master of Science (Chemistry)

complies with the regulation of the university and meets the accepted standards with respect to originality and quality

Signed by the final examining committee:

Dr. Louis Cuccia____________________________Chair
Dr. Marek B. Majewski________________________Examiner
Dr. Rafik Naccache__________________________Examiner
Dr. Ashlee J. Howarth________________________Supervisor

Approved by ______________________ Graduate Program Director
Dr. Yves Gélinas

____________20_____ ________________________Dean of Faculty
Dr. Pascale Sicotte

Abstract

Exploring RE-MOFs with spn Topology and their Stimuli-Responsive Structural Properties

Felix Saraci

The work described herein explores an emerging class of metal–organic frameworks (MOFs) that are synthesized using rare-earth (RE) metals, known as RE-MOFs. In this work, these RE-MOFs are comprised of RE-hexanuclear clusters and tritopic organic linkers that give rise to a framework with **spn** topology. This thesis explores the (i) design, synthesis, and characterization of a yttrium (Y(III)) hexanuclear-cluster based RE-MOF, known as CU-45 (CU = Concordia University, experiment 45), (ii) the implementation of neodymium oxide (Nd_2O_3) precursors as templating agents, and (iii) the design, synthesis, and characterization of terbium and europium (Tb(III) and Eu(III)) MOFs with preliminary exploration of luminescence properties for potential sensing applications.

Chapter 2 explores the synthesis, characterization, and stimuli-responsive structural transformation of CU-45. CU-45, an achiral MOF, is exposed to various external stimuli including pressure, pH, temperature, and solvent, and in each case undergoes a phase transformation to give a chiral, RE-chain based MOF, known as Y-MOF-76. The physical and chemical properties of CU-45 and Y-MOF-76, as well as the underlying mechanism of the stimuli-responsive structural transformation is discussed.

Chapter 3 aims to address and improve the stability of CU-45, first by exploring a phenomenon known as lanthanide templating, which can facilitate the assembly and stabilization of lanthanide clusters. By adding a Nd_2O_3 precursor template to the CU-45 synthetic mixture, a phase pure MOF with improved crystallinity can be obtained. Furthermore, the effect of incorporating other rare-earth ions in CU-45, including Tb(III)- and mixed-metal Tb(III)/Eu(III)-CU-45, on stability is examined.

Acknowledgments

First, I would like to express my gratitude to my supervisor, Dr. Ashlee J. Howarth, for her unwavering support and accommodations to my academic and personal life through my time at Concordia. I am extensively grateful for the freedom she provides to explore collaborations, the opportunity to attend conferences and embark on individual research interests. Her devotion and pride in her scientific research is inspiring. Additionally, her selflessness in catering towards the research interests, motivations, and success of each Ph.D., M.Sc., and undergraduate students is tremendously admirable. I will always try to embody her passion, work ethic and optimistic character when approaching new professional and personal challenges and experiences.

I'd also like to thank my group members, Victor, Zvart, Hudson, and Paola, for providing a productive, friendly, and supportive work environment. Additionally, I'd want to thank Joey from the Majewski group for keeping me company during the morning shift, and Pedro from the Howarth group for all our insightful discussions, and our comradery. I look forward to seeing what you all accomplish in the near future.

I want to express my appreciation for Dr. Hatem M. Titi, using his relentless research ambition during my personal and collaborative work, providing insightful discussions, and a close friendship. Additionally, I would like to thank Dr. Robin Stein for her help with the SS-^{13}C NMR.

To my committee members, Dr. Marek B. Majewski and Dr. Rafik Naccache, thank you for providing valuable feedback and guidance with my research and encouraging me to have a more positive outlook!

I want to thank my wonderful partner, Fiona, for always providing me with endless support, compassion, and patience during my studies. Thank you for always being there for me, having a genuine interest in my work, and believing in my aspirations. Finally, I'd like to thank my mom and stepdad, Aurela and Andrew Nasedkin, for their continuous love and support during this time. My achievements today are only possible due to their continuous support and encouragement throughout my academic career.

Contribution of Authors

In all chapters, Dr. Ashlee J. Howarth acted in a supervisory role. Chapter 2 involved a collaboration with Dr. Hatem M. Titi and Dr. Robin Stein from the Department of Chemistry at McGill University in Montreal, Canada, and Dr. Mihails Arhangelskis from the Faculty of Chemistry from the University of Warsaw in Warsaw Poland.

Sections of Chapter 1 have been published as a review: Saraci, F.; Quezada-Novoa, V.; Donnarumma, P. R.; Howarth, A. J. *Chem. Soc. Rev.* **2020**, 2020, **49**, 7949-7977. I am a primary author of this work. Victor Quezada-Novoa and Rafael P. Donnarumma contributed to sections 1.3.3 and 1.3.1 respectively.

A version of Chapter 2 is pending submission to a peer-reviewed journal as: Saraci, F.; Titi, H.M.; Arhangelskis, M.; Howarth, A.J. *ChemRxiv,* **2020**, *Pending submission.* I am the primary author of this work. Dr. Hatem M. Titi performed all VT-PXRD experiments, and the single crystal X-ray structure analysis of Y-MOF-76. All ^{13}C and ^{19}F SS-NMR were performed by Dr. Robin Stein. All DFT calculations, and the Rietfeld refinement of CU-45 were performed by Dr. Mihails Arhangelskis.

Chapter 3 is currently a preliminary investigation. I am the primary author of this work. Dr. Hatem M. Titi provided Nd_2O_3 precursor material and performed TGA/DSC measurements.

Table of Contents

List of Figures

List of Tables

List of Abbreviations

(1-MCP)	1-methylcyclopropene
CD	circular dichroism
CH_3CN	acetonitrile
CPMAS	cross-polarization magic angle spinning
CU-45	Concordia University, experiment 45
DCM	dichloromethane
DFT	density functional theory
DMF	*N,N*-dimethylformamide
DRIFTS	diffuse reflectance infrared Fourier transform spectroscopy
DSC	differential scanning calorimetry
H_3BBC	1,3,5-tris(4'-carboxy[1,1'-biphenyl]-4-yl)benzene
H_3BTC	1,3,5-benzenetricarboxylic acid
H_3BTE	1,3,5-triscarboxyphenylethynylbenzene
KBr	potassium bromide
MBB	molecular building blocks
MOF	metal–organic framework
msx	topological code
N_2	nitrogen gas
Nd_2O_3	neodymium oxide
NMR	nuclear magnetic resonance spectroscopy
OMSs	open-metal sites
PSM	post-synthetic modification
PXRD	powder X-ray diffraction
RE	rare-earth
RE-MOF	rare-earth metal–organic framework
SALE	solvent assisted linker exchange
SBU	secondary building unit
$scCO_2$	supercritical CO_2
SCSC	single-crystal-to-single-crystal
scXRD	single crystal X-ray diffraction
SEM	scanning electron microscopy
spn	spinel topology
SS CD	solid state circular dichroism
SVP	SmartVac Prep
SS NMR	solid state nuclear magnetic resonance spectroscopy
TGA	thermogravimetric analysis
THF	tetrahydrofuran
VT-PXRD	variable temperature powder X-ray diffraction

Chapter 1

Introduction

1.1. Brief History of Metal–Organic Frameworks (MOFs)

The ability to construct coordination polymers using bridging carboxylic acid linkers of varying configurations with metal-ions of differing valency has been understood for many decades.[1–5] In 1965, Tomic reported preliminary findings that showed the influence of fluctuating metal valency (di-, tri,- and tetra-) on the thermal stability of resulting coordination polymers.[1] These findings demonstrate early examples of coordination materials with structural versatility, and variable stability.

Over 20 years after the initial work of Tomic was published, Hoskins and Robson explored the structural and chemical nature of what they termed scaffolding-like materials. In the initial findings by Hoskins and Robson, solid polymeric materials were produced by assembling metals and ligands, constructing three-dimensional (3D) frameworks with low densities and an array of cavities. Hoskins and Robson presented the synthesis and X-ray crystal structure of an infinite framework material constructed of tetrahedral centers linked together by rod-like units. The acetonitrile ligands in Cu^{I}-$(CH_3CN)_4^+$ were substituted with 4,4′,4″,4‴-tetracyanotetraphenylmethane to produce an infinite framework.[6] They determined that framework materials that can be deliberately designed and synthesized is feasible. Additionally, assembling these scaffolding-like materials for direct-use applications such as ion-exchange, molecular sieves, and catalysis was proposed.[6] This work established some basic design rules for the synthesis of infinite molecules with 3D-framework assembly and potential porosity.

Further exploration of these materials led to imperative contributions from Yaghi,[4,7,8] Férey,[9] and Kitagawa.[5] In the 1990s, Yaghi presented the capability to construct metal–organic porous frameworks hydrothermally.[7] Yaghi and Kitagawa further explored MOFs and their properties by investigating their ability to accommodate and bind with guest molecules.[5,8] Greater understanding of the porosity, surface area, crystallinity, and stability of these materials was obtained.[4] Férey explored the promising opportunities that framework materials possess, providing preliminary insight regarding the synthesis and structures of mesoporous MOFs and the potential application of these materials.[9] Furthermore, in the 1990s these materials were named metal–organic frameworks (MOFs), and have become a pillar in the field of materials chemistry.

MOFs are a class of crystalline inorganic-organic porous materials constructed by coordination between metal nodes (*e.g.* ions, chains, or clusters) and organic linkers (*e.g.* di-, tri-, tetra-, etc.). MOFs have been synthesized with metals from the s-,[10,11] p-,[12,13] d-,[14–16] and f-block[17,18] of the periodic table, with varying coordination numbers, geometries, and oxidation states. The organic linkers that are used are typically carboxylic acid or nitrogen-based aromatic compounds.[19] The two main components shown in Figure 1.1, demonstrate the assembly of inorganic metal nodes and organic linkers. These units come together in synthesis (See section 1.2.3) to form secondary building units (SBUs), which are molecular building blocks, that come together and assemble framework materials. The organic linkers behave as "struts" that bridge inorganic metal nodes, which acts as "joints" in the framework architecture.[20]

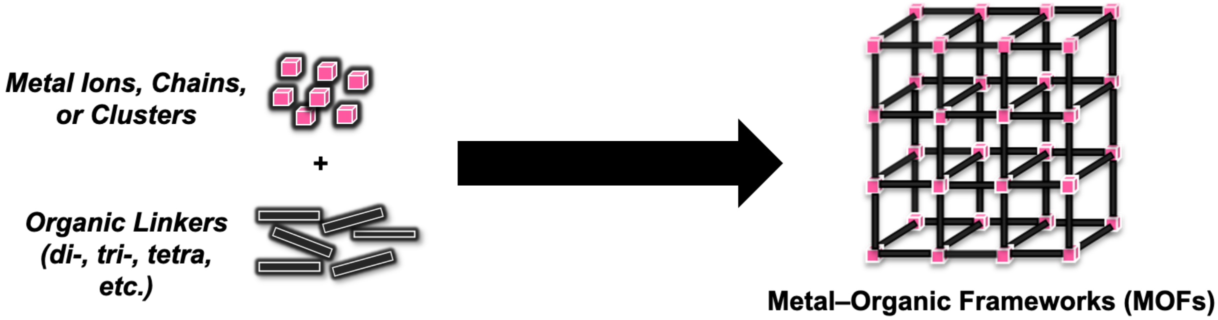

Figure 1.1. Schematic representation of assembling a metal–organic framework (MOF).

The seemingly endless variety of inorganic nodes and organic linkers alongside the foundation of reticular chemistry, gives rise to almost limitless possibilities for synthesizing MOFs. On account of their above-mentioned properties, MOFs have established tremendous potential in various applications that include but are not limited to gas adsorption,[21–23] catalysis,[24–26] water treatment,[27–29] drug delivery,[30,31] bioimaging,[32,33] and temperature[34] and chemical sensing.[35,36] Currently, there are two commercial applications of MOFs developed by NuMat Technologies,[37] and MOF Technologies,[38] which have demonstrated the potential of these materials. NuMat launched ION-X, which integrates MOFs for the storage and release of highly toxic gases, utilizing a low-pressure storage platform and providing a safety barrier for the handling of dangerous and toxic gases. MOF Technologies released a product known as TruPick, which utilizes a MOF as an adsorbent for the storage and release of 1-methylcyclopropene (1-MCP). 1-MCP is a competitive inhibitor for a ripening receptor found on some fruit and thus slows down the ripening process.

1.2. Fundamental Principles and Properties of MOFs

1.2.1. Reticular Chemistry

Introduced by Yaghi and O'Keefe,[39,40] reticular chemistry is the foundation of MOF synthesis, and is defined as the design and process of assembling rigid molecular building blocks (MBBs) into predetermined crystalline structures (*i.e.* networks) that are held together via strong bonding.[39,41] Reticular chemistry is considered as a logical approach to synthesizing an extensive class of complex crystalline materials with high surface area, porosity, stability, and structural tunability. Therefore, a strong understanding of coordination chemistry is needed when considering the geometry and connectivity of the building blocks required to generate pre-designed network structures. Additionally, understanding network topology is of utmost importance, as different network topologies have their own arrangements of vertices and edges that can yield an endless number of structures.[42] A topology is not affected by bond deformations such as stretching, bending, or squeezing, and is therefore ideal for describing MOF structure. The foundation of reticular chemistry relies on there being numerous building blocks that can build the same network structure, and which can be manipulated to have the same, or similar, geometry and connectivity, regardless of size.[43]

1.2.2. Characteristics and Properties of MOFs

MOFs are a promising class of multi-dimensional crystalline materials with properties that can include ultrahigh porosity (up to 90 % free volume),[44] high surface area (up to 7800 m^2/g),[45] low density (down to 0.124 g/cm),[46] structural tunability, and stability.[47] As a consequence of these properties, MOFs can be distinguished from related materials such as zeolites, and 1-D coordination polymers.[48] Currently, the exploration of MOFs assembled using rare-earth (RE) metal nodes has garnered much interest.[49–51] RE elements include yttrium, scandium, and the series of fifteen lanthanides. The term rare-earth" is used throughout this thesis to encompass all of these elements since the work encompasses lanthanides and yttrium.

1.3. Rare-Earth Metal–Organic Frameworks (RE-MOFs)

One subset of MOFs that are of interest from both a fundamental synthetic, and application standpoint are those assembled using RE metal nodes.[49–51] RE-metals include the series of fifteen lanthanides as well as yttrium and scandium (Figure 1.2). The coordination chemistry of RE-metals is very diverse, with only small energetic differences between different coordination numbers and geometries, and where geometry is dictated primarily by ligand steric effects.[52]

In contrast to d-block metals, RE-metals have unique electronic properties due to their 4f electron configurations.[53] Given that the 4f orbitals are buried below the 5s and 5p orbitals and shielded from their external environment, RE-metals have distinct electronic and magnetic properties that are not significantly altered by coordinating ligands.[53] While these properties can lead to difficulty in predicting MOF structures, it also opens the door for the discovery of several new and intricate structures, comprised of diverse metal-nodes, and in some cases giving rise to highly connected networks with the further capability to merge multiple network structures using only one metal.[21,54] By carefully tuning the RE-metal node and organic linker components, RE-MOFs can be assembled into fascinating structures with diverse and complex topologies, presenting endless possibilities for the development of functional materials. Herein, a brief overview of RE-MOFs is presented, classified by the identity of the RE-metal node (ions-, chains-, or clusters).

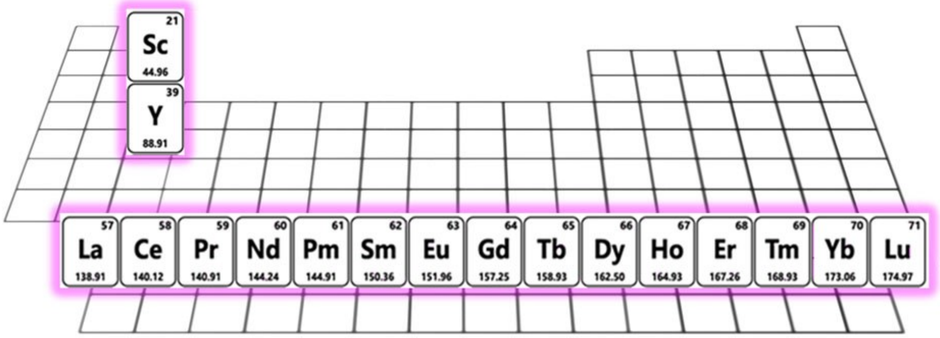

Figure 1.2. Periodic table highlighting the rare-earth (RE) elements.

1.3.1. RE-Metal Ion Nodes

Amongst the plurality of structures that a MOF can present, those comprised of metal-ion nodes are among the simplest from the perspective of the inorganic structural unit. Unlike s-, p-, and d-block metal ions, f-block metal ions possess high coordination numbers as well as numerous coordination modes, unlocking a variety of structures that are not accessible using the former.[55–61] Although RE-MOFs with metal-chain nodes (Section 1.3.2) and metal-cluster nodes (Section 1.3.3) are more prevalent in literature, there are several reported examples describing structures in which metal-ion nodes are observed.

Early on, Loeb *et al.* reported the synthesis of a series of RE-MOFs (RE = Sm(III), Eu(III), Gd(III), Tb(III), Yb(III)) comprised of rotaxane linkers and RE(III)-ion nodes, resulting in a high volume cage (10 000 Å^3) albeit partially filled with an interpenetrating net.[62] The structure obtained was found to depend on the identity of the RE(III), which adopts coordination number 7 (Yb(III)) or 8 (Sm(III) , Eu(III), Gd(III) and Tb(III)). All MOFs in the series showed similar thermal stability up to 240 °C, and PXRD patterns for the desolvated MOFs demonstrate retention of the structure, though porosity was not experimentally measured. Another MOF with RE(III)-ion nodes and large cages (UTSA-61), was reported by He, Chen *et al.* in 2013.[63] UTSA-61 is a mesoporous MOF with **hey** topology comprised of large octahedral cages (2.4 nm in diameter) and synthesized using a dendritic hexacarboxylic acid linker (Figure 1.3). Despite having an exceptionally long linker, no interpenetration is observed in UTSA-61. These two examples highlight the use of large, sterically bulky linkers to give RE-MOFs comprised of RE(III)-ion nodes.

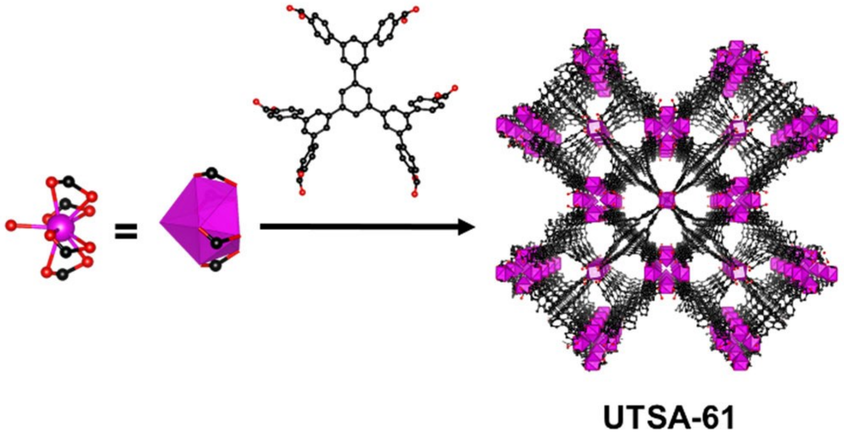

Figure 1.3. Structure of UTSA-61(Tb), highlighting the Tb(III)-ion node and hexacarboxylic acid linker. Tb = pink, C = black, O = red. Hydrogen atoms omitted for clarity.

1.3.2. RE-Metal Chain Nodes

Rare-earth-oxo/hydroxo chain nodes, also called rods,[64] (Figure 1.4) have been found for several RE-MOFs comprised of carboxylic acid linkers.[65–69] The formation of dimeric and polymeric RE-oxo/hydroxo chains tends to be favoured in the presence of bridging carboxylic acid ligands,[70] particularly if the ligand does not contain ortho substituted directing groups that can act to control hydrolysis of the RE-metal precursor.[71–73]

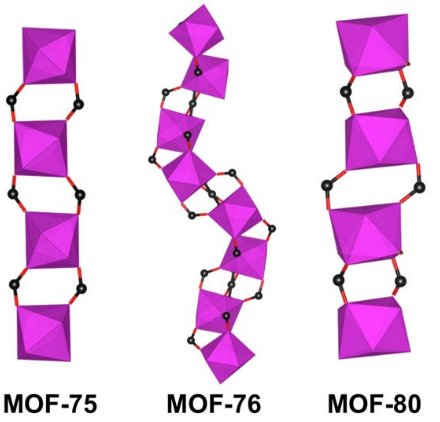

Figure 1.4. Example of rare-earth-oxo/hydroxo chain nodes observed in MOF-75, MOF-76, and MOF-80. RE = pink, C = black, O = red.

In 1998, the first examples of open coordination networks comprised of carboxylic acid linkers and RE-chains were reported.[74,75] Michaelides *et al.* demonstrated a 3D network comprised of La(III) and flexible ditopic adipic acid linkers, to give $La_2(adipate)_3(H_2O)_4]\cdot 6H_2O$.[75] While this structure contains pores approximately 7 x 8 Å in size, evacuation (or dehydration) of the network resulted in a nonporous phase. In another example, Férey *et al.* reported a network comprised of RE(III)-chains linked by flexible ditopic glutaric acid linkers.[74] The structure, named MIL-8, is comprised of edge-sharing $REO_8(H_2O)$ polyhedra, and isostructural derivatives were reported using Nd(III), Pr(III), Sm(III), Eu(III), Gd(III), Dy(III), Ho(III), and Y(III). Although the structure of MIL-8 is open, with channel dimensions of 3 × 5 Å, the porosity of these materials was not experimentally demonstrated. Linkers with higher connectivity can also be used to create open frameworks with enhanced porosity. For example, O'Keeffe, Yaghi *et al.* reported MOF-76, a structure comprised of 1,3,5-benzenetricarboxylic acid linkers (BTC) and helical Tb(III)-chains

(Figure 1.5).[10] Owing to the helical SBU connected by tritopic linkers, MOF-76 forms a complex, open structure with **msx** topology, and a Langmuir surface area of 335 m^2/g after activation at 200 °C under vacuum.

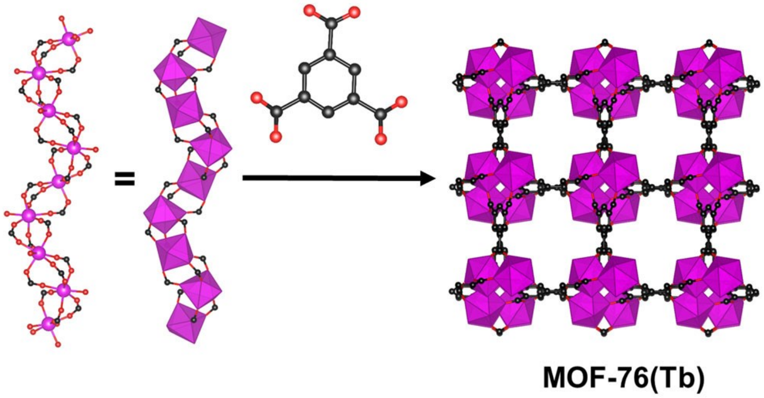

Figure 1.5. Structure of MOF-76(Tb), highlighting the Tb(III)-chain node and 1,3,5-benzenetricarboyxlic acid linker. Tb = pink, C = black, O = red. Hydrogen atoms omitted for clarity.

1.3.3. RE-Metal Cluster Nodes

Significant research effort has been devoted to the synthesis and isolation of discrete, polynuclear RE-oxo/hydroxo clusters.[71–73] In all cases, controlled hydrolysis of the RE precursor is required to ensure the synthesis of clusters as opposed to RE-chains, oxides, and hydroxides. Controlled hydrolysis can be achieved using ligands, which can act as structure directing agents (or modulators) but also as capping groups to stabilize the cluster. These same clusters can be generated and stabilized during the synthesis of RE-MOFs, functioning as SBUs for a wide range of structures. Currently, there are numerous reported examples of RE-cluster MOFs that are composed of di-,[61,76–83] tri-,[84–90] tetra-,[91–97] hexa-,[17,21,98–105] hepta-,[106,107] and nonanuclear[21,108–111] clusters and beyond; however, the work encompassed in this thesis, focuses exclusively on MOFs comprised of RE-hexanuclear clusters.

1.3.3.1. RE-Hexanuclear Cluster MOFs

The potential of RE(III)-hexanuclear clusters to be used as SBUs in MOFs was shown by Yao *et al.* in 2008.[98] In this example, the octahedral unit $[Er_6(\mu_6\text{-}O)(\mu_3\text{-}OH)_8]_8^+$ is repeated in one direction to achieve a rod shaped structure, giving a hybrid between a RE(III)-chain and RE(III)-cluster node (Figure 1.6a). Later, in a similar example published by Almeida Paz, Rocha *et al.* the hexanuclear cluster $Pr_6(\mu_3\text{-}O)_2(\mu_3\text{-}OH)_6$ was found to be interconnected to other clusters through a single Pr(III) ion, creating another hybrid RE(III)-chain/cluster node (Figure 1.6b).[99] In both examples discussed above, the linkers used (3-hydroxy-pyrazine-2-carboxylic acid, and 2,5-pyridinedicarboxylic acid) contain a pyridine nitrogen adjacent to the carboxylic acid, but no other modulator was used to control the formation of the cluster. Recognizing the similarities between RE(III)-hexanuclear clusters and the Zr(IV)-hexanuclear clusters used as SBUs in several MOFs since 2008 (Figure 1.7),[102] Eddaoudi *et al.* reported a series of isoreticular RE(III)-MOFs with **fcu** topology.[17]

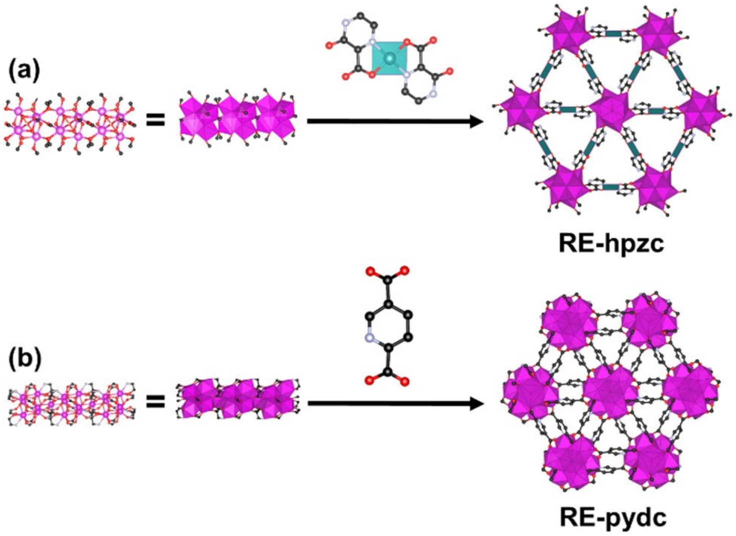

Figure 1.6. Structure of a) RE-hpzc highlighting the hexanuclear Er(III)-cluster node and 3-hydroxy-pyrazine-2-carboxylic acid linker; b) RE-pydc highlighting the hexanuclear Pr(III)-cluster node and 2,5-pyridinedicarboxylic acid linker. Er and Pr = pink, C = black.

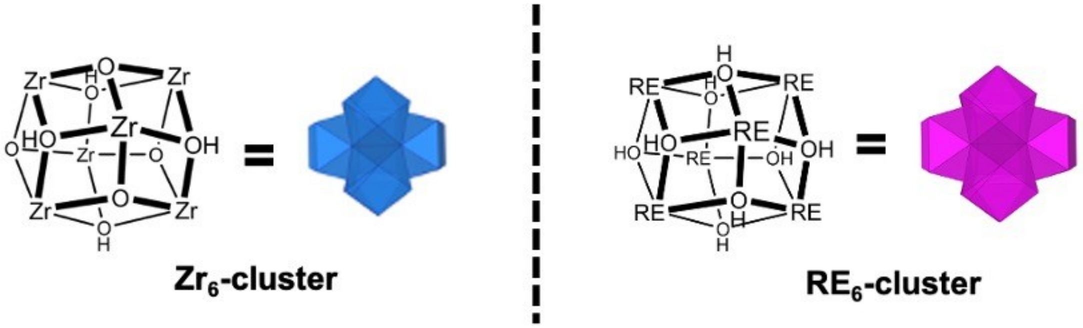

Figure 1.7. Comparison of Zr(IV)- hexanuclear cluster and RE(III)-hexanuclear clusters. Zr = blue, RE = pink.

Using their molecular building block (MBB) approach, seven Y(III) and Tb(III)-MOFs comprised of linear fluorinated and nonfluorinated, homo and heterotopic linkers were reported (Figure 1.8). For example, using 2-fluoro-4-(1H-tetrazol-5-yl)benzoic acid (FTZB) as a linker, the metal cluster [RE$_6$(μ_3-OH)$_8$(O$_2$C-)$_6$(N$_4$C-)$_6$] (RE = Y(III) and Tb(III)) is generated and serves as a 12-connected node, leading to the first RE(III)-MOFs with **fcu** topology. The MOFs, with structures analogous to Zr-based UiO-66, and UiO-67 display BET surface areas of 1200-1300 m^2/g.

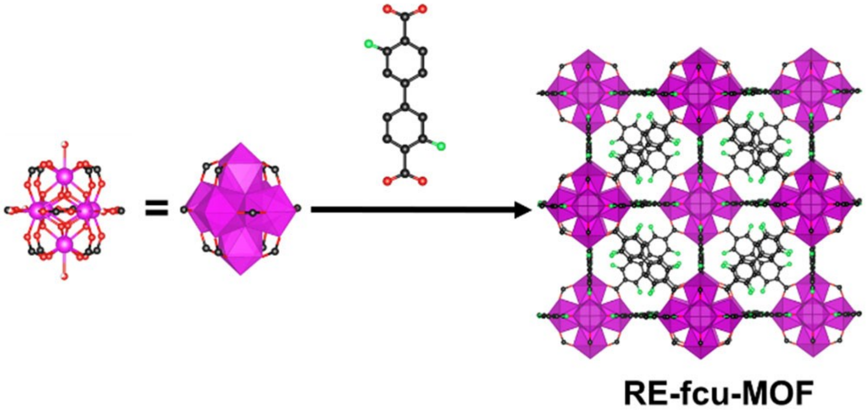

Figure 1.8. Structure of RE-**fcu**-MOF, highlighting the hexanuclear RE(III)-cluster node (RE = Y(III), and Tb(III)) and 3,3′-difluorobiphenyl-4,4′-dicarboxylic acid linker. RE = pink, C = black, O = red, F = lime green. Hydrogen atoms omitted for clarity.

Eddaoudi *et al.* have since gone on to report other examples of RE(III)-MOFs with **fcu** topology, comprised of RE(III)-hexanuclear cluster nodes (RE = Y(III), Sm(III), Gd(III), Tb(III), Dy(III), Ho(III), Er(III)) bridged by fumaric acid, or 1,4-naphthalenedicarboxylic acid.[21,103,104] In all cases, 2-fluorobenzoic acid was used as a modulator to drive the formation of the hexanuclear cluster node. Furthermore, Eddaoudi *et al.*, and later Hong, Li *et al.* showed that through the use quadrangular tetratopic linkers, RE(III)-MOFs comprised of the same 12-connected hexanuclear cluster node but with **ftw** topology could be made with Y(III), Tb(III) or Yb(III), again with the addition of 2-fluorobenzoic acid.[105,112]

In an example highlighting the power of the MBB approach, Eddaoudi *et al.* reported a series of MOFs with novel **sph** topology (Figure 1.9).[54] The topology was designed by merging two known topologies, **spn** (3,6-connected), and **hxg** (6-connected) to give a highly complex 3,6,12-connected topology, that the authors named **sph**. The series of Tb-**sph**-MOFs is comprised of 12-connected Tb(III)-hexanuclear cluster nodes, bridged by tritopic and hexatopic linkers (or in some cases tritopic linkers that can pack to form a 6-connected unit).

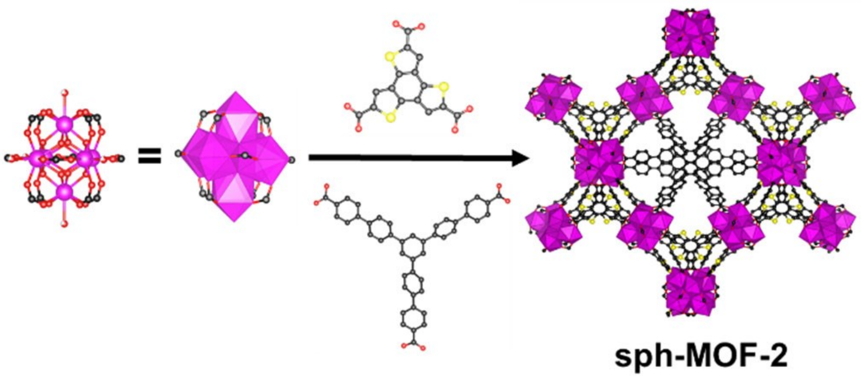

Figure 1.9. Structure of **sph**-MOF-2, highlighting the hexanuclear Tb(III)-cluster node and benzotristhiophene carboxylate and 4,4′,4″-(benzene-1,3,5-triyltris(benzene-4,1-diyl))tribenzoate linkers. Tb = pink, C = black, O = red, S = yellow. Hydrogen atoms omitted for clarify.

The Tb-**sph**-MOFs have two pores, a larger truncated tetrahedral cage (6.5 – 22 Å) and smaller tetrahedral cages (2.5 – 9.5 Å) with sizes corresponding to the size of the organic linkers used to build the framework. Upon activation, the Tb-**sph**-MOFs showed BET surface areas ranging from 1020 – 2170 m^2/g as measured by Ar adsorption.

1.4. Overview of Methods in MOF Synthesis

There are several synthetic techniques that produce MOFs, which include solvothermal,[1–3] hydrothermal,[7,116,117] electrochemical,[118,119] sonochemical,[120] mechanochemical,[121–123] and microwave assisted synthesis.[124] Additionally, if MOF thin-films are required, layer-by-layer deposition, liquid phase epitaxial growth, or seed growth can be utilized.[125]

The MOFs reported in this thesis, are synthesized predominantly using solvothermal synthetic methods. Solvothermal synthesis uses high boiling point solvents (*e.g.* DMF, DEF, or DMSO) alongside metal-salt and organic linker precursors mixed together in a screw-top vial. Typically, in this method, the reaction mixture is heated on a hot-plate or placed in an oven at high temperature with reaction times ranging from hours to days. Challenges arise when performing solvothermal synthesis, as the smallest variance in reaction conditions can alter the quality of the MOF produced; therefore, many parameters need to be considered and optimized, which may include: (i) time, (ii) temperature, (iii) reagent concentration, (iv) solvent polarity, (v) solvent volume, (vi) pH, (vii) presence of stirring, and (viii) the general nature of materials used.[113,126] As such, these parameters may not only affect the network structure and topology of the material but also possibly change the particle size, morphology, and phase purity.

The conditions used for MOF synthesis must give rise to a dynamic process. Dynamic bonds are essential for MOF synthesis, as they facilitate the assembly of crystalline and ordered materials. The occurrence of any errors in bonding can cause disorder or structure termination. In general, synthetic methods should be chosen to facilitate the organic linker and metal node to form a bond, break a bond, and reform, driving structure propagation.[26] In many cases, when the bonds between the metal-linker are very strong, non-structural monotopic ligands are used (*i.e.* modulators) that can be used to make the process dynamic, and thus prevent rapid precipitation of amorphous material.[127,128] These modulators (*e.g.,* benzoic acid, acetic acid, hydrochloric acid, and trifluoroacetic acid) can compete and form dynamic bonds with the metal precursor material to facilitate a slower formation of structural bonds, through competition with the linkers for metal-coordination sites.

1.4.1. Activation of MOFs

The final step in MOF synthesis is the process called activation, which is required for harnessing the permanent porosity of MOFs. Activation involves removing any guest molecules (*i.e.* solvent or other non-structural molecules) from the MOF without compromising structural integrity or porosity of the framework.[129] The strategies for removing guest molecules include (i) conventional heating and vacuum; (ii) solvent-exchange; (iii) supercritical CO_2 ($scCO_2$) drying, (iv) freeze drying, and (v) chemical treatment.

1.4.2. Conventional Activation

Conventional activation is the removal of guest molecules through the combination of applying heat and vacuum.[129] Although this method has been extensively used, it demonstrates minimal effectiveness for obtaining the full porosity for many MOFs.[129] Due to capillary forces and surface tension generated as solvent molecules pass through the liquid-to-gas phase boundary,[126,129] framework collapse can occur during activation. Therefore, more intricate and efficient activation strategies are needed to circumvent these concerns and achieve permanent porosities and high surface areas.

1.4.3. Solvent-Exchange Activation

To circumvent challenges arising from reaction solvent surface tension and strong capillary forces, solvent-exchange can be used.[126,129] Solvent-exchange involves exchanging the high boiling point and high surface tension reaction solvent (*i.e.* DMF, water), with solvents that have lower surface tension and higher volatility (*i.e.* chloroform or acetone). Solvent exchange is typically followed by conventional activation methods involving heat and vacuum treatment. The use of lower boiling point solvents is an effective strategy, as milder temperatures can then be used during the conventional activation stage. Solvents with lower surface tension are also required to minimize the severity of capillary forces acting on the MOF pores during solvent removal. Although, solvent-exchange is the preferred method of activation in many cases, there are instances when MOFs activated using this method demonstrate lower than anticipated porosities and surface areas.[130] In these cases, alternative methods of activation should be implemented.[131]

1.4.4. Supercritical CO_2 ($scCO_2$) Activation

In some instances, supercritical CO_2 ($scCO_2$) is employed for activating MOFs.[131,132] $scCO_2$ is non-toxic and considered more "green", is cost competitive, and scalable, providing a an alternative to activating MOFs. The benefit to using supercritical fluid is that the solvent exchange is much more mild, as it avoids the liquid- to gas- phase transformation, and directly goes to the supercritical phase avoiding issues with surface tension and capillary forces.

Similar to solvent-exchange, $scCO_2$ drying involves multiple solvent-exchange steps. First, the MOF undergoes a conventional solvent exchange with a solvent that is miscible with liquid CO_2 (*i.e.* ethanol) and soaked overnight. Then, the MOF is placed in the $scCO_2$ dryer and cooled (*ca.* 2-10 °C), where several solvent exchanges with liquid CO_2 occur. Following the final exchange, the MOF is heated to the supercritical temperature and pressure of CO_2 (*e.g.* 31 °C and 73 atm), and supercritical CO_2 is slowly released (*i.e.* "bleeding") from the MOF. Afterwards, the MOF should be placed under vacuum and moderate temperatures to remove any residual CO_2 from the activation procedure.

1.5. Characterization of MOFs

Due to their diverse structural and chemical properties, several characterization techniques are used to understand the features of a MOF. The characterization techniques used in this thesis include: (i) powder X-ray diffraction (PXRD) to establish phase purity and crystallinity of a MOF; (ii) single crystal X-ray diffraction (scXRD) to obtain the absolute structure; (ii) nitrogen (N_2) adsorption and desorption isotherms to measure surface area and porosity; (iii) thermogravimetric analysis (TGA) to study thermal stability and determine chemical formula; (iv) scanning electron microscopy (SEM) to obtain particle size and morphology; (vi) NMR spectroscopy to determine bulk purity and linker-to-linker or linker-to-modulator ratios; (vii) diffuse reflectance infrared Fourier transform spectroscopy (DRIFTS) to measure the presence or absence of IR-active functional groups in the framework, and; (viii) circular dichroism (CD) spectroscopy to study the chiral character of a MOF sample. Each technique, in the context of MOF characterization, is discussed below.

1.5.1. Powder X-ray Diffraction (PXRD)

PXRD is a powerful technique used to obtain information about crystalline structure and crystallite characteristics. As one of the most important fundamental techniques used for MOF characterization, PXRD is used to determine bulk crystallinity and topology. If a MOF is deemed crystalline, further information may then be extracted from the PXRD pattern.[126,133,134] For instance, structural topology, and phase purity can be discerned by comparison to simulated patterns generated from single crystal data obtained experimentally, or *in-silico.*

Typically, a PXRD experiment involves loading a powdered sample onto a sample holder that contains a plate of material (*e.g.* plate = plastic, glass, or aluminum), and samples are either dry loaded or transferred using volatile solvents or oil.[126] When preparing crystalline samples for analysis, it is important to remember that depositing powders on a flat substrate may result in crystallites packing in a preferred orientation. As a result, different PXRD patterns may be generated based on the calculation that assumes that crystallites are in random order. Additionally, reflection intensities may be different in experimental versus simulated patterns.

To circumvent this, the sample, should be continuously rotated throughout the duration of the experiment. By variable rotation, the crystallite orientation will become nearly random in relation to the incoming X-rays and the detector. PXRD is crucial when designing and assembling novel MOFs. For instance, as shown in Figure 1.10, PXRD can be used to determine that CU-45 (CU = Concordia University; 45 = Experiment 45) is isoreticular (isostructural) to the Zr(IV)-based MOF-808.

Although challenging, full crystal structure determination of unknown materials can be extracted from powder diffraction data. This method can be divided into three main stages: (i) indexing (unit cell determination) and space-group assignment (symmetry determination); (ii) solving the structure; and (iii) structure refinement.[133] These three main stages use peak positions and diffraction maxima intensities to adequately solve the desired crystal structure.

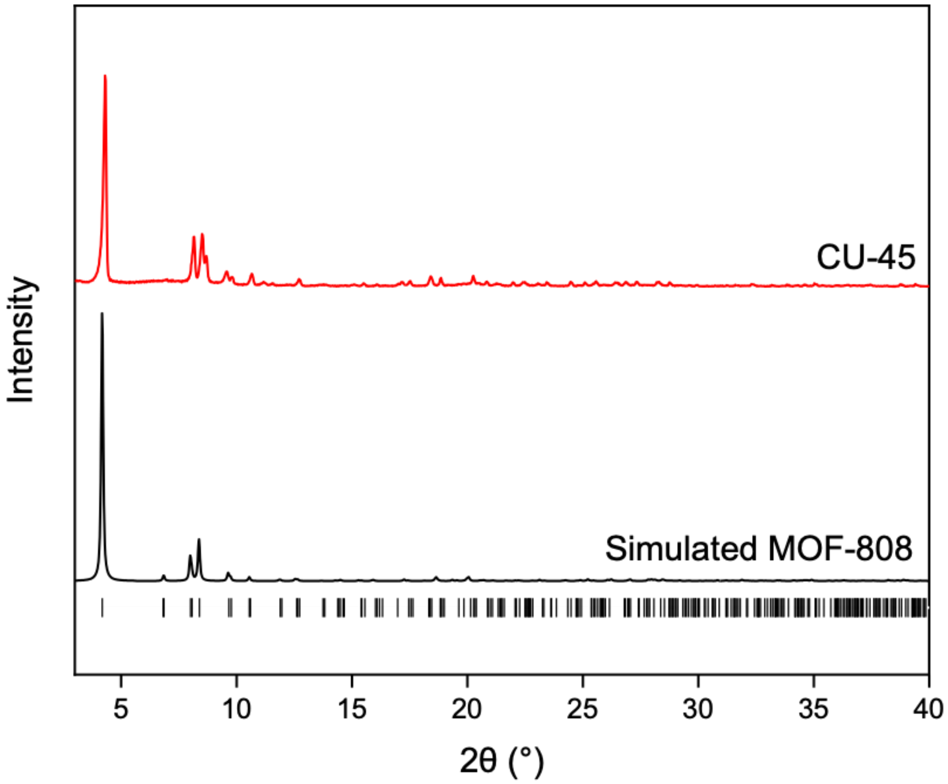

Figure 1.10. PXRD pattern of CU-45 synthesized *de novo* and simulated MOF-808.

1.5.2. Single Crystal X-ray Diffraction (scXRD)

In comparison to PXRD which probes the bulk, scXRD is used to determine the absolute structure of a MOF single crystal. However, it is very challenging to obtain a single crystal of the appropriate crystal size (> 50 μm) and quality. To overcome these challenges, reaction parameters and conditions for MOF synthesis need to be adjusted to facilitate the formation of crystals. Additionally, when a crystal of adequate quality and size is obtained, it is important to perform other characterization techniques to ensure the single crystal sample matches the bulk MOF material.

Differences between higher and lower temperatures may produce variation in the diffraction data collected for a MOF. Depending on the temperature, solvent molecules may freely move (highly disordered) and may not contribute much to diffraction peaks.[135] Some challenges arise due to the structural features a MOF entails, in which symmetry mismatches may occur between the lattice of the nodes and the lattice of the organic linkers. This is due to differences in the amount of symmetry in the respective lattice regions.[126] As a result, single crystal XRD for MOFs may be very challenging, although, tremendously rewarding.

1.5.3. Nitrogen (N_2) Adsorption and Desorption Isotherms

To determine the pore size, pore volume, and surface area of a MOF, gas (N_2) adsorption and desorption isotherms can be used. Prior to performing gas adsorption and desorption isotherms, it is necessary for MOFs to be thoroughly activated (see Section 1.4.1) to obtain sufficient data. N_2 adsorption isotherms for nonreactive gases at cryogenic temperatures (*i.e.* 77 K) can be used to determine pore volume, pore size distribution, and surface area of a MOF. Nitrogen gas at 77 K is the standard adsorbate for surface area and pore size analysis, [136] and has a permanent quadrupole moment, meaning the ability to form well-defined monolayers on most surfaces.

Gas adsorption analysis is based on physisorption, which is when an absorbable gas (*e.g.* N_2) is brought in contact with the surface of the solid (the adsorbent) and forms weak interactions.[136,137] Pore sizes are classified as: (i) micropores (less than 2 nm); (ii) mesopores (between 2 and 50 nm); and (iii) macropores (greater than 50 nm). Isotherms provide valuable information based on their shape (Figure 1.11), classified as:[137] (i) Type I – given by microporous solids, which is further subcategorized as Type I(a), given by materials with mainly narrow micropores (less than 1 nm), and Type I(b), given by materials with larger micropores or small mesopores; (ii) Type II – given by materials with macropores or those which are nonporous; (iii) Type III – presents no identifiable monolayer formation, due to weak adsorbent-adsorbate interactions which are typically found on the surface of macroporous or nonporous materials; (iv) Type IV – given by mesoporous materials with capillary condensation, which is further subcategorized as Type IV(a), given by materials with cylindrical pores greater than 4 nm, and Type IV(b) for mesopores less than 4 nm; (v) Type V – similar to type III, however, pore filling occurs at higher relative pressure; (vi) Type VI – is given by nonporous materials that have uniform layer-by-layer adsorption.

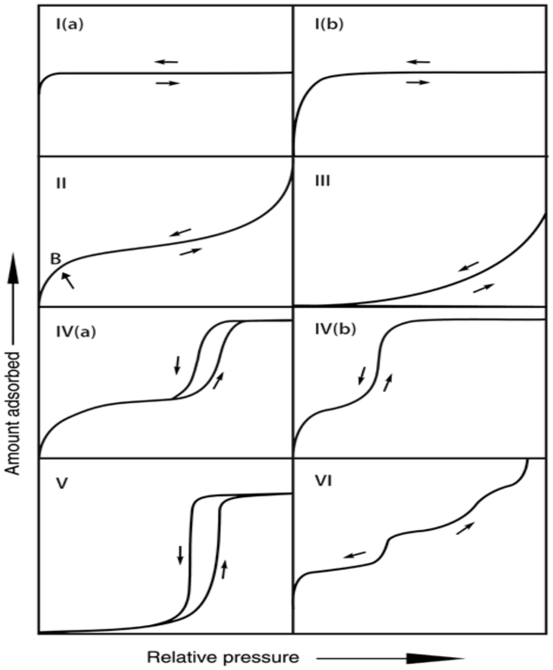

Figure 1.11. General representation of known examples for physisorption isotherms. Figure obtained from Thommes *et al*.[137]

In order to adequately calculate the surface area (m^2/g) of a MOF from a gas adsorption isotherm, it is best to use BET theory. In general, BET theory predicts the number of molecules required to be adsorbed on a surface to form a monolayer, even though a monolayer may never form during the gas adsorption experiment.[138] In contrast to BET theory, Langmuir theory assumes perfect adsorption and formation of a monolayer before multilayer adsorption occurs, and can therefore only be used to fit Type I isotherms.[139] Similar to surface area calculations, pore size distribution and pore volume of MOFs can be extracted from the N_2 isotherm data. There are various models that can be applied to determine these properties of MOFs, which include the non-local density functional theory (NLDFT) method,[140] Barrett-Joyner-Halenda (BJH) method,[141] and others. For MOFs, the NLDFT method is the most widely used and accepted model as it can be used to accurately fit isotherm data corresponding to mesopores and micropores.

1.5.4. Thermogravimetric Analysis (TGA) and Differential Scanning Calorimetry (DSC)

Thermogravimetric analysis (TGA) is a technique that can be used to measure the thermal stability of a MOF, determine the weight percent loss of guest molecules and linkers, measure solvent-accessible volume, and assist in determining the molecular formula of a MOF. In general, TGA measures the change in sample weight as a function of increasing temperature under a carrier gas (*e.g.* air, N_2, or O_2). Depending on the carrier gas used, different decomposition pathways can be observed for MOFs.[142] In some instances, a TGA apparatus may be equipped with a differential scanning calorimetry (DSC) device, which measures the heat required to increase the temperature of a sample, as a function of heat and time. Generally, one can use both a TGA/DSC technique to measure the thermal stability and how physical properties of a material change as a function of temperature and time.[143]

1.5.5. Scanning Electron Microscopy (SEM)

Scanning electron microscopy (SEM) is a powerful technique that can be used to measure MOF particle size and crystal morphology. Most MOFs are insulating materials, which can lead to image artifacts such as charging effects that arise from strong electron interactions within the MOF.[144] Additionally, the acceleration voltage of the electron beam, if too high, can dramatically change the MOF sample, damaging or potentially breaking the crystals. Generally, the most common method used to circumvent these issues is to coat the MOF sample with a conducting material (*i.e.* gold), that helps to decrease the charge build up in the MOF from the electron gun. Since MOF samples are most likely found as powdered materials, the samples are loaded onto an SEM sample holder using double-sided carbon tape. In addition to observing the physical characteristics of the crystallites, information regarding the elemental composition can be obtained, particularly when coupled with an energy-dispersive X-ray spectroscopy (EDS) detector.

1.5.6. NMR Spectroscopy

1.5.6.1. Solution-State NMR Spectroscopy

Due to their insolubility, MOFs cannot not be characterized by traditional NMR spectroscopy methods. In general, performing NMR spectroscopy analysis on a MOF requires digestion, which is most commonly achieved by adding deuterated sulfuric acid (D_2SO_4) (ca. 8-10 drops) to a MOF sample (ca. 1-2 mg).[145] The mixture is sonicated for a few minutes until the MOF is fully dispersed. Afterwards, deuterated dimethyl sulfoxide (DMSO-d_6) is added to the solution to dissolve the components of the digested mixture (metals, linkers, modulators, solvent, etc). Valuable information can be extracted that includes information on MOF purity, linker ratios, and the presence of modulator, guest molecules, and remaining solvent molecules. Demonstrated in

Figure 1.12, ^{1}H-NMR spectroscopy can be used to analyze a MOF sample containing benzoic acid capping ligands.

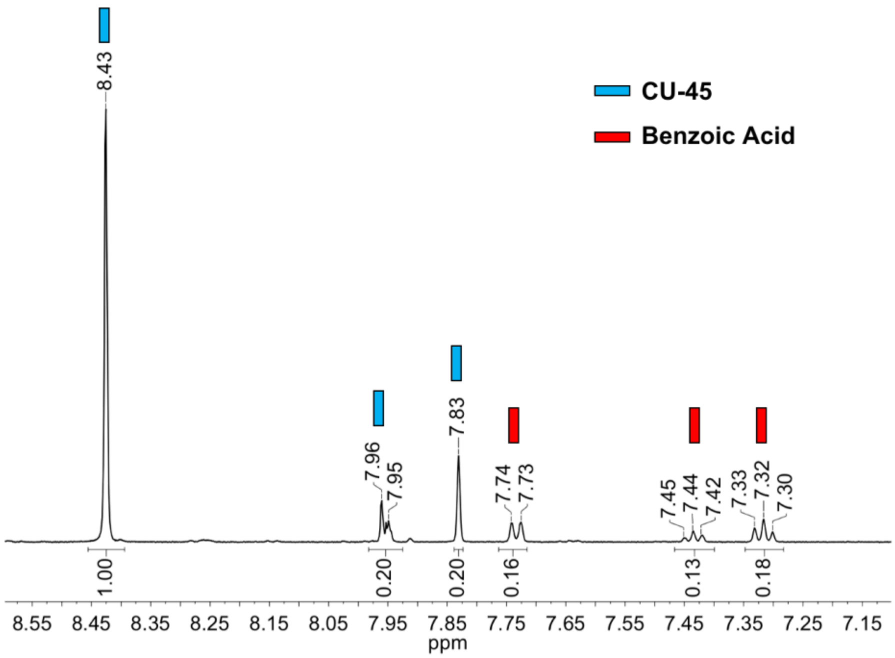

Figure 1.12. ^{1}H-NMR spectrum of CU-45 with benzoic acid capping ligands.

1.5.6.2. Solid-State NMR (SS-NMR) Spectroscopy

To circumvent the insolubility of MOF samples, solid-state NMR (SS-NMR) spectroscopy can be used. SS-NMR is a powerful technique, as it probes the local structure surrounding the nucleus of interest with short-range ordering, and is widely used in exploring the local structure of various materials which include MOFs.[146–149] SS-NMR can provide further valuable structural information on the framework, linker composition, and guest molecules in MOFs. SS-NMR possesses the ability to detect dynamic effects and structural parameters, such as identifying the presence and interactions of guest molecules (*e.g.* host-guest interactions).[147,148] In addition to characterizing organic linkers within a MOF using ^{1}H and ^{13}C SS-NMR, with the appropriate probe, SS-NMR can be used to investigate the inorganic SBUs (*i.e.* metal chains or clusters).[147]

1.5.7. Diffuse Reflectance Infrared Fourier Transform Spectroscopy (DRIFTS)

Diffuse reflectance infrared Fourier transform spectroscopy (DRIFTS) is a type of infrared spectroscopy technique that is generally used for powder samples. In MOFs, DRIFTS is a useful technique when investigating the presence or absence of IR-active functional group.[150] As radiation is focused on a sample, the radiation is reflected in all directions if the material has texture, such as a MOF.[151] One of the main advantages of using DRIFTS is the simple sample preparation with the ability to extract valuable information. DRIFTS is performed by loading a powdered sample (*e.g.* MOF) into a sample holder. Prior to the addition of the sample, the powder can be mixed with a non-absorbent matrix such as potassium bromide (KBr) using a mortar and pestle. It is important to remember that physical grinding can alter or degrade the framework of less stable MOFs.

Characteristic IR stretches observed from MOFs arise from functional groups (e.g. -OH stretching, C-H stretching, and C=O stretching) that are IR active, which come from the organic linker functional groups and other functional groups found in the metal node. For example, there can be hydroxyl stretches ranging from 3500 to 3800 cm^{-1} that arise from the presence of water in the sample. It is important to thoroughly activate MOF samples prior to running DRIFTS, as a large -OH band broadening peak can obstruct the peaks in this region. Utilizing the presence of IR active functional groups can provide valuable information on MOFs, in respect to their organic linkers, capping ligands, presence of guest molecules, and MOF purity following activation. Presented in Figure 1.13, DRIFTS was used to analyze a MOF before and after the addition of benzoic acid capping ligands.

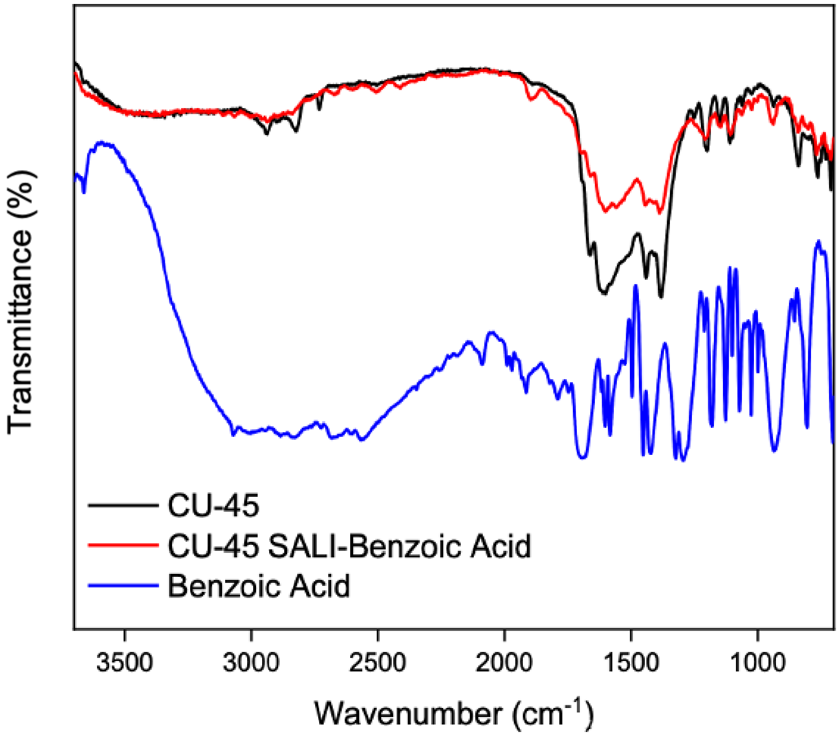

Figure 1.13. DRIFTS spectra of CU-45 before and after SALI with benzoic acid.

1.5.8. Circular Dichroism (CD) Spectroscopy

Circular dichroism (CD) spectroscopy is an absorption spectroscopy method using circularly polarized light.[152] Since circularly polarized light is chiral, meaning there are two non-superimposable forms that are mirror images of one another, a molecule must be chiral in order to absorb this light, as seen with a variety of biological molecules.[152] Recently, CD has been used to measure the chiral properties of MOFs.[153] In order to perform solid-state CD, samples are mixed with inert materials, typically CsI, KCl, or KBr and are pressed into a pellet under high vacuum. To construct a transparent pellet, and to remove humidity, the mixture (*e.g.* KBr plus sample) must be pressed under vacuum. As a result, transparent pellets avoid light scattering, and provide sufficient CD spectra.

1.6. Applications of RE-MOFs

On account of their aforementioned structural characteristics, properties, and their tunable nature, RE-MOFs have been studied for a broad range of applications. To date, RE-MOFs have been investigated for potential applications, which include, but are not limited to, sensing,[154,155] lighting applications,[156,157] gas adsorption,[158] chemical separations,[159] catalysis,[160,161] drug delivery,[162,163] bioimaging,[164] proton conductivity,[165] and single molecule magnets.[166] While many of these applications are not exclusive to RE-MOFs, and have been studied across all MOF families, several applications take advantage of the unique properties of RE-metals (more specifically lanthanides) to carry out the desired function. In this section, some examples of potential applications of RE-MOFs are presented, placing a focus on using RE-metals for their luminescence properties in chemical sensing applications.

1.6.1. Chemical Sensing

The luminescent properties of RE-coordination polymers[154,155,167] and RE-MOFs[168–172] have been studied since the materials first emerged in the literature. Given that the molar extinction coefficients for lanthanide ions are low, structural organic linkers and/or guest molecules encapsulated in the pores of MOFs can be used as antennas to absorb photons and sensitize emission from the metal. Furthermore, information about the number of coordinated terminal water ligands on lanthanide MOF nodes can be obtained by analyzing emission decay times,[168,173] a feature that can help discern the coordination number and formula of a MOF. This sensitivity of lanthanide ion emission decay times to the number of coordinated water (and to a lesser extent, hydroxyl) ligands can be harnessed to study these materials in sensing applications. While the majority of RE-MOF sensing studies are based on luminescence as a reporting mechanism, there are also examples of electrochemical sensors based on RE-MOFs. Over recent years, these MOFs have been applied to detect gases[103] and vapours,[174] small molecules,[175,176] cations,[177] anions,[178,179] biomarkers,[178] temperature variations,[181] and pH changes.[182]

In 2013, Song *et al.* reported a RE-MOF that demonstrates a selective luminescence response to DMF vapour.[174] The MOF, shown in Figure 1.14, is comprised of Eu(III)-chain nodes bridged by 2',5'-bis(methoxymethyl)-[1,1′:4′,1′′-terphenyl]-4,4′′-dicarboxylic acid linkers giving rise to accessible open channels for solvent exchange to occur. When DMF from the synthesis is exchanged with water, the resulting RE-MOF exhibits weak emission from Eu(III) due to quenching caused by O–H oscillations from coordinated water ligands. Once exposed to DMF vapour, however, a turn-on luminescence is observed which is attributed to DMF replacing the terminal water ligands in the MOF.

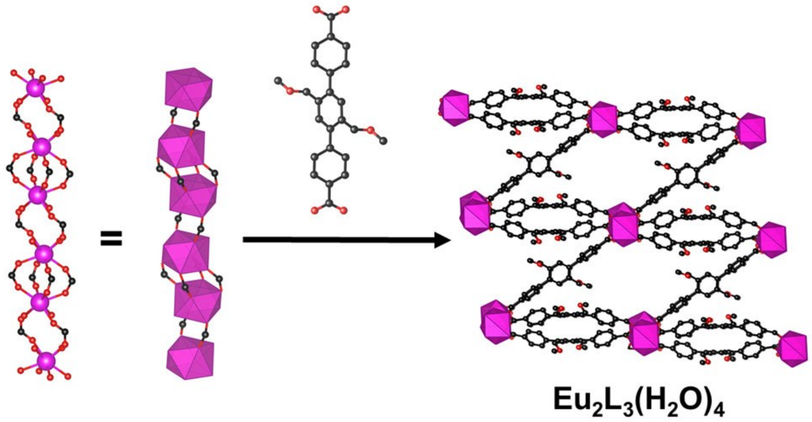

Figure 1.14. Structure of $Eu_2L_3(H_2O)_4$, highlighting the Eu(III)-chain node and 2′,5′-bis(methoxymethyl)-[1,1′:4′,1′′-terphenyl]-4,4′′-dicarboxylic acid linker. Eu = pink, C = black, O = red. Hydrogen atoms omitted for clarity.

Additionally, the RE-MOF was found to be selective for DMF vapour, as increases in luminescence intensity were negligible in the presence of twelve other solvent vapours. A similar sensing mechanism was observed in an earlier example using Eu(BTC), a Eu(III)-analogue of MOF-76 (Figure 1.5), comprised of Eu(III)-chain nodes and BTC linkers.[176] In this example, liquid

DMF was found to enhance luminescence from the Eu(III) ions while liquid acetone was found to quench the emission.

While replacement of terminal –OH and –OH_2 ligands in RE(III)-MOFs can give rise to turn-on luminescence, analytes that hydrogen bond with these ligands can also minimize luminescence quenching effects caused by O–H oscillations. This mechanism was observed by Chen, Qian *et al.* in Tb-MOF-76 (Figure 1.5) where hydrogen bonding between terminal methanol ligands and F^- analytes was found to enhance luminescence from the MOF.[179] Given that hydrogen bonding interactions with F^- are quite strong, the MOF was selective for sensing F^- vs. Cl^-, Br^-, NO_3^-, SO_4^{2-}, and CO_3^{2-}. Using a different approach to sensing F^- with a RE(III)-MOF, Stylianou *et al.* reported SION-105, a MOF comprised of dinuclear Eu(III)-cluster nodes bridged by tris(p-carboxylic acid)tridurylborane linkers, shown in (Figure 1.15), which acts as a selective, sensitive, and recyclable chemical sensor for detecting F^- in drinking water.[178]

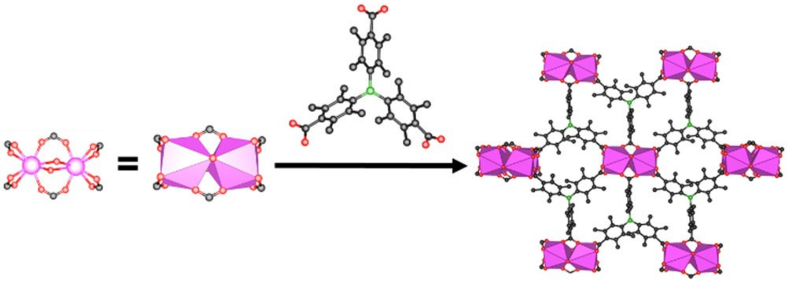

Figure 1.15. Structure of SION-105, highlighting the dinuclear Eu(III)-cluster node and tris(p-carboxylic acid)tridurylborane linker. Eu = pink, C = black, O = red, B = green. Hydrogen atoms omitted for clarity.

In this example, the F^- interacts with the organic linker of SION-105, which contains a Lewis-acidic boron receptor. Turn-off sensing was observed, possibly due to changes in the absorption spectrum of the boron-based antenna ligand after coordination to F^-.

Another example was reported in 2012, in which mixed-metal MOF demonstrated temperature-dependent luminescence suitable as a potential ratiometric temperature sensor.[34] Demonstrated by Qian, Chen *et al.*, an approach assembled mixed-lanthanide metal MOFs to yield Tb(III)/Eu(III)-DMBDC, assembled with Tb(III)/Eu(III)-chain nodes with 2,5-dimethoxy-1,4benzenedicarboxylic acid linkers (DMBDC) (Figure 1.16), and was found to demonstrate dual emission arising from both the Tb(III) and Eu(III) sensitized by the organic linkers. RE-DMBDC demonstrated temperature-dependent luminescence, as temperature increased, the Tb(III) emission decreased, while, Eu(III) emission increased. These results were consistent with energy transfer mechanisms that occur between Tb(III) and Eu(III) at increased temperatures. Therefore, by tuning the triplet energy of the linker (*i.e.* antenna) in the MOF, the energy transfer and temperature sensing, could be made more sensitive.

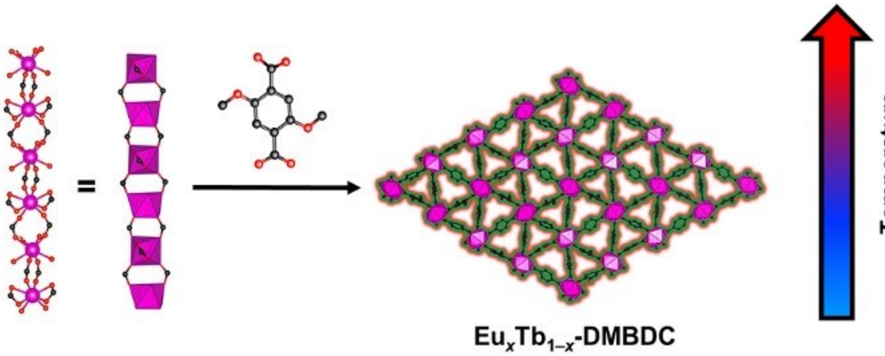

Figure 1.16. Structure of the dual-emitting RE-DMBDC, highlighting the Eu/Tb(III)- chain node and 2,5-dimethoxy-1,4-benzenedicarboxylic acid linker. Eu/Tb = pink, C = black, O = red. Hydrogen atoms omitted for clarity.

Of the various attractive features that MOF possess, their structural flexibility allows them to possess a much greater magnitude of response to external stimuli than other traditional materials.[183] MOFs have demonstrated that they undergo structural changes in response to various stimuli that include temperature, adsorption/desorption of guest molecules, pressure, light, and electric fields.

1.7. Scope of Thesis

The following two chapters will present the design, synthesis, and characterization of a library of novel RE-MOFs assembled with a variety of RE-metals and a tritopic organic linker. The primary objective of this work is to synthesize RE-MOFs with **spn** topology, using RE_6-cluster nodes as SBUs.

Chapter 2 describes the design, synthesis and experimental investigation of the complex structural and physical properties of CU-45, a MOF with **spn** topology comprised of Y_6-cluster nodes. It was determined that when exposed to various external stimuli, CU-45 undergoes a crystalline phase-transition to give an entirely different MOF with **msx** topology comprised of Y-chain nodes. This crystalline phase-transition is thoroughly investigated and discussed.

Chapter 3 explores the design and synthesis of lanthanide analogs of CU-45. Isostructural RE-MOFs, RE-CU-45, were constructed with Tb(III), Er(III), Eu(III), and Nd(III). RE-CU-45 is successfully characterized using PXRD, N_2 sorption isotherms, TGA/DSC, and photoluminescence spectroscopy. Furthermore, preliminary investigations describing the use of templating agents to stabilize the RE_6-cluster of CU-45 are discussed.

Chapter 2

Exploring the stimuli-responsive structural transformation of an achiral to chiral rare-earth metal–organic framework

2.1. Introduction

Metal–organic frameworks (MOFs) are a class of multifunctional, porous materials[5,6,184–186] with diverse structural tunability that can be used for various potential applications.[187–195] In addition to the many important potential applications of MOFs, these beautiful network structures also allow for the study of various fundamental phenomena in inorganic and materials chemistry. MOFs are constructed from inorganic metal nodes and organic linkers (di-, tri-, tetratopic etc.) that assemble into 2D or 3D framework materials.[196,197] MOFs with targeted structures and properties can be synthesized due to the seemingly endless combinations of metal nodes and organic linkers that can be used as building blocks.[184,198] Over the years, MOFs comprised of s-,[198,199] p-,[12,13] d,[14,200–202] and f-block[198,203,204] metals have been reported. Owing to their high and variable coordination numbers and geometries, the incorporation of f-block metals in MOFs has attracted significant interest, as unique structures can be realized. Among the f-block elements that have been explored, MOFs comprised of rare-earth (RE) metals have been shown to have diverse structures, with secondary buildings units (SBUs) that include metal ions, chains, or multinuclear clusters.

The high coordination number of RE-metals, particularly when coupled with the ability to form multinuclear cluster nodes, allows for the synthesis of intricate structures with complex topologies.[108,205–207] These unique structures arise, in part, from the ability to form highly connected (12-[105,112,208,209], 18-[108,210]) metal nodes. On the other hand, the design and synthesis of RE-cluster MOFs with lower node connectivity (8-, 6-) is less commonly explored due to difficulties associated with stabilizing under-connected multinuclear RE-clusters.[209] This is in contrast to the well-known Zr-based MOFs where frameworks with 4-,[211] 6-,[212,213] and 8-connected[214–217] nodes have been studied for various applications where metal accessibility is an asset. Herein we show the synthesis, isolation, and characterization of a RE-MOF, named CU-45 (CU = Concordia University) comprised of 6-connected hexanuclear RE-cluster nodes. Despite the challenges associated with synthesizing MOFs comprised of under-connected RE-clusters, CU-45 was isolated and fully characterized. Interestingly, CU-45, an achiral MOF, was found to undergo a stimuli-responsive structural transformation to give the chiral Y-MOF-76. To the best of our knowledge, this is the first example of a stimuli-responsive structural transformation of an achiral to chiral MOF, as well as the first example of a structural transformation that involves a cluster SBU transforming to a chain (or rod) SBU.

CU-45 is comprised of hexanuclear Y_6-cluster nodes bridged by 1,3,5-tricarboxylic acid (H_3BTC) linkers forming a 3,6-connected framework with **spn** topology (Figure 2.1, left), which is isostructural to the Zr_6- based MOF-808.[218] During the processes of synthetic optimization and characterization, we serendipitously discovered that CU-45 undergoes a unique transformation to give Y-MOF-76 when exposed to various external stimuli such as temperature, pressure through manual grinding, and soaking in various solvents. Y-MOF-76 is comprised of Y(III)-chain nodes, bridged by H_3BTC linkers, forming a chiral structure with **msx** topology (Figure 2.1, right).

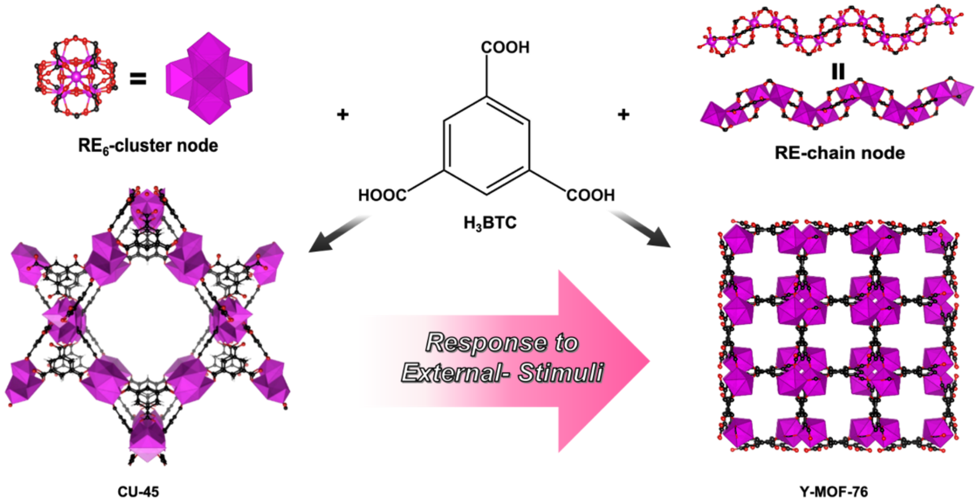

Figure 2.1. Schematic representation of the assembly of CU-45 (lower left) and Y-MOF-76 (lower right) comprised of a RE_6- cluster node and RE-chain node, respectively; and the transition between CU-45 and Y-MOF-76 in the presence of external-stimuli. Colour scheme: RE = pink, O = red, and C = black. Hydrogen atoms omitted for clarity.

MOFs have been shown to undergo phase transitions or conformational changes related to flexibility through exposure to external stimuli,[219–221] in response to temperature,[211,214] guest molecules,[204,211,222] acidic modulators,[220] and pressure.[219,223] MOF structural transformations that involve structural bonds breaking and/or forming in the solid state are more rare. Recently, Sun *et al.* reported a solid-state transformation of an interpenetrated to non-interpenetrated MOF, following the rearrangement of chain SBUs through a thermally driven single-crystal-to-single-crystal (SCSC) transformation.[224] To the best of our knowledge, there have been no reports on stimuli-responsive solid state achiral to chiral MOF transformations.

To gain more understanding about this unique structural transformation, we report time-resolved *in situ* variable-temperature powder X-ray diffraction (VT-PXRD), carbon solid-state NMR spectroscopy (^{13}C SS-NMR), and circular dichroism (CD) spectroscopy monitoring the structural transformation and appearance of chirality that occur due to the unfolding of RE(III)-metal cluster nodes to RE(III)-chain nodes. Additionally, through the use of density functional theory (DFT) calculations, the formation energies of both CU-45 and Y-MOF-76 were determined, and a mechanism for the transformation is proposed.

2.2. Experimental Procedure

2.2.1. General Materials and Methods

All materials, chemicals and solvents were purchased from commercial suppliers. Yttrium (III) nitrate hydrate (99.9%), 1,3,5-benzenetricarboxylic acid (H_3BTC), and trifluoracetic acid (TFA) were purchased from Alfa Aesar. *N,N*-dimethylformamide (DMF), chloroform, hexanes (98%), R-and S-limonene, and potassium bromide (KBr) were purchased from Sigma-Aldrich. Acetone, ethanol (95%), methanol, toluene, tetrahydrofuran (BHT stabilized) (THF), and dichloromethane (DCM) were purchased from Fisher Scientific. Liquid Nitrogen (N_2) was purchased from Megs Speciality Gases.

Powder X-ray diffraction (PXRD) data was collected on a Bruker D8 Advance diffractometer equipped with a LYNXEYE linear position sensitive detector (Bruker AXS, Madison, WI). CU-45 was placed onto the low-background sample holder. Data was collected using a continuous coupled $\theta/2\theta$ scan with Ni-filtered Cu$K\alpha$ ($\lambda = 1.54178$ Å) radiation operating at 40 kV and 40 mA. Variable temperature powder X-ray diffraction (VT-PXRD) measurements were collected on a Bruker D8 Advance instrument equipped with a LYNXEYE detector using Ni-filtered Cu*K*α (λ = 1.54178 Å) radiation. The setup was equipped with Anton Paar CHC$^+$ chamber. Diffractograms were collected in a stepwise fashion, and after each collection (ca. 7 min), the temperature in the chamber was raised in intervals of 5 °C at a rate of 1 °C min^{-1} and a new collection started.

scXRD data were measured on a Bruker D8 Venture diffractometer equipped with a Photon 200 detector, and an IμS microfocus X-ray source (Bruker AXS, Cu*K*α source). All measurements were carried out at 298(2) K on crystals coated with a thin layer of amorphous oil. Structure solution was carried out using the SHELXTL package from Bruker.[225] The parameters were refined for all data by full-matrix-least-squares on F2 using SHELXL.[226,3] All the non-hydrogen atoms were refined with anisotropic thermal parameters. All other hydrogen atoms were placed in calculated positions and allowed to ride on the carrier atoms. Y-MOF-76 exhibits unresolved, disordered coordinated DMF and all the attempts to model the DMF met with no success. The structure was squeezed using PLATON Squeeze command,[4] leaving oxygen atoms corresponding to coordinated DMF.

Rietveld refinement[227] of the crystal structure of CU-45 was performed using the program TOPAS Academic 6,[228] using the isostructural Zr-MOF-808 as a starting model. The diffraction peak profile was modelled using a pseudo-Voigt function combined with a simple axial divergence model. The background was modelled with a 6th degree Chebyshev polynomial function. Coordinates of yttrium and oxygen atoms within the metal cluster were refined independently, subject to the crystallographic symmetry constraints, the BTC and formate ligands were refined as rigid bodies. The material used for PXRD data collection contained an impurity of Y-MOF-76 framework, which was modelled as a separate crystalline phase during the refinement. Crystallographic parameters of CU-45 are summarized in Table A.2, and the Rietveld refinement is shown in Figure A2.1.

Thermogravimetric analysis coupled with differential scanning calorimetry (TGA/DSC) data was collected on the Mettler Toledo TGA 5500 Discovery. Thermal stability of CU-45 samples was tested from 25 to 800 °C under air (60.00 L/min) with consistent heating of 10 °C per minute.

N_2 adsorption and desorption isotherms for CU-45 were performed on Micromeritics TriStar II Plus automated surface area and porosity analyzer. The sample tubes were cooled with liquid N_2 before data was collected. Drying with supercritical CO_2 ($scCO_2$) was performed using a Tousimis Samdri-PVT-3D manual critical-point dryer.

Scanning electron microscopy (SEM) for CU-45 was performed on a JEOL JSM7600F equipped with a field effect gun.

Proton and fluorine (^{1}H and ^{19}F NMR) nuclear magnetic resonance spectroscopy measurements were collected on a Varian VNMRS-500 MHz system equipped with a 5 mm AutoX DB (Dual Broadband) probe with automatic tuning by ProTune accessory. Samples (~0.2 mg) were digested in sulfuric acid-d_2 solution (~8 drops) and sonicated for 10 minutes. After sonication, dimethyl sulfoxide-d_6 was added to the mixture to dissolve the digested MOF sample.

Diffuse Reflectance Infrared Fourier Transform Spectroscopy (DRIFTS) spectra were collected on a Thermo Scientific Nicolet 6700 FTIR spectrometer equipped with an MCT detector. The detector was cooled with liquid N_2 and the samples were collected in air. Potassium bromide (KBr) was used to prepare samples and act as a sample background.

^{13}C SS-NMR spectra were acquired using cross-polarization in a VNMRS 400 widebore NMR spectrometer operating at 399.9 MHz for ^{1}H and 100.5 MHz for ^{13}C in a 4 mm Varian Chemagnetics double-resonance probe. The spectrum of CU-45 was acquired in 512 scans with a CP contact time of 2 ms, under spinning at 13 kHz. The recycle delay was 5 s. The same parameters were used for Y-MOF-76 and H_3BTC, except that 1800 and 888 scans were acquired, respectively. The spectrum of CU-45 ground was also acquired with a CP contact time of 2 ms and a recycle delay of 5 s, but spinning was at 5 kHz, so TOSS was used to suppress spinning sidebands. 10000 scans were acquired.

Periodic DFT calculations were performed using the plane wave DFT code CASTEP 19.1.[229] and crystal structures of CU-45, Y-MOF-76, yttrium formate $Y(HCOO)_3$, and BTC. Furthermore, gas phase energies of water and formic acid molecules were simulated in CASTEP by placing the molecules in a cubic box of 20 Å dimension, which was found to be sufficiently large to make the interaction between the periodic images of the molecules negligible. The calculations were performed using a PBE[230] functional combined with Grimme D2[231] dispersion correction. The plane wave basis set was truncated at 700 eV cutoff, and the CASTEP built-in ultrasoft pseudopotentials were used to attenuate the Coulomb potential in the core regions of electron density. The 1st electronic Brillouin zone was sampled with $2\pi\times0.07$ Å^{-1} Monkhorst-Pack[232] k-point grid.

Circular dichroism (CD) spectroscopy spectra were collected on a Jasco CD spectropolarimeter equipped with J-715 lamp measured from 230 to 700 nm. Samples were collected with dried KBr and were prepared as KBr pellets using high vacuum hydraulic press. Prior to pellet formation, 10 uL of chiral additive, R- and S-limonene, was added to MOF sample and ground and dried until limonene evaporated.

2.2.2. Synthesis and Activation of CU-45, Y-MOF-76, and MOF-808

Synthesis of CU-45. Synthesis of CU-45 (Figure 2.2a) was performed by traditional solvothermal methods. $Y(NO_3)_3 \cdot 6H_2O$ (237 mg, 0.62 mmol) was added to a 6-dram vial with 0.6 mL trifluoroacetic acid (TFA) and 12 mL of *N-N*-dimethylformamide (DMF) and placed in the sonicator for ca. 20 minutes. Subsequently, H_3BTC (27 mg, 0.13 mmol) was added to the homogenous solution. The mixture was sonicated once more and placed in an oven at 130 °C and left undisturbed for 120 hours. After cooling to room temperature, white crystal flakes of CU-45 were immersed in fresh DMF, which was replaced three times (3 × 10 mL) throughout the day and soaked overnight. Afterwards, the DMF was removed via centrifugation, and the MOF sample was further soaked in fresh acetone, which was replaced three times (3 × 10 mL) throughout the day and soaked overnight. The product was isolated via centrifugation and left to dry for 24 hours at room temperature.

To obtain permanent porosity, several activation procedures were attempted for CU-45. CU-45 was activated at 80, 100, 110, 120, and 130 °C for 24 hours under dynamic vacuum oven, however, resulting in inadequate BET surface areas. To circumvent these issues, supercritical CO_2 ($scCO_2$) activation was attempted, although demonstrating similarly poor results. Finally, with the use of the SmartVac Prep (SVP) instrument and several variations in temperature (80, 100, 110, 120, and 130 °C) and time (20 and 24 hours), activation of CU-45 was achieved at 100 °C for 20 hours.

Synthesis of MOF-808. Synthesis of MOF-808 (Figure 2.2b) was achieved by traditional solvothermal methods, which includes the addition of $ZrOCl_2 \cdot 8H_2O$ (32.5 mg, 0.100 mmol), H_3BTC (21 mg, 0.100 mmol), and DMF/formic acid (5 mL/ 5 mL) in a 6-dram vial. The solution was placed in the sonicator for ca. 20 minutes, then placed in an oven at 130 °C for two days (48 hours). Microcrystalline powders were obtained after washing the material thoroughly with DMF

(3 × 15 mL) and soaking overnight, followed by the same washing procedure with acetone. As synthesized MOF-808 was activated under vacuum at 120 °C for 24 hours.

Synthesis of Y-MOF-76. Synthesis of Y-MOF-76 (Figure 2.2c) was performed by traditional solvothermal methods, which involves the addition of $Y(NO_3)_3 \cdot 6H_2O$ (229 mg, 0.600 mmol) to a 6-dram vial with 8 mL each of water and DMF. The mixture was sonicated for ca. 20 minutes. Subsequently, H_3BTC (42 mg, 0.200 mmol) was added to the homogenous solution. The mixture was sonicated once more and placed in an oven at 80 °C for three days (72 hours). After cooling to room temperature, white cotton-like crystals of Y-MOF-76 were washed with DMF (3 × 15 mL) and acetone (3 × 15 mL) and soaked overnight in acetone. The product was isolated via centrifugation and dried in air. Y-MOF-76 was activated at 100 °C for 24 hours under vacuum.

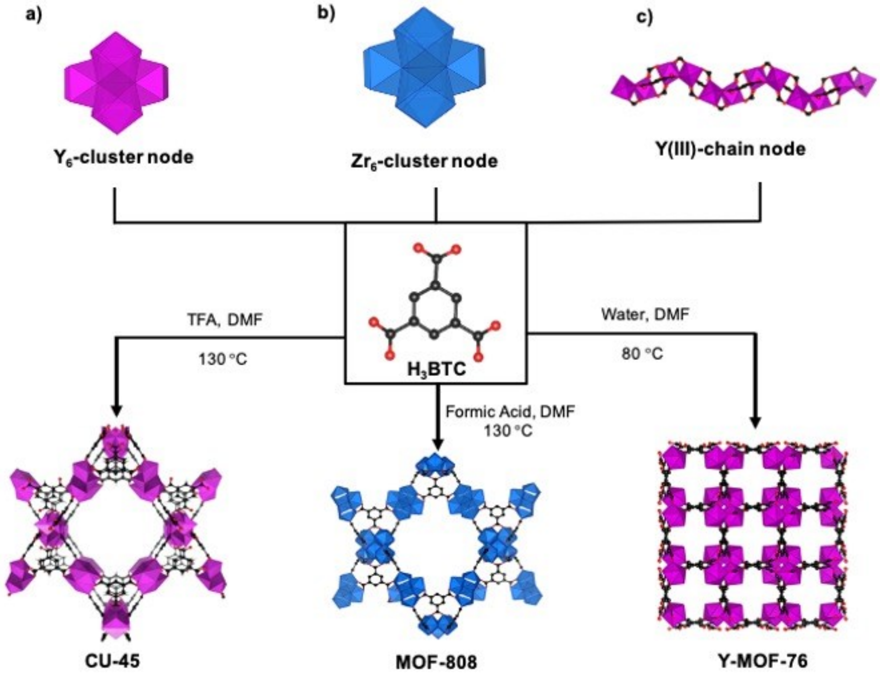

Figure 2.2. Synthesis of a) CU-45, b) Y-MOF-76, and c) MOF-808 through traditional solvothermal conditions. Colour scheme: RE = pink, O = red, C = black, and Zr = blue. Hydrogen atoms omitted for clarity.

2.3. Results and Discussion

CU-45 was synthesized using standard solvothermal conditions by reacting $Y(NO_3)_3 \cdot 6H_2O$ and H_3BTC in DMF with 0.6 mL of trifluoroacetic acid (TFA) as a modulator, at 130 °C for approximately five days. As expected, the powder X-ray diffraction (PXRD) pattern (Figure 2.3) and Rietfeld refined structure (Figure 2.1) of CU-45 resembles that of the well-known Zr_6-based MOF-808 reported by Yaghi *et al.*[218] One notable structural difference that cannot be discerned from X-ray crystallography arises from the oxidation state of the metal in the node. Owing to this difference in oxidation states, the hexanuclear cluster nodes comprised of Zr(IV) are known to have four μ_3-O and four μ_3-OH bridges, while the nodes comprised of Y(III) are expected to have eight μ_3-OH bridges for charge balancing purposes. The crystal structure of CU-45 shows the expected Y_6-cluster nodes bridged by H_3BTC linkers, forming a 3,6-connected MOF with **spn** topology (Figure 2.1).

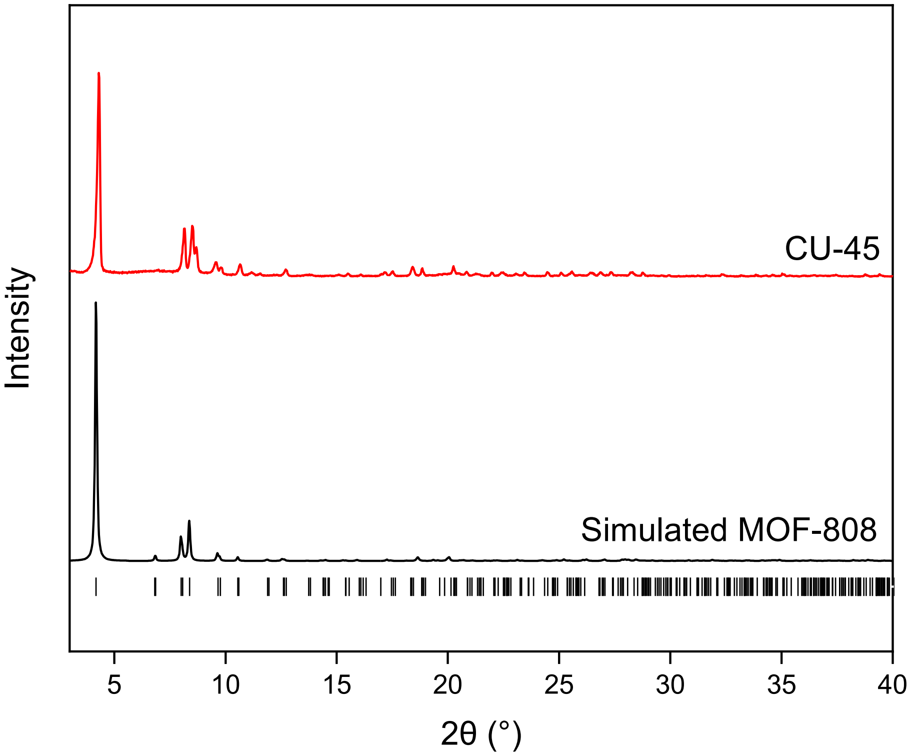

Figure 2.3. PXRD patterns of CU-45 synthesized *de novo* and compared to the simulated patterns of MOF-808.

When activated at 100 °C under vacuum for 20 hours, N_2 adsorption analysis of CU-45 reveals a type I isotherm (Figure 2.4a), giving rise to a BET area of 485 m^2/g. The pore size distribution (PSD) calculated using non-linear density functional theory (NLDFT), confirms the presence of an inner-pore cavity of 17.3 Å (Figure 2.4b) consistent with the ~17 Å pore observed in MOF-808.[233] Although the nitrogen isotherm shape and PSD are consistent with the **spn** topology of CU-45, the BET area is lower than the expected value of ~1500 m^2/g.

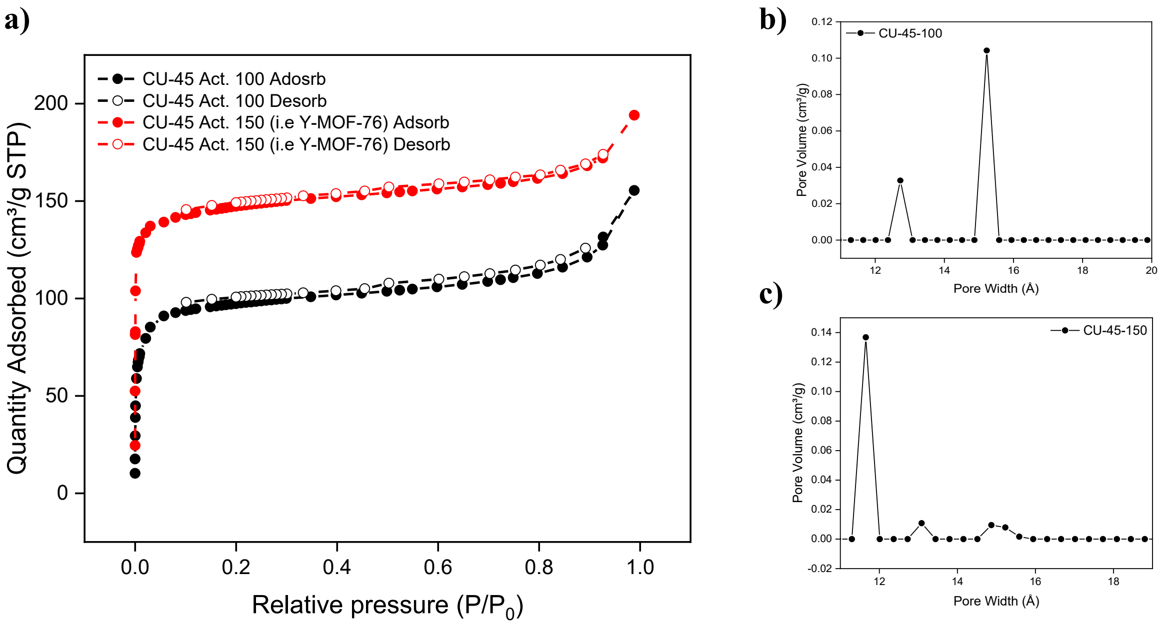

Figure 2.4. a) N_2 adsorption-desorption isotherms for CU-45-100 and CU-45-150. b) The reported pore-size distribution (PSD) analysis of CU-45 following activation at 100 °C. c) The reported pore-size distribution (PSD) analysis of CU-45 following activation.

This observation led us to try several activation procedures including solvent exchanges with various low-boiling solvents, vacuum activation under different temperatures, and supercritical CO_2 activation. Interestingly, when activated under vacuum at 150 °C, the slight mesoporous step (p/p_0 ~0.02) corresponding to the 15.8 Å (Figure 2.4a and b) pore in the N_2 adsorption isotherm disappears, and the PSD analysis reveals a pore at 11.8 Å only (Figure 2.4c).

In addition, the BET area of CU-45 activated at 150 °C increases to 585 m^2/g. These curious observations led us to evaluate the structure of CU-45 post-activation at 100 °C vs. 150 °C. PXRD patterns of the MOF post-activation (100 and 150 °C) reveal that the MOF undergoes a structural transformation, where the pattern for CU-45-100 shows two distinct phases, CU-45 and Y-MOF-76, while CU-45-150 shows that the MOF has been completely converted to the well-known, chiral, rare-earth MOF-76 (Figure 2.5).

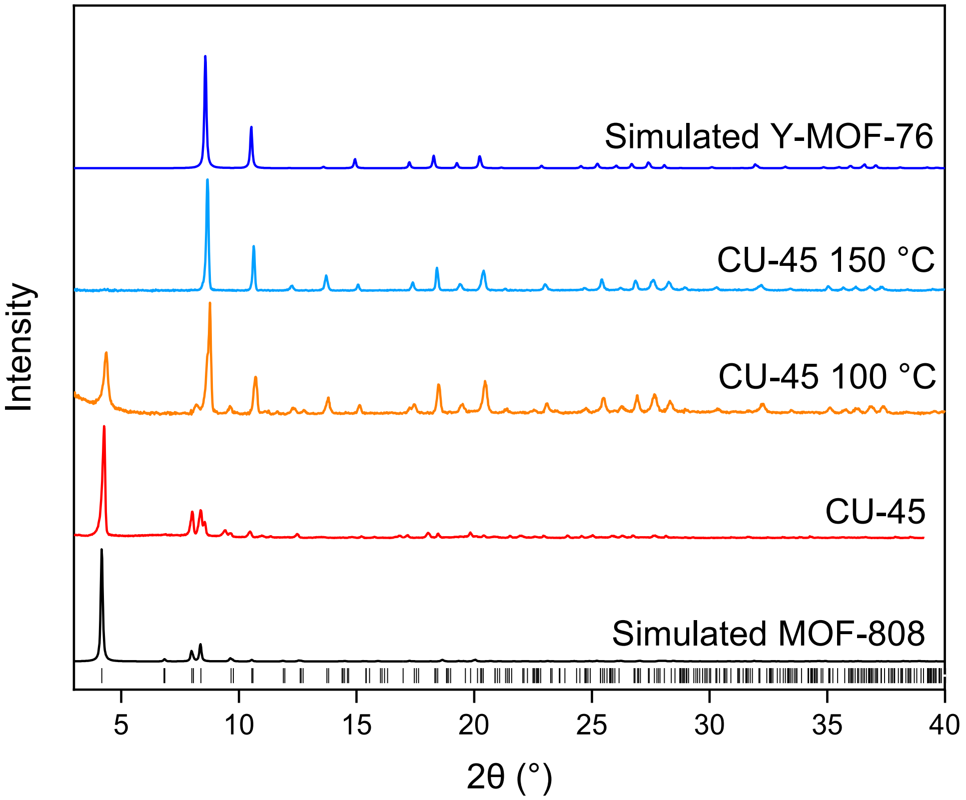

Figure 2.5. PXRD patterns of CU-45 as synthesized, CU-45-100, and CU-45-150 with simulated patterns for both MOF-808 and Y-MOF-76.

To understand more about the thermodynamics of the structural transformation, we performed *in situ* variable temperature PXRD (VT-PXRD) on CU-45. VT-PXRD was conducted on a fresh sample of CU-45 from 25 to 300 °C, in intervals of 5 °C between scans (over 6.5 hours of measurement). The results exhibit a transformation of CU-45 to an intermediate phase as is clearly observed between 90 and 130 °C (Figure 2.6a). The intermediate phase can be attributed to the loss of solvent guest molecules.[234] Further heating of the material led to the formation of fully activated Y-MOF-76 (Figure 2.6b).

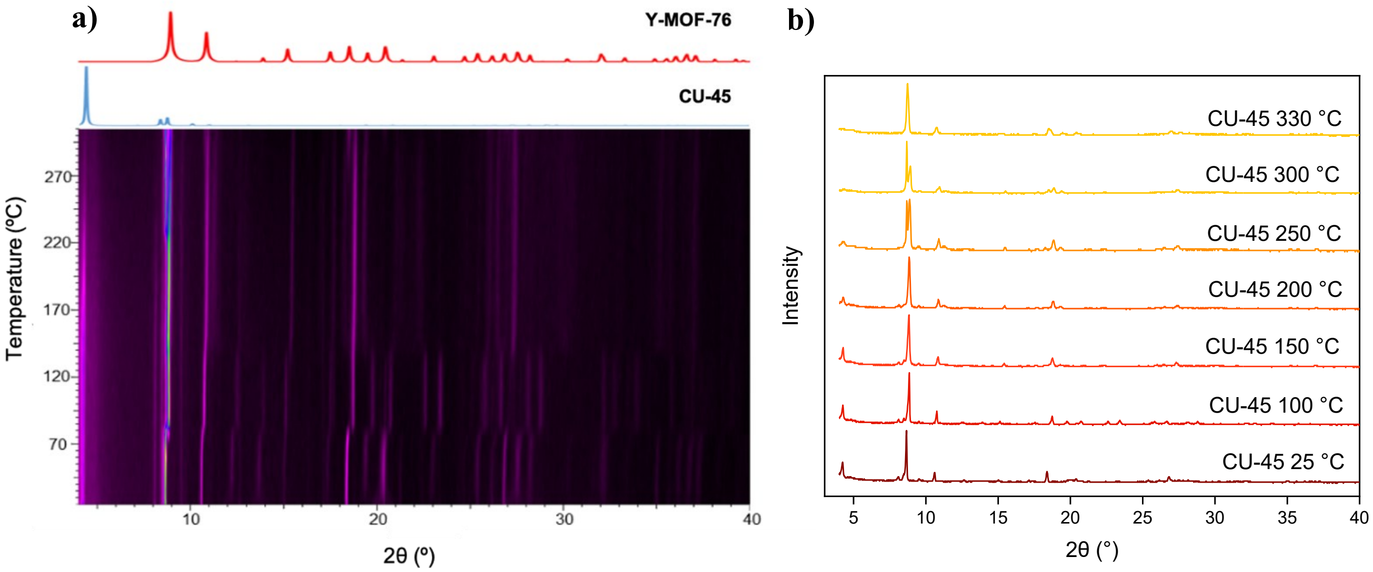

Figure 2.6. PXRD patterns of a) VT-PXRD analysis of CU-45 and Y-MOF-76 demonstrating the structural transformation occurring at elevated temperatures. b) CU-45 at elevated temperatures demonstrating the conversion to fully activated Y-MOF-76.

In order to understand whether MOF-808 would behave the same, we conducted identical VT-PXRD analysis between 25 and 300 °C (Figure 2.7). As expected, MOF-808 shows stability up to 270 °C, after which crystallinity slowly declines until complete amorphization occurs at 300 °C. This confirms that the unique achiral-to-chiral transformation of CU-45 to Y-MOF-76 is a consequence of the 6-connected Y_6-cluster metal nodes, which are more susceptible to hydrolysis than the analogous 6-connected Zr_6-nodes. The preference of RE-metals to form chain-nodes as the thermodynamic product could lead to several discoveries of stimuli-responsive structural transformations in RE-cluster based MOFs, particularly where the clusters are under-connected.

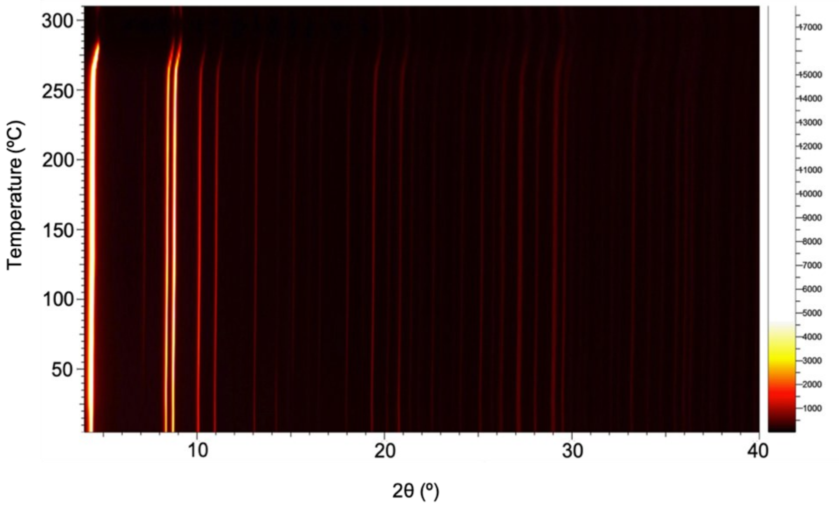

Figure 2.7. VT-PXRD analysis of MOF-808 synthesized *de novo* demonstrating stability of up to 270 °C, following the slowly amorphization that occurs at 300 °C.

In addition to the structural transformation of CU-45 to Y-MOF-76 observed upon activation (heating and vacuum), and upon heating alone, other external stimuli were found to give the same outcome. Mechanical grinding with a mortar and pestle, a technique commonly used to make fine powders of samples for PXRD measurements, was also found to transform the MOF. PXRD patterns acquired at various time intervals after manual grinding (Figure 2.8) show that the formation of Y-MOF-76 gradually begins even after 2 minutes of manual grinding. This demonstrates the importance of minimizing external pressure post-synthesis when attempting to isolate new MOFs where the mechanical stability of the material is not yet known.

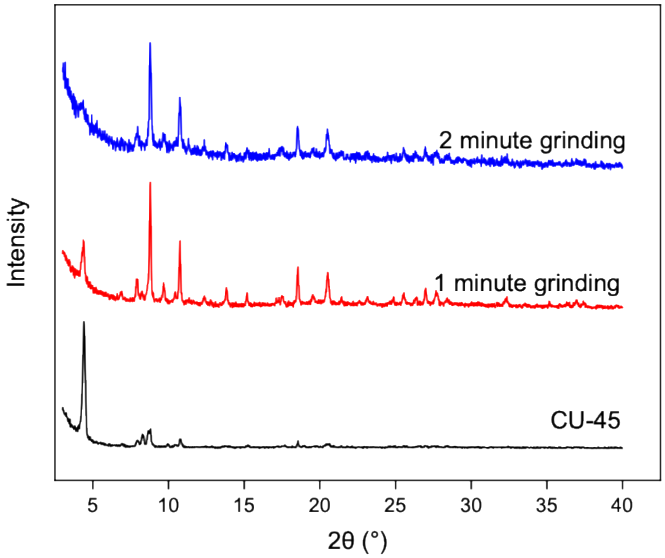

Figure 2.8. PXRD patterns of CU-45 and CU-45 ground at 1 and 2 minutes respectively.

External stimuli including pH and solvents were also tested. Fresh as-synthesized CU-45 was prepared as previously described, however, following activation of the material, CU-45 was soaked in 10 mL of water, methanol, ethanol, toluene, THF, chloroform, DMF, and DCM overnight. The material was then washed three times with acetone (3 × 10 mL) and air-dried. PXRD patterns of CU-45 were then obtained (Figure 2.9a and 2.9b).

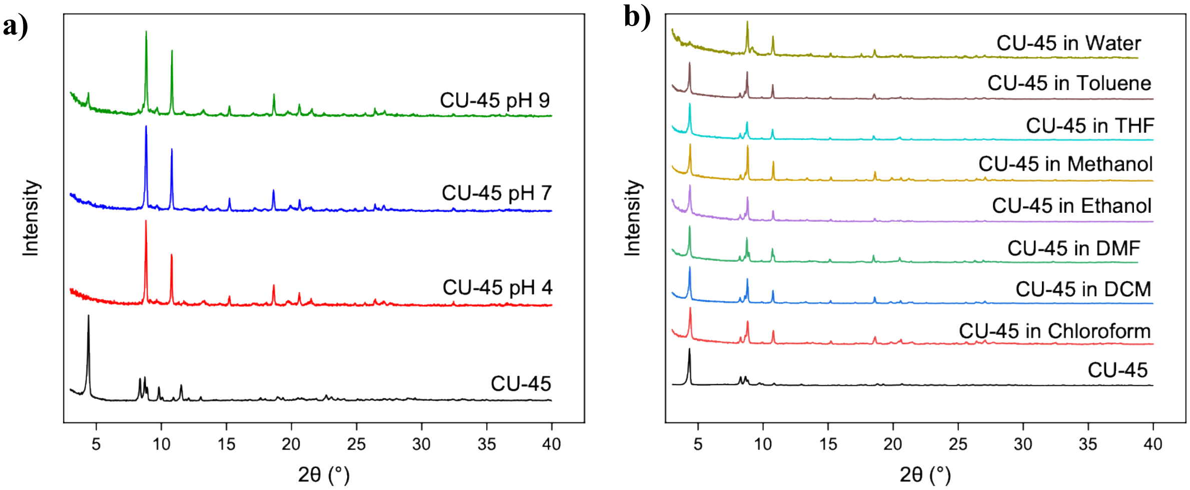

Figure 2.9. PXRD patterns of a) CU-45 after soaking in various organic solvents of varying polarity, and b) CU-45 soaking in pH 4, 7, and 9 respectively.

Partial transformation occurs in organic solvents such as methanol, ethanol, toluene, THF, chloroform and DMF, while nearly complete conversion occurs in water, and under acidic and basic conditions. This partial stability in organic solvents is somewhat surprising given the overall sensitivity of CU-45 to other external stimuli like mild pressure, and moderate temperatures but confirms that hydrolysis plays a key role in the transformation.

Scanning electron microscopy (SEM) images were obtained to provide further evidence for the transformation of CU-45 to Y-MOF-76, specifically in water. Figure 2.10 shows SEM images obtained for CU-45 and Y-MOF-76 synthesized *de novo*, as well as CU-45 after soaking in water for 24 hours. The images show the expected, distinct morphological differences between CU-45 and Y-MOF-76, where CU-45 demonstrates octahedron-shaped particles as observed for MOF-808,[218,235] while MOF-76,[198,236,237] demonstrates rod-shaped particles. SEM images of CU-45 after soaking in water overnight show rod-like particles consistent with transformation to Y-MOF-76.

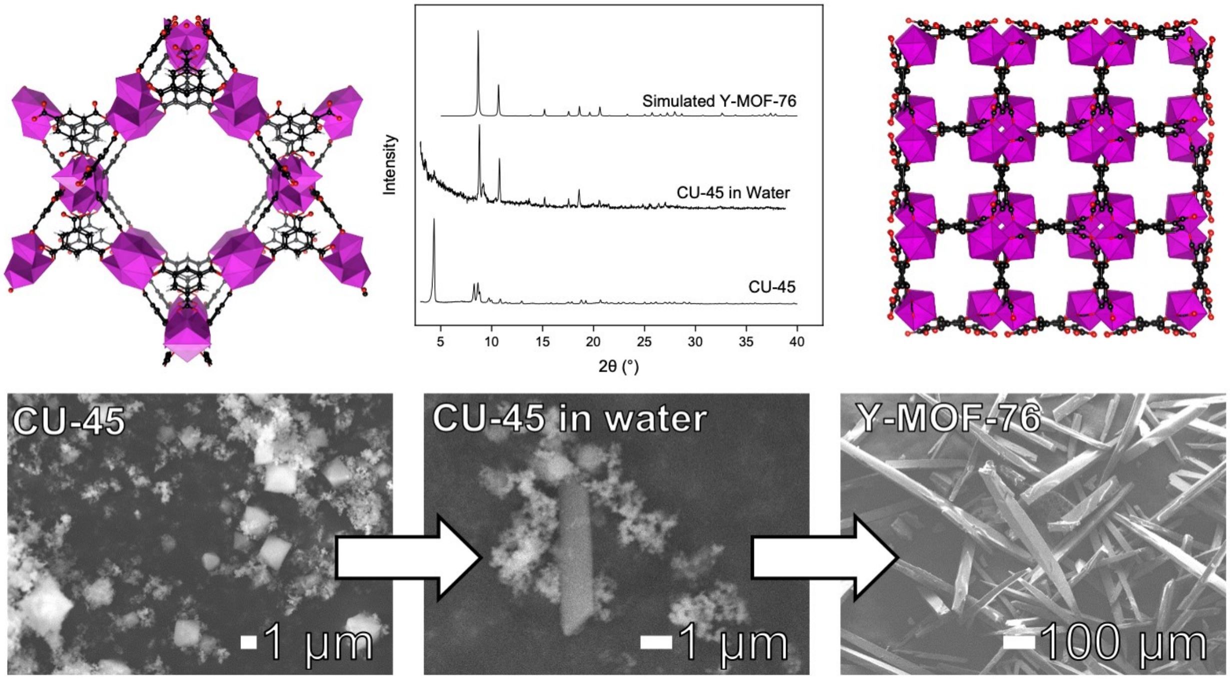

Figure 2.10. PXRD patterns of CU-45 synthesized *de novo*, CU-45 in water, and Y-MOF-76 with respective SEM images.

The thermal stability of CU-45 was measured following activation at 100 and 150 °C for 20 hours by thermogravimetric analysis (TGA). TGA measurements of CU-45-100 and CU-45-150 (*i.e.* CU-45 activated at 100 and 150 °C) were conducted under air from 25 to 800 °C where two distinct TGA curves were observed (Figure 2.11a), providing further evidence of RE-MOFs with structural differences.

For both CU-45-100 and CU-45-150 (*i.e.* Y-MOF-76), an individual weight loss is observed near 100 °C, which can be assigned to loss of solvent and capping ligands. The presence of formate and trifluoroacetate capping ligands in CU-45 is further confirmed by ^{1}H- (Figure 2.11b) and ^{19}F-NMR spectroscopy (Figure A2.14). In contrast, no capping ligands are observed for CU-45-150 (*i.e.* Y-MOF-76), consistent with the Y-chain node (Figure 2.11c).

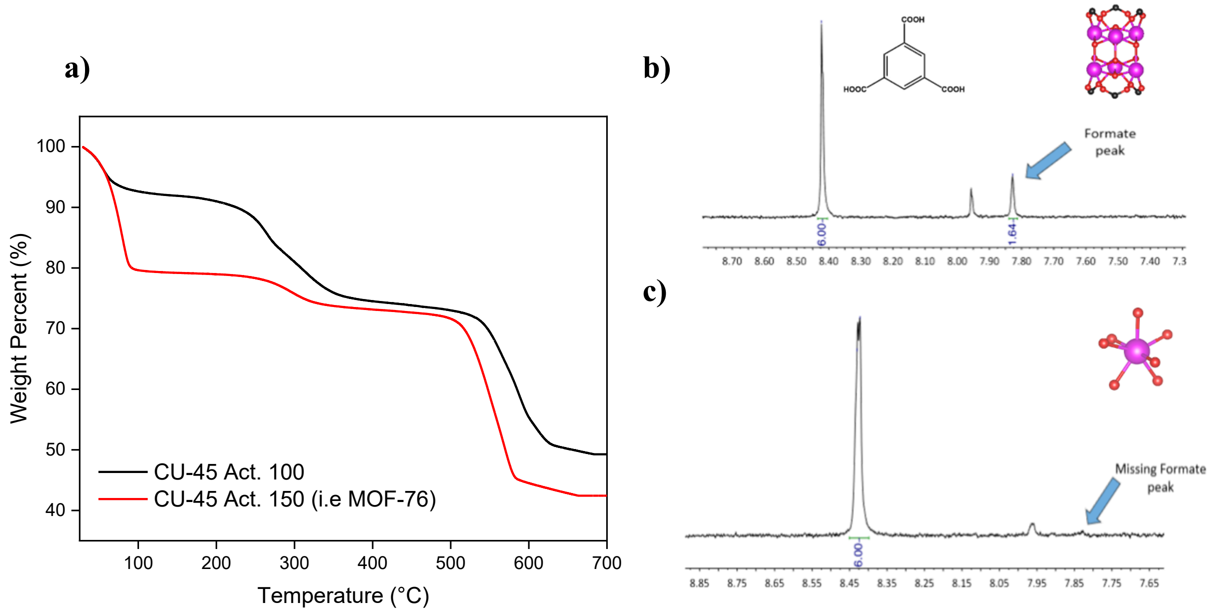

Figure 2.11. a) TGA curves of CU-45-100 (black) and CU-45-150 (red). b) ^{1}H NMR of CU-45 synthesized *de novo* demonstrating the formate peak. c) ^{1}H NMR of CU-45-150 synthesized *de novo* demonstrating the missing formate peak.

To confirm that the transformation of CU-45 to Y-MOF-76 is exothermic, thermogravimetric analysis coupled with differential scanning calorimetry (TGA/DSC), was performed (Figure 2.12). The initial weight loss (ca. 100-200 °C) measured on the TGA correlates with a phase-transition observed by DSC (Figure 2.12). Additionally, MOF-808 synthesized *de novo* was measured to investigate the similarities and differences between CU-45 and MOF-808 (Figure A2.6 and A2.7). An enthalpy (ΔH) of -201.21 kJ/mol can be extracted from the DSC corresponding to this transformation from CU-45 to MOF-76 occurring between 100-300 °C

(Figure 2.12). Subsequently, exothermic peaks are present in the DSC (ca. 500-600 °C) that arise from decomposition of the MOF into yttrium oxide (Figure A2.8).

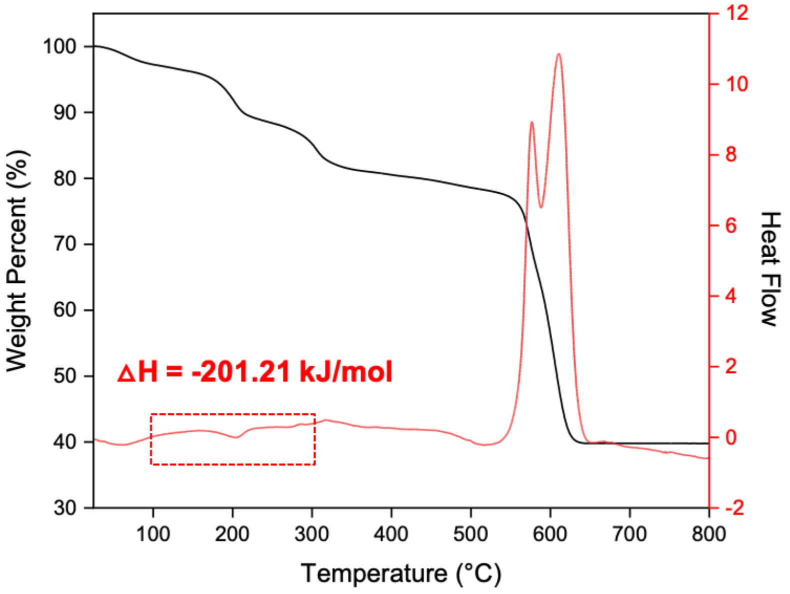

Figure 2.12. TGA/DSC (red/black) curves of CU-45. All TGA/DSC experiments conducted from 25 to 800 °C under air.

Theoretical formation energies were calculated using DFT to determine the enthalpy of the proposed transformation given by equation 1 (Table 1). The transformation must occur alongside the production of by-products since the empirical chemical formula of CU-45, $[Y_6(\mu_3\text{-}OH)_8(HCOO)(TFA)_3(BTC)_2]\cdot(DMF)_2(H_2O)_3)$, is not the same as Y-MOF-76, $[Y(BTC)(H_2O)_{1.5}\cdot(DMF)]$. We hypothesized that the byproducts are most likely to include yttrium formate ($Y(HCOO)_3$), yttrium hydroxide ($Y(OH)_3$), and yttrium trifluoroacetate ($Y(TFA)_3$), which was corroborated through the use of ^{13}C SS-NMR. Formation energies confirm that the reaction shown in equation 1 is exothermic with ΔH of -233.68 kJ/mol, a value similar to that extracted from DSC.

Equation 1

$$\mathrm{Y_6(\mu_3 - OH)_8(HCOO)(TFA)_3(BTC)_2 \cdot (DMF)_2(H_2O)_3 \rightarrow 2Y(BTC)(H_2O)_{1.5}{\cdot}(DMF) +}$$
$$\mathrm{\tfrac{1}{3}[Y(HCOO)_3 + \tfrac{8}{3}\,[Y(OH)_3] + \,[Y(TFA)_3]}$$

Table 1. The energy values for each species reported in equation 1 with calculated enthalpy values.

	Energy per unit cell / eV	**Energy per f. u. / eV**
Y-MOF-76	-22620.06	-5655.01
CU-45	-90141.63	-22535.41
Y_2O_3	-27808.64	-3476.08
$Y(OH)_3$	-4893.25	-2446.62
$Y(HCOO)_3$	-4237.49	-4237.49
BTC^-	-199340.15	-4152.92
H_2O	-	-471.56
Formic Acid	-	-1068.18
Enthalpy (ΔH / kJ mol^{-1})	-223.68	

Carbon solid-state NMR spectroscopy (^{13}C SS-NMR) was used to gain further information about the side-products produced during the transformation of CU-45 to Y-MOF-76. The ^{13}C SS-NMR spectra further confirm the transformation of CU-45 (Figure A2.19) to Y-MOF-76 due to the concomitant disappearance and appearance of signals at distinct chemical shifts attributed to each MOF (Figure 2.13). As observed from equation 1, the formation of Y-MOF-76 from CU-45 yields various by-products that include yttrium formate ($Y(HCOO)_3$), yttrium hydroxide ($Y(OH)_3$) and yttrium trifluoroacetate ($Y(TFA)_3$). From the ^{13}C solid state cross-polarization magic angle spinning (CPMAS) NMR spectra of a converted sample of CU-45 (now Y-MOF-76) (Figure A2.16 -A2.18), signals are observed for DMF (165, 38, and 31 ppm), $Y(HCOO)_3$ (177 ppm), and $Y(TFA)_3$ (ca. 161, 115, and 105 ppm).

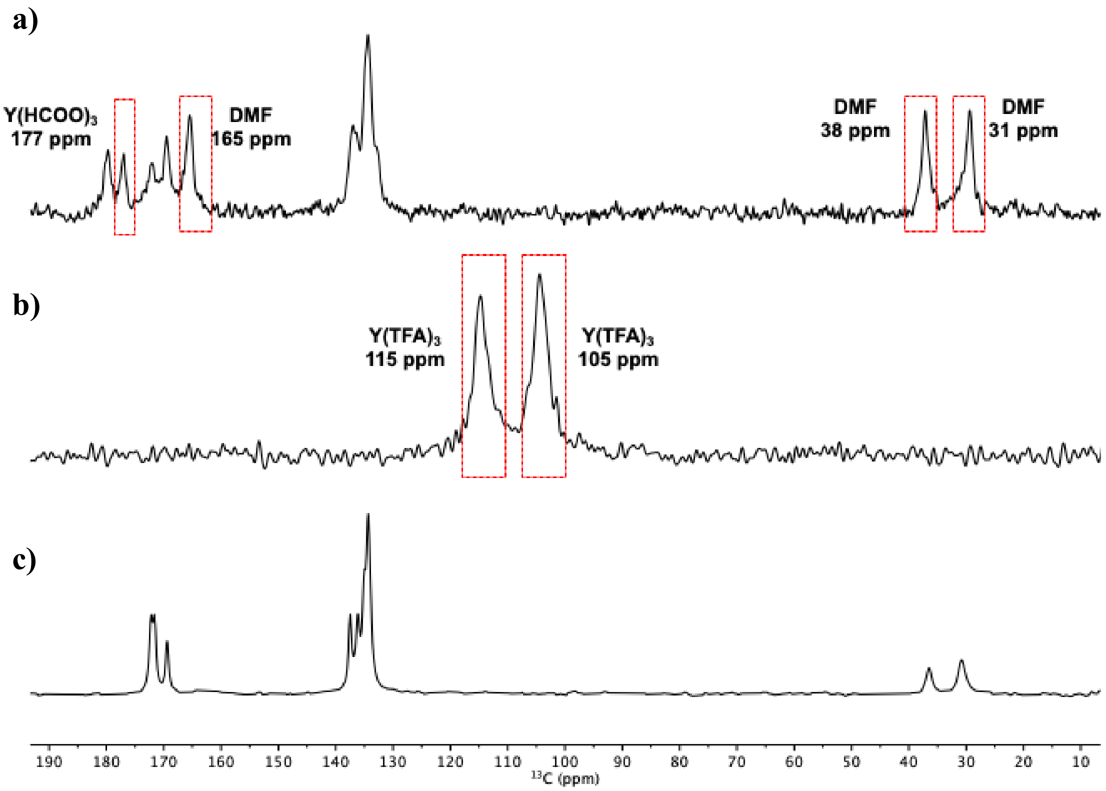

Figure 2.13. ^{13}C SS-NMR spectra of a) CU-45 cross-polarized from ^{1}H, b) CU-45 cross-polarized from ^{19}F, and c) Y-MOF-76 (bottom) synthesized *de novo*.

Solid-state circular dichroism (SS-CD) spectroscopy was performed to observe the chiral character of Y-MOF-76 synthesized *de novo* (Figure 2.14a), vs. that transformed from CU-45 (Figure 2.14c) including in the presence of chiral additives R- and S-limonene. The SS-CD spectrum was recorded between 230 and 700 nm using bulk sample diluted with KBr in the form of a pellet. CU-45 was exposed to R- and S-limonene and ground until the limonene evaporated. The PXRD patterns (Figure 2.14d) confirm that when exposed to chiral additives, CU-45 still undergoes a phase-transformation to Y-MOF-76. The CD spectra demonstrate that Y-MOF-76 preferentially forms one enantiomer *de novo*, and that same enantiomer is formed during the transformation from CU-45, even in the presence of chiral additives (Figure 2.14).

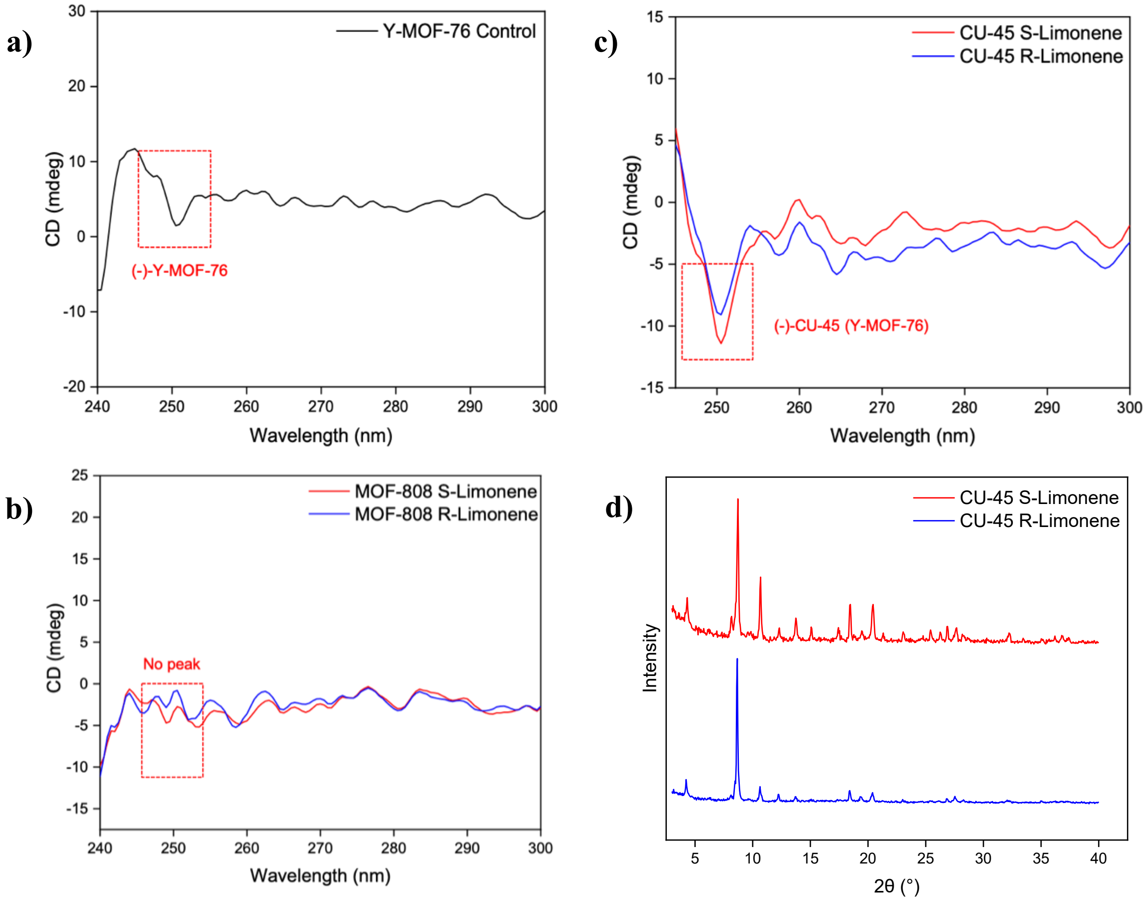

Figure 2.14. SS-CD spectrum of a) Y-MOF-76, b) MOF-808 in R- and S-Limonene, c) CU-45 in R- and S-Limonene, and d) PXRD patterns of CU-45 following the addition of chiral additive R- and S-limonene. All SS-CD performed with background KBr pellet with R- and S- limonene.

2.4. Conclusions

In conclusion, we report a novel rare-earth metal–organic framework (RE-MOF) comprised of hexanuclear Y_6–metal clusters and tritopic BTC linkers that assemble to give CU-45. CU-45 is isostructural to the Zr_6-based MOF-808 with **spn** topology. CU-45 was characterized by PXRD, N_2 sorption, TGA, SEM, and ^1H NMR spectroscopy. CU-45, an achiral MOF, was found to undergo a unique structural transformation to give MOF-76, a chiral MOF with **msx** topology comprised of Y-chain nodes. The structural transformation was investigated using VT-PXRD, TGA/DSC, SS-NMR spectroscopy, and supported by DFT calculations. It was determined that the structural transformation is exothermic and occurs on exposure to various external stimuli that include (i) temperature; (ii) pH; (iii) solvent; and (iv) manual grinding. In all cases, CU-45 converts to the $P4_322$ enantiomer of MOF-76, as confirmed by SS-CD, suggesting that the transformation is enantioselective. This study demonstrates that RE-MOFs comprised of hexanuclear clusters with low connectivity can undergo unique structural transformations to generate MOFs with thermodynamically favoured RE-chain nodes, and that this pathway can be harnessed to enantioselectivity generate a chiral RE-MOF.

Chapter 3

Towards enhancing the stability of CU-45: exploring mixed-metal derivatives and lanthanide templating

3.1. Introduction

In recent years, metal–organic frameworks (MOFs), a class of multi-dimensional, porous, and often crystalline materials, have emerged as a class of exciting new candidates for a plethora of potential applications in multidisciplinary fields.[9,238,239] MOFs are assembled via a phenomenon known as reticular chemistry that involves the linking of molecular building blocks (MBBs), which contain metal ions, chains, or clusters and organic linkers, into highly ordered structures.[82,197]

A subset of MOFs are those which contain f-block elements, which can produce beautiful yet complex structures and topologies. Specifically, rare-earth (RE) metals, which include yttrium (III), scandium (III), and the lanthanide series, have been explored to construct RE-cluster nodes that can be used as MOF building blocks.[26,45,240] Due to their high and variable coordination numbers and geometries, the use of RE elements can give rise to MOFs with unusually high connectivity, and complex topologies, while the design and synthesis of RE-MOFs with lower connectivity may be more challenging.[108,206,241] Assembling RE-cluster MOFs with lower node connectivity (*e.g.* 8-, 6-) is greatly desired, as the there are numerous applications that utilize open-metal sites (OMSs) as an advantage.

One the beneficial features of MOFs is the tunability in their design and synthesis. The ability to assemble multifunctional materials through a modified mixed-metal (MM) approach is an attractive option to construct materials that possess multiple potential functionalities.[242] Recently, the MM approach has been explored in developing MM-MOFs with dual emission that can be used for a wide range of luminescence applications. In 2011, Qian, Chen *et al.* reported a mixed-metal Tb(III)/Eu(III)-MOF as a ratiometric temperature sensor.[243] Qian, Chen *et al.* discovered that MM-MOFs containing Tb(III) and Eu(III) display inverse emission intensity changes that change as a function of temperature.

Due to their preference to form RE-oxo/hydroxo chain nodes, constructing RE-cluster MOFs with lower node connectivity (*e.g.* 8-and 6-) is challenging task. In order to circumvent these stability drawbacks, framework materials can achieve structural support through the use of external "templating" molecules. Templating can be defined as the implementation of organic molecules or hydrate metal ions that provide support to a host material to facilitate crystallization.[244] Generally, template molecules may serve numerous functions, however, recently the utilization of template molecules to support difficult-to-construct frameworks, such as MOFs, has been explored.[244–246] Due to the intricate nature of MOF structures and topologies, template molecules provide structure-directing capabilities that provide support to construct these challenging frameworks. In this work, we demonstrate introductory findings on the design, synthesis, and isolation of CU-45 with neodymium oxide (Nd_2O_3) as a template-directing agent to assemble CU-45-Nd_2O_3 with varying Y(III)/Nd(III) molar ratios.

Herein, we report a library of rare-earth (RE) based hexanuclear (RE_6) cluster MOFs with **spn** topology (Figure 3.1) inspired by the structure of the recently reported, CU-45 (CU = Concordia University), comprised of 6-connected Y_6-clusters bridged by 1,3,5-benzenetricarboxylic acid (H_3BTC).[218]

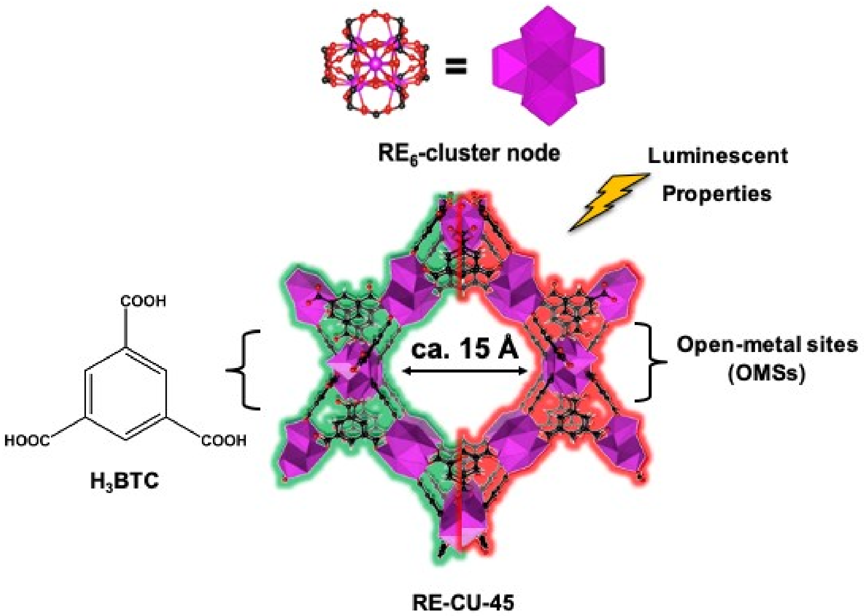

Figure 3.1. Schematic representation of the assembly of RE-CU-45 (lower left) comprised of a RE_6-cluster node and H_3BTC tritopic linker. RE = Y(III), Tb(III), Eu(III), or Er(III). Colour scheme: RE = pink, O = red, and C = black. Hydrogen atoms omitted for clarity.

As illustrated in Figure 3.1, RE-CU-45 is constructed from RE_6-hexanuclear clusters (RE = Y(III), Tb(III), Er(III), and Eu(III)) with H_3BTC giving rise to a 3D framework with an inner pore cavity of approximately 15 Å, and displaying a 3,6-connected **spn** net. Preliminary characterization of these materials was performed using powder X-ray diffraction (PXRD), thermogravimetric analysis (TGA), N_2 sorption isotherms, pore-size distribution (PSD) analysis, and photoluminescence spectroscopy. These preliminary findings show promise towards (i) stabilizing the structure of CU-45 by incorporating Nd_2O_3 template directing agents and (ii) assembling a library of RE-MOFs with luminescent properties to provide a platform to for various potential applications.

3.2. Experimental Procedure

3.2.1. General Materials and Methods

All materials, chemicals and solvents were purchased from commercial suppliers. Yttrium (III) nitrate hydrate (99.9%), terbium (III) nitrate pentahydrate (99.9%), europium (III) nitrate pentahydrate (99.9%), erbium (III) nitrate hydrate (99.9%), 1,3,5-tricarboxylic acid (H_3BTC), and trifluoracetic acid (TFA) were purchased from Alfa Aesar. Neodymium oxide (N_2O_3) was purchased from Stream Chemicals. *N,N*-dimethylformamide (DMF), and potassium bromide (KBr) were purchased from Sigma-Aldrich. Acetone was purchased from Fisher. Liquid Nitrogen (N_2) was purchased from Megs Speciality Gases.

Powder X-ray diffraction (PXRD) data was collected on a Bruker D8 Advance diffractometer equipped with a LYNXEYE linear position sensitive detector (Bruker AXS, Madison, WI). CU-45 was placed onto the low-background sample holder. Data was collected using a continuous coupled $\theta/2\theta$ scan with Ni-filtered Cu$K\alpha$ (λ = 1.54178 Å) radiation operating at 40 kV and 40 mA.

Thermogravimetric analysis coupled with differential scanning calorimetry (TGA/DSC) data was collected on the Mettler Toledo TGA 5500 Discovery. Thermal stability of RE-CU-45 samples were performed from 25 to 800 °C under air (60.00 L/min) with consistent heating of 10 °C per minute. Gas (N_2) adsorption and desorption isotherms for RE-CU-45 were performed using a Micromeritics TriStar II Plus automated surface area and porosity analyzer. The sample tubes were cooled with liquid N_2 before the data was collected.

Photoluminescence measurements were performed on a PTI QuantaMaster 8075 spectrofluorometer (from Horiba). MOF samples were measured by placing MOF on glass slide coated with grease. Solid-state emissions of Tb:Eu-CU-45 and Tb-CU-45 were obtained with an excitation wavelength of 365 nm.

3.2.2. Synthesis and Activation of RE-CU-45 MOFs

3.2.2.1. Synthesis and Activation Er-CU-45 and Tb-CU-45

Synthesis of Er-CU-45. Synthesis of Er-CU-45 was performed by conventional solvothermal methods. $Er(NO_3)_3 \cdot 5H_2O$ (143 mg, 0.41 mmol) was added to a 6-dram vial with 0.6 mL of trifluoroacetic acid (TFA) and 12 mL of *N-N*-dimethylformamide (DMF) and the mixture was placed in the sonicator for ca. 20 minutes. Subsequently, H_3BTC (28 mg, 0.13 mmol) was added to the homogenous solution. The mixture was sonicated once more and placed in an oven at 120 °C and left undisturbed for five days (120 hours). After cooling to room temperature, pink crystal flakes of Er-CU-45 were immersed in fresh DMF, which was replaced three times (3 × 10 mL) throughout the day and soaked overnight. Afterwards, the DMF was removed via centrifugation, and the MOF sample was further soaked in fresh acetone, which was replaced three times (3 × 10 mL) throughout the day and soaked overnight. The product was isolated via centrifugation and left to dry for 24 hours at room temperature. Er-CU-45 was activated with the use of the SmartVac Prep at 100 °C for 20 hours.

Synthesis of Tb-CU-45. Synthesis of Tb-CU-45 was performed by conventional solvothermal methods. $Tb(NO_3)_3 \cdot 5H_2O$ (139 mg, 0.41 mmol) was added to a 6-dram vial with 0.6 mL of trifluoroacetic acid (TFA) and 12 mL of *N-N*-dimethylformamide (DMF) and the mixture was placed in the sonicator for ca. 20 minutes. Subsequently, H_3BTC (28 mg, 0.13 mmol) was added to the homogenous solution. The mixture was sonicated once more and placed in an oven at 120 °C and left undisturbed for five days (120 hours). After cooling to room temperature, white crystal flakes of Tb-CU-45 were immersed in fresh DMF, which was replaced three times (3 × 10 mL) throughout the day and soaked overnight. Afterwards, the DMF was removed via centrifugation, and the MOF sample was further soaked in fresh acetone, which was replaced three times (3 × 10 mL) throughout the day and soaked overnight. The product was isolated via centrifugation and left to dry for 24 hours at room temperature. Tb-CU-45 was activated with the use of the SmartVac Prep at 100 °C for 20 hours.

3.2.2.2. Synthesis and Activation Tb:Eu-CU-45

Synthesis of Tb:Eu-CU-45 (75:25). Tb:Eu-CU-45 (75:25) was synthesized by the addition of $Tb(NO)_3 \cdot 5H_2O$ (51 mg, 0.15 mmol) and $Eu(NO)_3 \cdot 5H_2O$ (33 mg, 0.05 mmol) to a 6-dram vial followed by the addition of trifluoracetic acid (TFA) (0.6 mL) and *N,N*-dimethylformamide (DMF) (12 mL). The heterogenous solution was placed in the sonicator (*ca.* 10 minutes), H_3BTC (28 mg, 0.13 mmol) was added. The mixture was sonicated again to yield a homogenous solution. The mixture was placed in an oven at 120 °C and left undisturbed for 3 days (72 hours). After cooling to room temperature, white-pink crystal flakes of Tb:Eu-CU-45 (75:25) were obtained. The material was washed with DMF (3 × 10 mL) and acetone (3 × 10 mL) and soaked overnight respectively. The final product was isolated via centrifugation and air dried until a fine white crystalline powder was obtained. Tb:Eu-CU-45 (75:25) was activated with the use of the SmartVac Prep at 100 °C for 20 hours.

Synthesis of Tb:Eu-CU-45 (95:5). Tb:Eu-CU-45 (95:5) was synthesized by the addition of $Tb(NO)_3 \cdot 5H_2O$ (65 mg, 0.19 mmol) and $Eu(NO)_3 \cdot 5H_2O$ (7.5 mg, 0.01 mmol) to a 6-dram vial followed by the addition of trifluoracetic acid (TFA) (0.6 mL) and *N,N*-dimethylformamide (DMF) (12 mL). The heterogenous solution was placed in the sonicator (*ca.* 10 minutes), H_3BTC (28 mg, 0.13 mmol) was added. The mixture was sonicated again to yield a homogenous solution. The mixture was placed in an oven at 120 °C and left undisturbed for 3 days (72 hours). After cooling to room temperature, white-pink crystal flakes of Tb:Eu-CU-45 (95:5) were obtained. The material was washed with DMF (3 × 10 mL) and acetone (3 × 10 mL) and soaked overnight respectively. The final product was isolated via centrifugation and air dried until a fine white crystalline powder was obtained. Tb:Eu-CU-45 (95:5) was activated with the use of the SmartVac Prep at 100 °C for 20 hours.

3.2.2.3. Synthesis and Activation CU-45-Nd_2O_3

Synthesis CU-45-Nd_2O_3 (90:10). CU-45-Nd_2O_3 (90:10) was synthesized by the addition of $Y(NO)_3 \cdot xH_2O$ (213 mg, 0.56 mmol) to a 6-dram vial followed by the addition of Nd_2O_3 (20 mg, 0.006 mmol), trifluoracetic acid (TFA) (0.6 mL), and *N,N*-dimethylformamide (DMF) (12 mL). The heterogenous solution was placed in the sonicator (*ca.* 10 minutes) and H_3BTC (25 mg, 0.12 mmol) was added was added. The mixture was sonicated again to yield a homogenous solution. The mixture was placed in an oven at 120 °C and left undisturbed for 3 days (72 hours). After cooling to room temperature, fine purple-white crystals of CU-45-Nd_2O_3 (90:10) were obtained.

The material was washed with DMF (3 × 10 mL) and acetone (3 × 10 mL) and soaked overnight respectively. The final product was isolated via centrifugation and air dried until a fine white crystalline powder was obtained. CU-45-Nd_2O_3 (90:10) was activated with the use of the SmartVac Prep at 100 °C for 20 hours.

Synthesis CU-45-Nd_2O_3 (95:5). CU-45-Nd_2O_3 (95:5) was synthesized by the addition of $Y(NO)_3 \cdot xH_2O$ (225 mg, 0.59 mmol) to a 6-dram vial followed by the addition of Nd_2O_3 (16 mg, 0.003 mmol), trifluoracetic acid (TFA) (0.6 mL), and *N,N*-dimethylformamide (DMF) (12 mL). The heterogenous solution was placed in the sonicator (*ca.* 10 minutes) and H_3BTC (26 mg, 0.123 mmol) was added was added. The mixture was sonicated again to yield a homogenous solution. The mixture was placed in an oven at 120 °C and left undisturbed for 3 days (72 hours). After cooling to room temperature, fine purple-white crystals of CU-45-Nd_2O_3 (95:5) were obtained. The material was washed with DMF (3 × 10 mL) and acetone (3 × 10 mL) and soaked overnight respectively. The final product was isolated via centrifugation and air dried until a fine white crystalline powder was obtained. CU-45-Nd_2O_3 (95:5) was activated with the use of the SmartVac Prep at 100 °C for 20 hours.

3.3. Results and Discussion

3.3.1. Synthesis, Characterization, and Activation of RE-CU-45

Isostructural RE-CU-45 materials were synthesized using standard solvothermal conditions by reacting RE-metal nitrate precursors (See section 3.2.2.1) with H_3BTC in DMF with 0.6 mL of TFA as a modulator, at temperatures of 120 ºC for approximately 5 days. Given that these MOFs are isostructural to CU-45, the PXRD patterns (Figure 3.2) of RE-CU-45 (RE = Tb (III) and Er (III)) resemble that of the previously reported Y derivative (Chapter 2).[43] The PXRD pattern shown in Figure 3.2. confirms the bulk crystallinity, phase purity, and **spn** topology of these samples.

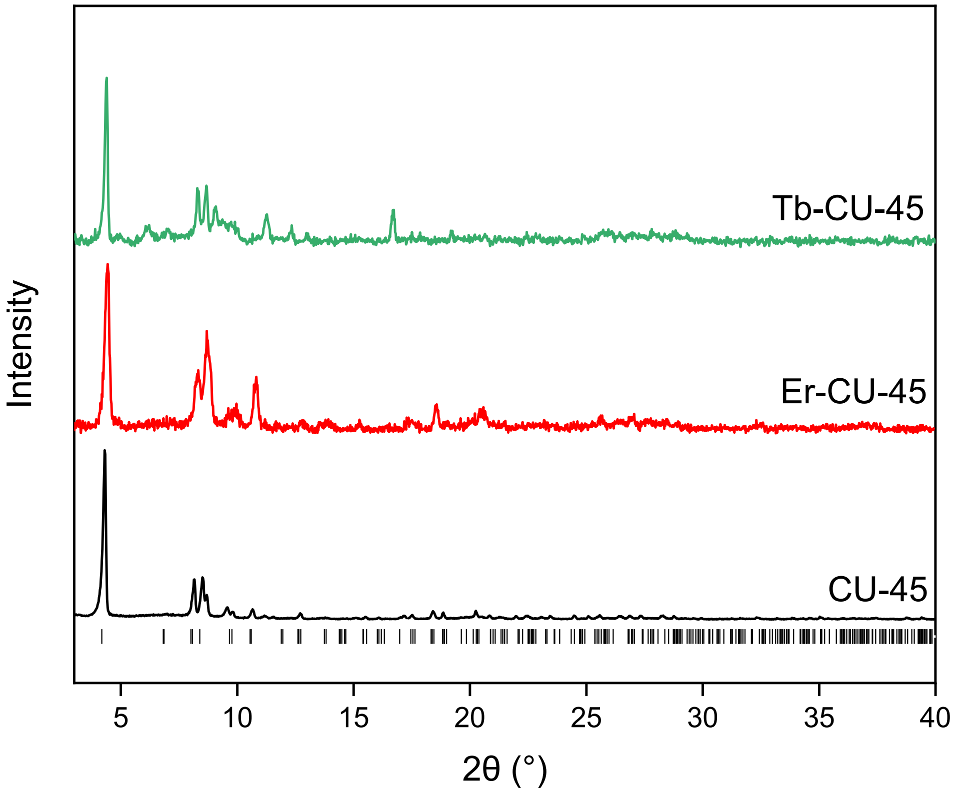

Figure 3.2. PXRD patterns of RE-CU-45 isostructures constructed with Tb (III) and Er(III) synthesized *de novo* and compared to experimental pattern of Y-based CU-45.

In addition to RE-CU-45 derivatives, mixed-metal (RE/RE)-CU-45 materials were synthesized using standard solvothermal conditions by reacting RE-metals with varying molar ratios (See section 3.2.2.1) with H_3BTC in TFA and DMF at 120 °C for three days. PXRD patterns for Tb:Eu-CU-45 (95:5) (Figure 3.3a) and Tb:Eu-CU-45 (75:25) (Figure 3.3b) confirm bulk crystallinity and desired **spn** topology, with prominent reflections at 4.4 (2θ) and two characteristic smaller reflections at 8.4 and 8.6 (2θ) respectively.

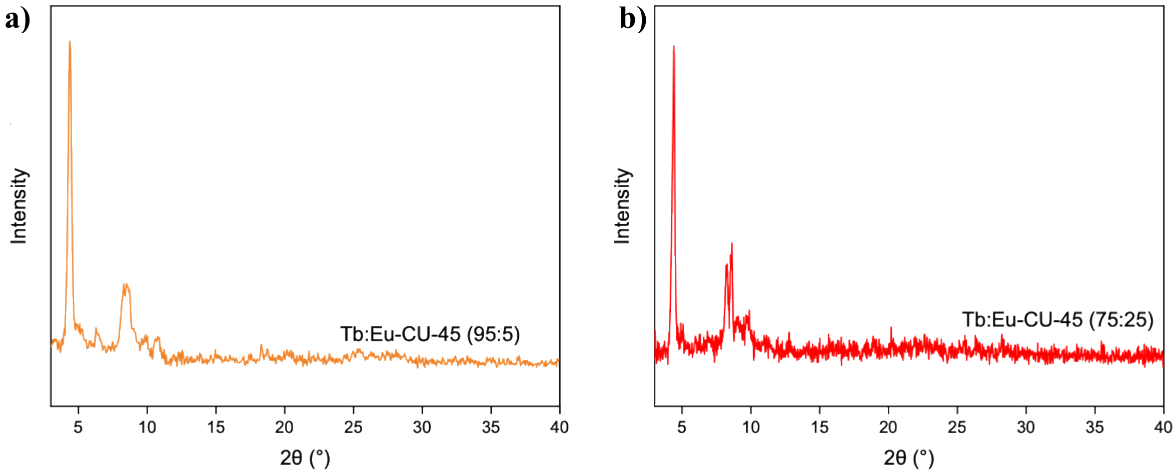

Figure 3.3. PXRD patterns of mixed-metal RE-CU-45. a) Tb:Eu-CU-45 (95% Tb(III), 5% Eu(III)); b) Tb:Eu-CU-45 (75% Tb(III), 25% Eu(III)).

RE-CU-45 isostructures were activated at 100 °C under vacuum for 20 hours, and nitrogen sorption analysis for Tb-, Er-, Tb:Eu-CU-45 (95:5) and (75:25) reveals Type I isotherms (Figure 3.4a and b) for all materials, giving rise to BET surface areas of 105, 305, 55, and 75 m^2/g respectively. While the BET surfaces are lower than that found for CU-45, and much lower than the expected value of ~1500 m^2/g for Zr_6-MOF-808, the isotherm shape and pore size distribution analysis is consistent with that expected. Future work should involve exploring optimal activation procedures for these derivatives.

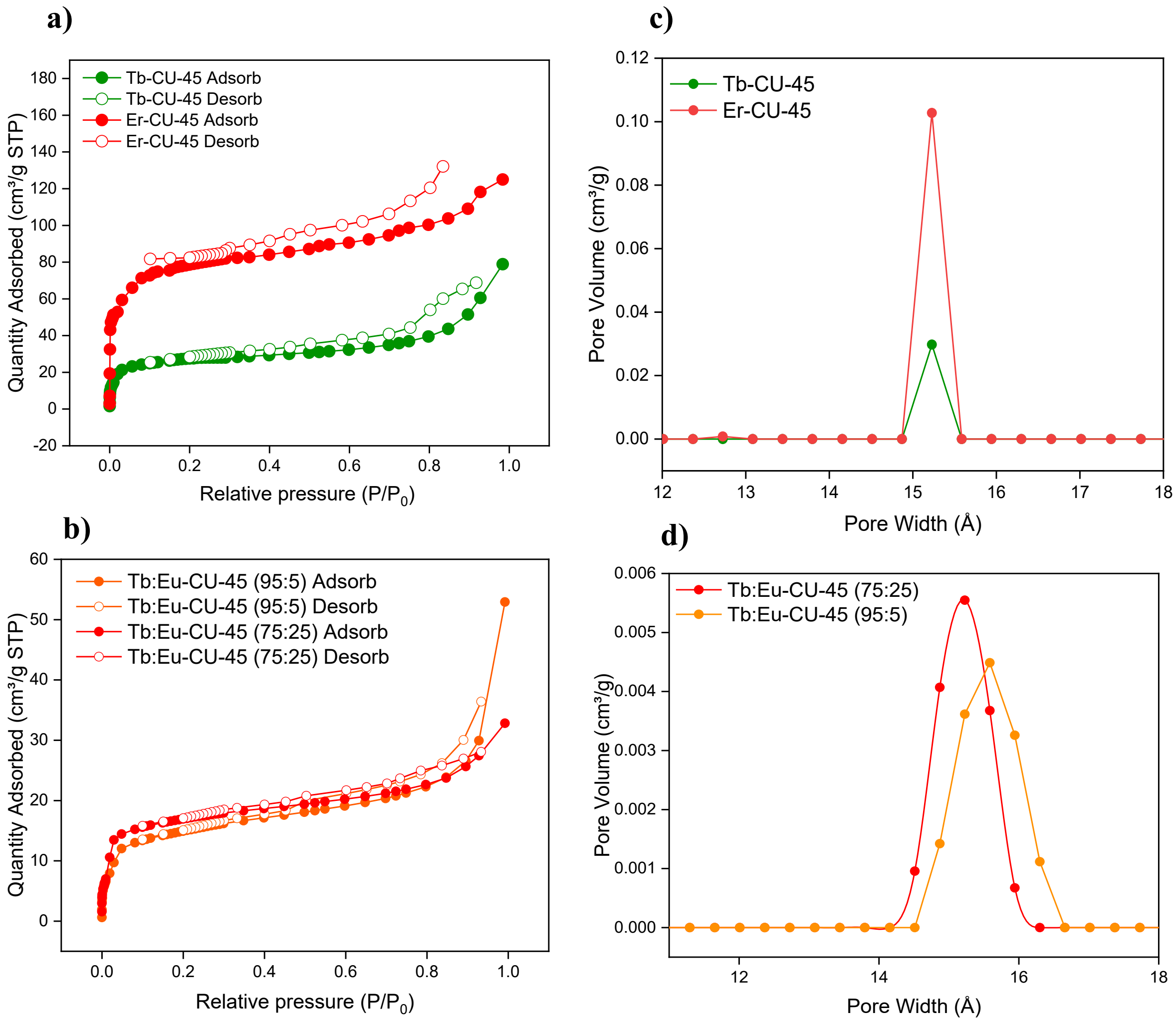

Figure 3.4. N_2 adsorption-desorption isotherms for a) Tb- and Er-CU-45, and b) Tb:Eu-CU-45 (95:5) and (75:25). PSD analysis of c) Tb- and Er-CU-45 and d) Tb:Eu-CU-45 (95:5) and (75:25).

PSD analysis (Figure 3.4c and d) confirms the presence of pores with diameters of 15.2, 15.9, 15.9, and 15.6 Å for Tb-CU-45, Er-CU-45, Tb:Eu-CU-45 (75:25), and Tb:Eu-CU-45 (95:5) respectively. The PXRD, BET, and PSD analysis for these RE-CU-45 are consistent with previously synthesized CU-45 and confirm **spn** topology.

The thermal stabilities of Tb-CU-45 (Figure 3.5a), Tb:Eu-CU-45 (75:25) and (95:5) (Figure 3.5b) were measured following activation at 100 °C for 20 hours by thermogravimetric analysis (TGA). TGA measurements of Tb-CU-45, Tb:Eu-CU-45 (75:25), and Tb:Eu-CU-45 (95:5) were performed under air from 25 to 800 °C where distinct TGA curves are observed for each of the four RE-CU-45 materials, providing evidence that these RE-MOFs possess similar thermal stabilities with decomposition occurring around 550 °C.

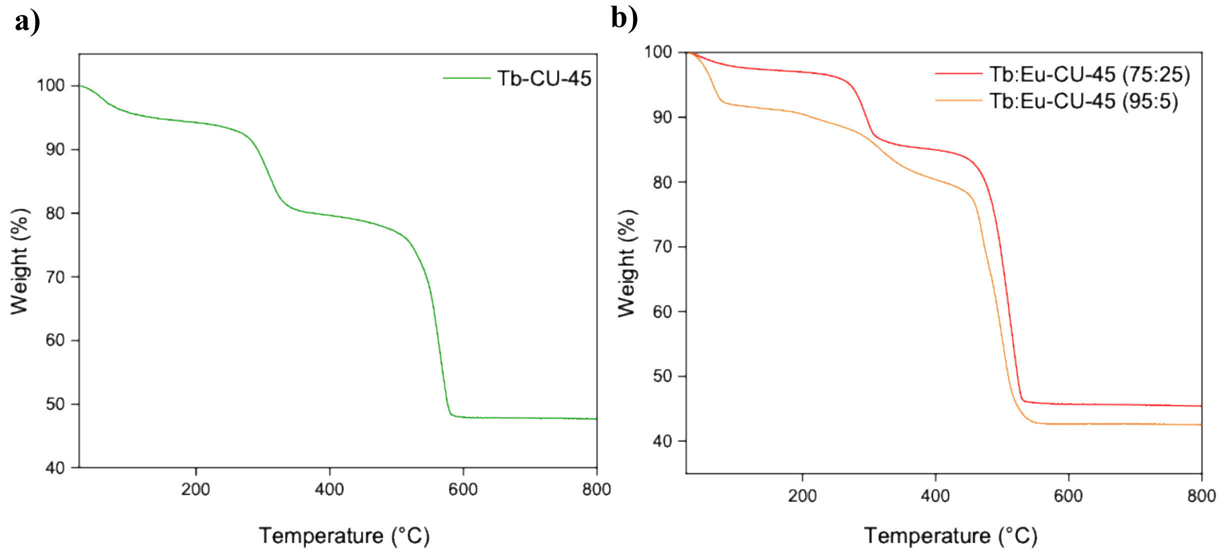

Figure 3.5. TGA curves of a) Tb- and Er-CU-45 and b) Tb:Eu-CU-45 (95:5) and (75:25). TGA measurements were performed under air from 25 to 800 °C.

To understand the luminescent properties of these RE derivatives of CU-45, Tb-CU-45, Tb:Eu-CU-45 (95:5) and (75:25) were investigated using photoluminescence spectroscopy. Tb-CU-45 exhibited bright green emission, with the solid-state emission spectrum displaying four characteristic Tb(III) emissions peaks at 485, 545, 585, and 625 nm, when excited at 365 nm at room temperature. Emission results from the disbandment of the $^5D_4$ excited state to the ^7F_J ground state of the Tb(III) metal (J = 6, 5, 4, and 3), and the emission spectrum exhibits a strong characteristic peak at 545 nm that is attributed to $^5D_4 \rightarrow {}^7F_5$ transition.[247–249]

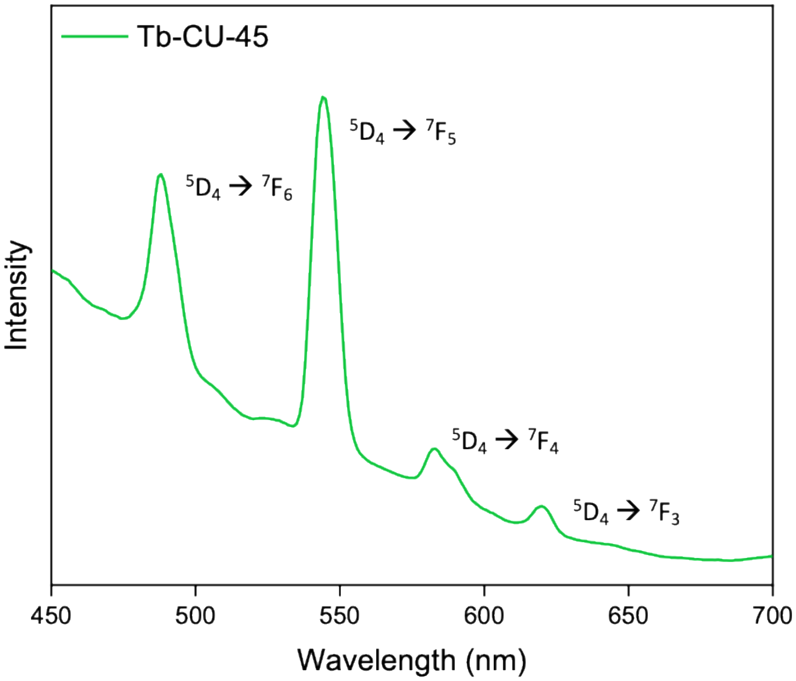

Figure 3.6. The solid-state emission spectrum of Tb-CU-45 excited at 365 nm.

The assembly of multiple luminescent centers with varying emission properties in a single material is an attractive trait due to the ability to achieve dual emission for ratiometric sensing.[250] The solid-state emission spectra of MM-CU-45 materials, Tb:Eu-CU-45 (95:5) and (75:25) are shown in Figure 3.7. For both MM-CU-45 materials, bright red emission is observed, regardless of the quantity of Tb(III) metal. The solid-state luminescence spectrum of Tb:Eu-CU-45 (95:5) demonstrates four emissions peaks of varying intensity at 540, 583, 623, and 655 nm, when excited at 365 nm at room temperature. While this material contains predominantly Tb(III) ions, the intense peaks can be attributed to the deactivation of $^5D_0$ excited state to the ^7F_J ground state of the Eu(III), which is due to the disbandment of $^5D_0$ excited state to the ^7F_J ground state of the Tb(III) ion (J = 0, 1, 2, 3, and 4).[243,247]

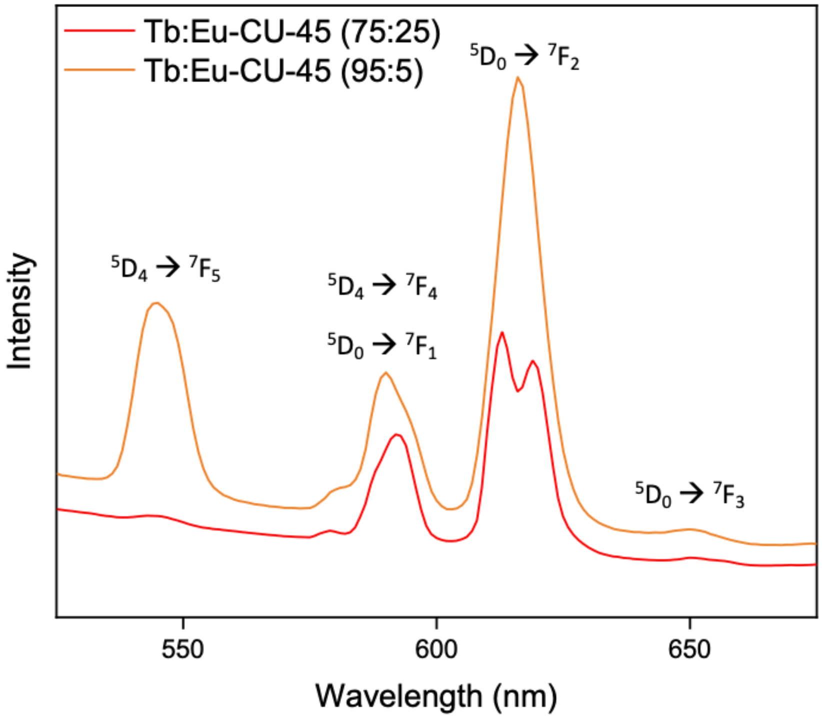

Figure 3.7. Solid-state emission spectra of MM-CU-45, Tb:Eu-CU-45 (95:5) and (75:25) excited at 365 nm at room temperature.

The strongest peaks observed are attributed to the $^5D_0 \rightarrow {}^7F_1$ (583 nm) and $^5D_0 \rightarrow {}^7F_2$ (623 nm), additionally, characteristic transitions of $^5D_4 \rightarrow {}^7F_5$ and $^5D_4 \rightarrow {}^7F_4$ for Tb(III) are found at 540 and 585 nm respectively. On the other hand, increasing the Eu(III) concentration in Tb:Eu-CU-45 (75:25) leads emission quenching of the peak observed at 540, characteristic for $^5D_4 \rightarrow {}^7F_5$ transition in the Tb(III) metal, while demonstrating reduced intensity for peaks at 585, 610, and 630 nm.

3.3.2. Preliminary Investigation to RE$_6$-cluster Stabilization

As previously reported in Chapter 2, CU-45, a Y$_6$-based RE-MOF undergoes a structural transformation in response to numerous external stimuli. It is hypothesized that embedding small molecules capable of taking part in intermolecular interactions with the framework material, can serve to stabilize the structure and prevent the transformation from taking place.[72,244,245] In order to establish a preliminary template-directed synthesis method, neodymium oxide (Nd_2O_3) was used as structure-directing agent.

CU-45-Nd_2O_3 materials were synthesized using standard solvothermal conditions (See Section 3.2.2.2) by reacting varying amounts of $Y(NO)_3{\cdot}6H_2O$ with Nd_2O_3, and H_3BTC, in DMF with 0.6 mL of TFA added as a modulator at 130 °C for three days. As these templated materials are expected to be isostructures of CU-45, the expected PXRD patterns (Figure 3.8) confirm bulk crystallinity, and phase purity with characteristic reflections at approximately 4.5, 8.5 and 8.7 (2θ) respectively. With the addition of varying mole percent of Nd_2O_3 as a structure-directing template, CU-45-Nd_2O_3 (Y = 90; Nd_2O_3 = 10) and (Y = 95; Nd_2O_3 = 5), the phase purity of CU-45 was significantly improved.

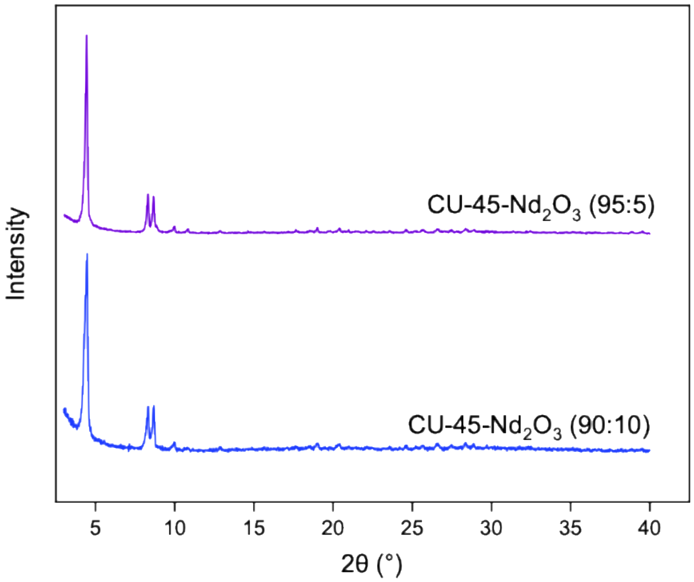

Figure 3.8. PXRD patterns of CU-45-Nd_2O_3 (90:10) and (95:5), utilizing Nd_2O_3 as structure-directing agent.

To measure the porosity and BET surface areas of these materials, CU-45-Nd_2O_3 (90:10) and (95:5) were activated under vacuum for 20 hours at 100 °C. The N_2 sorption isotherms (Figure 3.9a) reveal Type I behaviour with BET surface areas of 470 m^2/g for CU-45-Nd_2O_3 (90:10) and 585 m^2/g for CU-45-Nd_2O_3 (95:5). PSD analysis (Figure 3.9b) confirms the presence of inner pore size of 15.5 and 15.9 Å for CU-45-Nd_2O_3 (90:10) and (95:5) respectively. The preliminary synthetic procedure of implementing 10 and 5% Nd_2O_3 into the CU-45 framework, and PXRD, BET, and PSD data, demonstrate potential for developing CU-45 materials with higher crystallinity, phase purity, and stability.

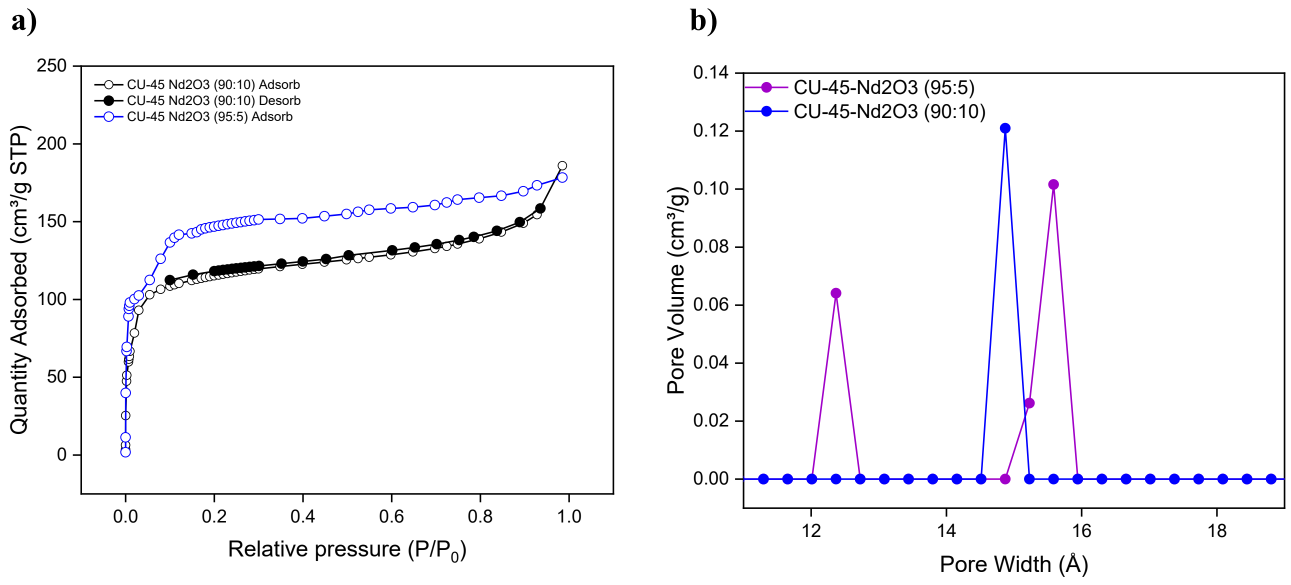

Figure 3.9. a) N_2 sorption isotherms for CU-45-Nd_2O_3 (95:5) and (90:10), b) PSD analysis of CU-45-Nd_2O_3 (95:5) and (90:10).

3.4. Conclusions

In conclusion, we report the synthesis of five novel derivatives of the rare-earth metal–organic framework, CU-45. RE-CU-45 (RE = Y(III), Tb(III), Er(III), and Eu(III); CU = Concordia University) were assembled with hexanuclear metal or MM-clusters, RE_6, and commercially available tritopic linkers, H_3BTC to construct MOFs with desirable **spn** topology. Additionally, the incorporation of a structure-directing molecule, Nd_2O_3, to stabilize CU-45 was investigated.

The structural properties of RE-CU-45 and CU-45-Nd_2O_3 were investigated with PXRD, TGA, N_2 sorption, BET surface area, and PSD analysis. The characterization results for all these materials are consistent physical and structural characteristics of CU-45 with **spn** topology. Preliminary findings show that the incorporation of structure-directing molecule, Nd_2O_3 increases the crystallinity, stability, and phase purity of CU-45.

Furthermore, initial investigation to the MM-CU-45 luminescent properties were explored through solid-state photoluminescence to investigate their capabilities as luminescent sensors. Findings for Tb:Eu-CU-45 (95:5) and (75:25) demonstrate strong and characteristic emissions, providing possibility to achieve luminescent materials.

Chapter 4

Conclusions and Future Work

4.1. General Conclusions

Constructing MOFs with lower-connectivity RE-clusters provides a plethora of synthetic challenges. However, we have established a reproducible, solvothermal procedure that utilizes a fluorinated modulator, commercially available tritopic carboxylic acid linker, and a 6-connected RE-metal cluster to assemble CU-45 (CU = Concordia University). CU-45 is comprised of hexanuclear Y_6-cluster nodes, bridged by benzene-1,3,5-tricarboxylic acid, forming a framework that is isostructural to Zr_6-based MOF-808 with **spn** topology. CU-45 was successfully synthesized, isolated, and activated, and characterized. Exposure of CU-45 to various external stimuli such as pH, solvent polarity, pressure, and elevated temperatures enables a crystalline-to-crystalline phase transformation to give a chiral MOF comprised of Y-chain nodes, Y-MOF-76. Theoretical and experimental results demonstrate that Y-MOF-76 is the thermodynamic product, while CU-45 is the kinetic product. In chapter 2, we presented detailed characterization, including TGA/DSC, VT-PXRD, SS-^{13}C NMR, and SS-CD, to understand the details of this unique achiral-to-chiral, crystalline-to-crystalline phase transition.

Using the Y(III) analogue of CU-45 as a blueprint, four novel RE-CU-45 isostructures, with Tb(III), Er(III) and mixed-metals Tb(III)/Eu(III) were successfully synthesized. A preliminary investigation of the structural and optical properties of these frameworks was carried out using PXRD, N_2-sorption, TGA, and photoluminescence spectroscopy. This work provides insight into the development of RE-CU-45 derivatives with OMSs and luminescent properties to study as a platform for potential sensing applications.

In an attempt to circumvent the transformation of RE-CU-45 to MOF-76, template-directed synthesis was investigated. CU-45 was successfully synthesized using Nd_2O_3 as a templating agent, and the material was characterized using PXRD and N_2-sorption. By implementing 5 and 10% mole percent of Nd_2O_3 in the synthesis of CU-45, highly crystalline materials are assembled, with superior surface areas.

4.2. Future Work

Future work should focus on constructing a library of RE-CU-45 materials, and optimization of reaction conditions. Further exploration of the solvothermal synthesis of CU-45, with and without templating agents, is required to achieve higher crystallinity and phase purity. While the current method (Chapters 2 and 3) is successful for producing RE-CU-45, it may be of interest to explore the synthetic conditions further by tuning metal (M), linker (L), modulator (X), and solvent ratios for further optimization.

Furthermore, to harness porosity, OMSs, and luminescent properties of CU-45, a synthetic procedure that stabilizes the MOF and prevents the structural transformation to MOF-76 should be developed. This works can provide a foundation for the synthesis of RE-MOFs with **spn** topology and varying linker configurations (*e.g.* 1,3,5-benzenetricarboxylic acid (H_3BTB), 1,3,5-tris(4'-carboxy[1,1'-biphenyl]-4-yl)benzene (H_3BBC), and 1,3,5-triscarboxyphenylethynylbenzene (H_3BTE)) and/or RE-metal ions in the near future.

While the initial success of constructing five novel RE-CU-45 materials is encouraging, further experimental analysis needs to be performed on the Tb(III), Er(III), and Tb(III)/Eu(III) derivatives. First, to provide robust evidence of the incorporation of the metals, inductively coupled plasma mass spectrometry (ICP-MS) must be performed. Second, scanning electron microscopy (SEM) should be performed to obtain information on the crystalline morphology and size. When coupled with energy dispersive X-ray spectroscopy (EDS), information on the metal dispersion/incorporation in RE-CU-45 can be obtained for comparison with ICP-MS results. Finally, all the derivatives of CU-45 (synthesized with and without templating agents) should be exposed to external stimuli to ascertain whether the material transforms into various derivatives of MOF-76. If stabilization of CU-45 derivatives is possible, then full characterization, investigation of luminescent properties, and potential sensing applications should be explored.

References

(1) Tomic, E. A. *J. Appl. Polym. Sci.* **1965**, *9* (11), 3745–3752.

(2) Hoskins, B. F.; Robson, R. *J. Am. Chem. Soc.* **1989**, *111* (15), 5962–5964.

(3) Yaghi, O. M.; Li, H. *J. Am. Chem. Soc.* **1995**, *117* (41), 10401–10402.

(4) Li, H.; Eddaoudi, M.; O'Keeffe, M.; Yaghi, O. M. *Nature* **1999**, *402* (6759), 276–279.

(5) Kondo, M.; Yoshitomi, T.; Matsuzaka, H.; Kitagawa, S.; Seki, K. *Angew. Chem. Int. Ed.* **1997**, *36* (16), 1725–1727.

(6) Hoskins, B. F.; Robson, R. *J. Am. Chem. Soc.* **1989**, *111* (15), 5962–5964.

(7) Yaghi, O. M.; Li, H. *J. Am. Chem. Soc.* **1995**, *117* (41), 10401–10402.

(8) Yaghi, O. M.; Li, G.; Li, H. *Nature* **1995**, *378* (6558), 703–706.

(9) Cheetham, A. K.; Férey, G.; Loiseau, T. *Angew. Chem. Int. Ed.* **1999**, *38* (22), 3268–3292.

(10) Rosi, N. L.; Kim, J.; Eddaoudi, M.; Chen, B.; O'Keeffe, M.; Yaghi, O. M. *J. Am. Chem. Soc.* **2005**, *127* (5), 1504–1518.

(11) Joseph, N.; Lawson, H. D.; Overholt, K. J.; Damodaran, K.; Gottardi, R.; Acharya, A. P.; Little, S. R. *Sci. Rep.* **2019**, *9* (1), 1–11.

(12) Robison, L.; Zhang, L.; Drout, R. J.; Li, P.; Haney, C. R.; Brikha, A.; Noh, H.; Mehdi, B. L.; Browning, N. D.; Dravid, V. P.; Cui, Q.; Islamoglu, T.; Farha, O. K. *ACS Appl. Bio Mater.* **2019**, *2* (3), 1197–1203.

(13) Férey, G.; Latroche, M.; Serre, C.; Millange, F.; Loiseau, T.; Percheron-Guégan, A. *Chem. Commun.* **2003**, No. 24, 2976–2977.

(14) Feng, D.; Gu, Z.-Y.; Li, J.-R.; Jiang, H.-L.; Wei, Z.; Zhou, H.-C. *Angew. Chem. Int. Ed.* **2012**, *51* (41), 10307–10310.

(15) Feng, D.; Wang, K.; Wei, Z.; Chen, Y.-P.; Simon, C. M.; Arvapally, R. K.; Martin, R. L.; Bosch, M.; Liu, T.-F.; Fordham, S.; Yuan, D.; Omary, M. A.; Haranczyk, M.; Smit, B.; Zhou, H.-C. *Nat. Commun* **2014**, *5* (1), 1–9.

(16) Phan, A.; Doonan, C. J.; Uribe-Romo, F. J.; Knobler, C. B.; O'Keeffe, M.; Yaghi, O. M. *Acc. Chem. Res.* **2010**, *43* (1), 58–67.

(17) Xue, D.-X.; Cairns, A. J.; Belmabkhout, Y.; Wojtas, L.; Liu, Y.; Alkordi, M. H.; Eddaoudi, M. *J. Am. Chem. Soc.* **2013**, *135* (20), 7660–7667.

(18) Dolgopolova, E. A.; Rice, A. M.; Shustova, N. B. *Chem. Commun.* **2018**, *54* (50), 6472–6483.

(19) Lee, Y.-R.; Kim, J.; Ahn, W.-S. *Korean J. Chem. Eng.* **2013**, *30* (9), 1667–1680.

(20) Ockwig, N. W.; Delgado-Friedrichs, O.; O'Keeffe, M.; Yaghi, O. M. *Acc. Chem. Res.* **2005**, *38* (3), 176–182.

(21) Alezi, D.; Peedikakkal, A. M. P.; Weseliński, Ł. J.; Guillerm, V.; Belmabkhout, Y.; Cairns, A. J.; Chen, Z.; Wojtas, Ł.; Eddaoudi, M. *J. Am. Chem. Soc.* **2015**, *137* (16), 5421–5430.

(22) Ma, S.; Zhou, H.-C. *J. Am. Chem. Soc.* **2006**, *128* (36), 11734–11735.

(23) Mason, J. A.; Veenstra, M.; Long, J. R. *Chem. Sci.* **2013**, *5* (1), 32–51.

(24) Otake, K.; Cui, Y.; Buru, C. T.; Li, Z.; Hupp, J. T.; Farha, O. K. *J. Am. Chem. Soc.* **2018**, *140* (28), 8652–8656.

(25) Lee, J.; Farha, O. K.; Roberts, J.; Scheidt, K. A.; Nguyen, S. T.; Hupp, J. T. *Chem. Soc. Rev.* **2009**, *38* (5), 1450–1459.

(26) Yang, D.; Gates, B. C. *ACS Catal.* **2019**, *9* (3), 1779–1798.

(27) Howarth, A. J.; Liu, Y.; Hupp, J. T.; Farha, O. K. *CrystEngComm* **2015**, *17* (38), 7245–7253.

(28) Drout, R. J.; Robison, L.; Chen, Z.; Islamoglu, T.; Farha, O. K. *Trends Chem* **2019**, *1* (3), 304–317.

(29) Kobielska, P. A.; Howarth, A. J.; Farha, O. K.; Nayak, S. *Coord. Chem. Rev.* **2018**, *358*, 92–107.

(30) Horcajada, P.; Serre, C.; Maurin, G.; Ramsahye, N. A.; Balas, F.; Vallet-Regí, M.; Sebban, M.; Taulelle, F.; Férey, G. *J. Am. Chem. Soc.* **2008**, *130* (21), 6774–6780.

(31) Orellana-Tavra, C.; Marshall, R. J.; Baxter, E. F.; Lázaro, I. A.; Tao, A.; Cheetham, A. K.; Forgan, R. S.; Fairen-Jimenez, D. *J. Mater. Chem. B* **2016**, *4* (47), 7697–7707.

(32) Cui, Y.; Li, B.; He, H.; Zhou, W.; Chen, B.; Qian, G. *Acc. Chem. Res.* **2016**, *49* (3), 483–493.

(33) Cui, Y.; Yue, Y.; Qian, G.; Chen, B. *Chem. Rev.* **2012**, *112* (2), 1126–1162.

(34) Rao, X.; Huang, Q.; Yang, X.; Cui, Y.; Yang, Y.; Wu, C.; Chen, B.; Qian, G. *J. Mater. Chem.* **2012**, *22* (7), 3210–3214.

(35) Kreno, L. E.; Leong, K.; Farha, O. K.; Allendorf, M.; Van Duyne, R. P.; Hupp, J. T. *Chem. Rev.* **2012**, *112* (2), 1105–1125.

(36) Bauer, C. A.; Timofeeva, T. V.; Settersten, T. B.; Patterson, B. D.; Liu, V. H.; Simmons, B. A.; Allendorf, M. D. *J. Am. Chem. Soc.* **2007**, *129* (22), 7136–7144.

(37) Faust, T. *Nat. Chem.* **2016**, *8* (11), 990–991.

(38) *Nat. Chem.* **2016**, *8* (11), 987–987.

(39) Yaghi, O. M.; O'Keeffe, M.; Ockwig, N. W.; Chae, H. K.; Eddaoudi, M.; Kim, J. *Nature* **2003**, *423* (6941), 705–714.

(40) Yaghi, O. M. *J. Am. Chem. Soc.* **2016**, *138* (48), 15507–15509.

(41) Yaghi, O. M. *ACS Cent. Sci.* **2019**, *5* (8), 1295–1300.

(42) Öhrström, L. *Crystals* **2015**, *5* (1), 154–162.

(43) O'Keeffe, M.; Peskov, M. A.; Ramsden, S. J.; Yaghi, O. M. *Acc. Chem. Res.* **2008**, *41* (12), 1782–1789.

(44) Furukawa, H.; Ko, N.; Go, Y. B.; Aratani, N.; Choi, S. B.; Choi, E.; Yazaydin, A. O.; Snurr, R. Q.; O'Keeffe, M.; Kim, J.; Yaghi, O. M. *Science* **2010**, *329* (5990), 424–428.

(45) Hönicke, I. M.; Senkovska, I.; Bon, V.; Baburin, I. A.; Bönisch, N.; Raschke, S.; Evans, J. D.; Kaskel, S. *Angew. Chem. Int. Ed.* **2018**, *57* (42), 13780–13783.

(46) Li, P.; Vermeulen, N. A.; Malliakas, C. D.; Gómez-Gualdrón, D. A.; Howarth, A. J.; Mehdi, B. L.; Dohnalkova, A.; Browning, N. D.; O'Keeffe, M.; Farha, O. K. *Science* **2017**, *356* (6338), 624–627.

(47) *Chem. Rev.* **2012**, *112* (2), 673–674.

(48) Bai, Y.; Dou, Y.; Xie, L.-H.; Rutledge, W.; Li, J.-R.; Zhou, H.-C. *Chem. Soc. Rev.* **2016**, *45* (8), 2327–2367.

(49) Li, B.; Wen, H.-M.; Cui, Y.; Zhou, W.; Qian, G.; Chen, B. *Adv. Mater.* **2016**, *28* (40), 8819–8860.

(50) Pagis, C.; Ferbinteanu, M.; Rothenberg, G.; Tanase, S. *ACS Catal.* **2016**, *6* (9), 6063–6072.

(51) Cui, Y.; Chen, B.; Qian, G. *Coord. Chem. Rev.* **2014**, *273–274*, 76–86.

(52) Seitz, M.; Oliver, A. G.; Raymond, K. N. *J. Am. Chem. Soc.* **2007**, *129* (36), 11153–11160.

(53) Fordham, S.; Wang, X.; Bosch, M.; Zhou, H.-C. In *Lanthanide Metal-Organic Frameworks*; Cheng, P., Ed.; Springer Berlin Heidelberg: Berlin, Heidelberg, 2014; Vol. 163, pp 1–27.

(54) Jiang, H.; Jia, J.; Shkurenko, A.; Chen, Z.; Adil, K.; Belmabkhout, Y.; Weselinski, L. J.; Assen, A. H.; Xue, D.-X.; O'Keeffe, M.; Eddaoudi, M. *J. Am. Chem. Soc.* **2018**, *140* (28), 8858–8867.

(55) Yang, L.-Z.; Wang, J.; Kirillov, A. M.; Dou, W.; Xu, C.; Fang, R.; Xu, C.-L.; Liu, W.-S. *CrystEngComm* **2016**, *18* (34), 6425–6436.

(56) Zhang, H.; Fan, R.; Chen, W.; Fan, J.; Dong, Y.; Song, Y.; Du, X.; Wang, P.; Yang, Y. *Cryst. Growth Des* **2016**, *16* (9), 5429–5440.

(57) Akhtar, M. N.; Chen, Y.-C.; AlDamen, M. A.; Tong, M.-L. *Dalton Trans.* **2017**, *46* (1), 116–124.

(58) Medina-Velazquez, D. Y.; Alejandre-Zuniga, B. Y.; Loera-Serna, S.; Ortiz, E. M.; Morales-Ramirez, A. de J.; Garfias-Garcia, E.; Garcia-Murillo, A.; Falcony, C. *J. Nanopart Res.* **2016**, *18* (12), 352.

(59) Rong, J.; Zhang, W.; Bai, J. *CrystEngComm* **2016**, *18* (40), 7728–7736.

(60) Rybak, J.-C.; Meyer, L. V.; Wagenhöfer, J.; Sextl, G.; Müller-Buschbaum, K. *Inorg. Chem.* **2012**, *51* (24), 13204–13213.

(61) Fang, S.-M.; Sañudo, E. C.; Hu, M.; Zhang, Q.; Ma, S.-T.; Jia, L.-R.; Wang, C.; Tang, J.-Y.; Du, M.; Liu, C.-S. *Cryst. Growth Des.* **2011**, *11* (3), 811–819.

(62) Hoffart, D. J.; Loeb, S. J. *Angew. Chem. Int. Ed. Engl.* **2005**, *44* (6), 901–904.

(63) He, Y.; Furukawa, H.; Wu, C.; O'Keeffe, M.; Chen, B. *CrystEngComm* **2013**, *15* (45), 9328–9331.

(64) Schoedel, A.; Li, M.; Li, D.; O'Keeffe, M.; Yaghi, O. M. *Chem. Rev.* **2016**, *116* (19), 12466–12535.

(65) Kumar, M.; Wu, L.-H.; Kariem, M.; Franconetti, A.; Sheikh, H. N.; Liu, S.-J.; Sahoo, S. C.; Frontera, A. *Inorg. Chem.* **2019**, *58* (12), 7760–7774.

(66) Wong, N. E.; Ramaswamy, P.; Lee, A. S.; Gelfand, B. S.; Bladek, K. J.; Taylor, J. M.; Spasyuk, D. M.; Shimizu, G. K. H. *J. Am. Chem. Soc.* **2017**, *139* (41), 14676–14683.

(67) Michaelides, A.; Skoulika, S. *Cryst. Growth Des.* **2005**, *5* (2), 529–533.

(68) Devic, T.; Serre, C.; Audebrand, N.; Marrot, J.; Férey, G. *J. Am. Chem. Soc.* **2005**, *127* (37), 12788–12789.

(69) Tobin, G.; Comby, S.; Zhu, N.; Clérac, R.; Gunnlaugsson, T.; Schmitt, W. *Chem. Commun.* **2015**, *51* (68), 13313–13316.

(70) Ouchi, A.; Suzuki, Y.; Ohki, Y.; Koizumi, Y. *Coord. Chem. Rev.* **1988**, *92*, 29–43.

(71) Zheng, Z. *Chem. Commun.* **2001**, No. 24, 2521–2529.

(72) Wang, R.; Selby, H. D.; Liu, H.; Carducci, M. D.; Jin, T.; Zheng, Z.; Anthis, J. W.; Staples, R. J. *Inorg. Chem.* **2002**, *41* (2), 278–286.

(73) Wang, R.; Liu, H.; Carducci, M. D.; Jin, T.; Zheng, C.; Zheng, Z. *Inorg. Chem.* **2001**, *40* (12), 2743–2750.

(74) Serpaggi, F.; Férey, G. *J. Mater. Chem.* **1998**, *8* (12), 2737–2741.

(75) Kiritsis, V.; Michaelides, A.; Skoulika, S.; Golhen, S.; Ouahab, L. *Inorg. Chem.* **1998**, *37* (13), 3407–3410.

(76) Reineke, T. M.; Eddaoudi, M.; Moler, D.; O'Keeffe, M.; Yaghi, O. M. *J. Am. Chem. Soc.* **2000**, *122* (19), 4843–4844.

(77) He, H.; Yuan, D.; Ma, H.; Sun, D.; Zhang, G.; Zhou, H.-C. *Inorg. Chem.* **2010**, *49* (17), 7605–7607.

(78) Liao, J.-H.; Tsai, C.-S.; Lin, T.-K. *Inorg. Chem. Commun.* **2010**, *13* (2), 286–289.

(79) Nayak, S.; Nayek, H. P.; Pietzonka, C.; Novitchi, G.; Dehnen, S. *J. Mol. Struct* **2011**, *1004* (1), 82–87.

(80) Efthymiou, C. G.; Kyprianidou, E. J.; Milios, C. J.; Manos, M. J.; Tasiopoulos, A. J. *J. Mater. Chem. A* **2013**, *1* (16), 5061–5069.

(81) Mahata, P.; Ramya, K. V.; Natarajan, S. *Chem. Eur. J.* **2008**, *14* (19), 5839–5850.

(82) Li, H.; Eddaoudi, M.; O'Keeffe, M.; Yaghi, O. M. *Nature* **1999**, *402* (6759), 276–279.

(83) Roques, N.; Maspoch, D.; Imaz, I.; Datcu, A.; Sutter, J.-P.; Rovira, C.; Veciana, J. *Chem. Commun.* **2008**, No. 27, 3160–3162.

(84) Bhattacharjee, S.; Chen, C.; Ahn, W.-S. *RSC Adv.* **2014**, *4* (94), 52500–52525.

(85) Férey, G.; Serre, C.; Mellot-Draznieks, C.; Millange, F.; Surblé, S.; Dutour, J.; Margiolaki, I. *Angew. Chem. Int. Ed.* **2004**, *43* (46), 6296–6301.

(86) Dezotti, Y.; Ribeiro, M. A.; Pirota, K. R.; Barros, W. P. *Cryst. Growth Des.* **2019**, *19* (10), 5592–5603.

(87) Karmakar, A.; Hazra, S.; Guedes da Silva, M. F. C.; Paul, A.; Pombeiro, A. J. L. *CrystEngComm* **2016**, *18* (8), 1337–1349.

(88) Zhang, L.; Song, T.; Xu, J.; Sun, J.; Zeng, S.; Wu, Y.; Fan, Y.; Wang, L. *CrystEngComm* **2014**, *16* (12), 2440–2451.

(89) Sudik, A. C.; Côté, A. P.; Yaghi, O. M. *Inorg. Chem.* **2005**, *44* (9), 2998–3000.

(90) Serre, C.; Mellot-Draznieks, C.; Surblé, S.; Audebrand, N.; Filinchuk, Y.; Férey, G. *Science* **2007**, *315* (5820), 1828–1831.

(91) Ma, B.-Q.; Zhang, D.-S.; Gao, S.; Jin, T.-Z.; Yan, C.-H.; Xu, G.-X. *Angew. Chem. Int. Ed.* **2000**, *39* (20), 3644–3646.

(92) Wu, P.; He, C.; Wang, J.; Peng, X.; Li, X.; An, Y.; Duan, C. *J. Am. Chem. Soc.* **2012**, *134* (36), 14991–14999.

(93) Han, L.; Zhang, S.; Wang, Y.; Yan, X.; Lu, X. *Inorg. Chem.* **2009**, *48* (3), 786–788.

(94) Yi, X.; Bernot, K.; Calvez, G.; Daiguebonne, C.; Guillou, O. *Eur. J. Inorg. Chem.* **2013**, No. 34, 5879–5885.

(95) Savard, D.; Lin, P.-H.; Burchell, T. J.; Korobkov, I.; Wernsdorfer, W.; Clérac, R.; Murugesu, M. *Inorg. Chem.* **2009**, *48* (24), 11748–11754.

(96) Silva, P.; Cunha-Silva, L.; Silva, N. J. O.; Rocha, J.; Paz, F. A. A. *Cryst. Growth Des.* **2013**, *13* (6), 2607–2617.

(97) Luo, T.-Y.; Liu, C.; Eliseeva, S. V.; Muldoon, P. F.; Petoud, S.; Rosi, N. L. *J. Am. Chem. Soc.* **2017**, *139* (27), 9333–9340.

(98) Chen, L.-F.; Zhang, J.; Ren, G.-Q.; Li, Z.-J.; Qin, Y.-Y.; Yin, P.-X.; Cheng, J.-K.; Yao, Y.-G. *CrystEngComm* **2008**, *10* (8), 1088–1092.

(99) Shi, F.-N.; Cunha-Silva, L.; Trindade, T.; Paz, F. A. A.; Rocha, J. *Cryst. Growth Des.* **2009**, *9* (5), 2098–2109.

(100) Gándara, F.; Gutiérrez-Puebla, E.; Iglesias, M.; Snejko, N.; Monge, M. Á. *Cryst. Growth Des.* **2010**, *10* (1), 128–134.

(101) Demel, J.; Kubát, P.; Millange, F.; Marrot, J.; Císařová, I.; Lang, K. *Inorg. Chem.* **2013**, *52* (5), 2779–2786.

(102) Cavka, J. H.; Jakobsen, S.; Olsbye, U.; Guillou, N.; Lamberti, C.; Bordiga, S.; Lillerud, K. P. *J. Am. Chem. Soc.* **2008**, *130* (42), 13850–13851.

(103) Yassine, O.; Shekhah, O.; Assen, A. H.; Belmabkhout, Y.; Salama, K. N.; Eddaoudi, M. *Angew. Chem. Int. Ed.* **2016**, *55* (51), 15879–15883.

(104) Assen, A. H.; Belmabkhout, Y.; Adil, K.; Bhatt, P. M.; Xue, D.-X.; Jiang, H.; Eddaoudi, M. *Angew. Chem. Int. Ed.* **2015**, *54* (48), 14353–14358.

(105) Luebke, R.; Belmabkhout, Y.; Weseliński, Ł. J.; Cairns, A. J.; Alkordi, M.; Norton, G.; Wojtas, Ł.; Adil, K.; Eddaoudi, M. *Chem. Sci.* **2015**, *6* (7), 4095–4102.

(106) Guo, Y.; Zhang, L.; Muhammad, N.; Xu, Y.; Zhou, Y.; Tang, F.; Yang, S. *Inorg. Chem.* **2018**, *57* (3), 995–1003.

(107) Fang, W.-H.; Cheng, L.; Huang, L.; Yang, G.-Y. *Inorg. Chem.* **2013**, *52* (1), 6–8.

(108) Guillerm, V.; Weseliński, Ł. J.; Belmabkhout, Y.; Cairns, A. J.; D'Elia, V.; Wojtas, Ł.; Adil, K.; Eddaoudi, M. *Nat. Chem.* **2014**, *6* (8), 673–680.

(109) AbdulHalim, R. G.; Bhatt, P. M.; Belmabkhout, Y.; Shkurenko, A.; Adil, K.; Barbour, L. J.; Eddaoudi, M. *J. Am. Chem. Soc.* **2017**, *139* (31), 10715–10722.

(110) Feng, L.; Wang, Y.; Zhang, K.; Wang, K.-Y.; Fan, W.; Wang, X.; Powell, J. A.; Guo, B.; Dai, F.; Zhang, L.; Wang, R.; Sun, D.; Zhou, H.-C. *Angew. Chem. Int. Ed.* **2019**, *58* (46), 16682–16690.

(111) Zhang, Y.; Huang, L.; Miao, H.; Wan, H. X.; Mei, H.; Liu, Y.; Xu, Y. *Chem. Eur. J.* **2015**, *21* (8), 3234–3241.

(112) Hu, F.; Di, Z.; Wu, M.; Hong, M.; Li, J. *Cryst. Growth Des.* **2019**, *19* (11), 6381–6387.

(113) Stock, N.; Biswas, S. *Chem. Rev.* **2012**, *112* (2), 933–969.

(114) Meek, S. T.; Greathouse, J. A.; Allendorf, M. D. *Adv. Mater.* **2011**, *23* (2), 249–267.

(115) Gangu, K. K.; Maddila, S.; Jonnalagadda, S. B. *Inorganica Chim. Acta* **2017**, *466*, 308–323.

(116) Qi, Y.; Luo, F.; Che, Y.; Zheng, J. *Cryst. Growth Des.* **2008**, *8* (2), 606–611.

(117) Liang, Y.; Yuan, W.-G.; Zhang, S.-F.; He, Z.; Xue, J.; Zhang, X.; Jing, L.-H.; Qin, D.-B. *Dalton Trans.* **2016**, *45* (4), 1382–1390.

(118) Li, M.; Dincă, M. *J. Am. Chem. Soc.* **2011**, *133* (33), 12926–12929.

(119) Al-Kutubi, H.; Gascon, J.; Sudhölter, E. J. R.; Rassaei, L. *ChemElectroChem* **2015**, *2* (4), 462–474.

(120) Haque, E.; Khan, N. A.; Kim, C. M.; Jhung, S. H. *Cryst. Growth Des.* **2011**, *11* (10), 4413–4421.

(121) Klimakow, M.; Klobes, P.; Thünemann, A. F.; Rademann, K.; Emmerling, F. *Chem. Mater.* **2010**, *22* (18), 5216–5221.

(122) Friščić, T. *Chem. Soc. Rev.* **2012**, *41* (9), 3493–3510.

(123) Friščić, T.; Reid, D. G.; Halasz, I.; Stein, R. S.; Dinnebier, R. E.; Duer, M. J. *Angew. Chem. Int. Ed.* **2010**, *49* (4), 712–715.

(124) Klinowski, J.; Paz, F. A. A.; Silva, P.; Rocha, J. *Dalton Trans.* **2010**, *40* (2), 321–330.

(125) Zacher, D.; Shekhah, O.; Wöll, C.; Fischer, R. A. *Chem. Soc. Rev.* **2009**, *38* (5), 1418–1429.

(126) Howarth, A. J.; Peters, A. W.; Vermeulen, N. A.; Wang, T. C.; Hupp, J. T.; Farha, O. K. *Chem. Mater.* **2017**, *29* (1), 26–39.

(127) Schaate, A.; Roy, P.; Godt, A.; Lippke, J.; Waltz, F.; Wiebcke, M.; Behrens, P. *Chem. Eur. J.* **2011**, *17* (24), 6643–6651.

(128) Vermoortele, F.; Bueken, B.; Le Bars, G.; Van de Voorde, B.; Vandichel, M.; Houthoofd, K.; Vimont, A.; Daturi, M.; Waroquier, M.; Van Speybroeck, V.; Kirschhock, C.; De Vos, D. E. *J. Am. Chem. Soc.* **2013**, *135* (31), 11465–11468.

(129) Mondloch, J. E.; Karagiaridi, O.; Farha, O. K.; Hupp, J. T. *CrystEngComm* **2013**, *15* (45), 9258.

(130) Nelson, A. P.; Farha, O. K.; Mulfort, K. L.; Hupp, J. T. *J. Am. Chem. Soc.* **2009**, *131* (2), 458–460.

(131) Eckert, C. A.; Knutson, B. L.; Debenedetti, P. G. *Nature* **1996**, *383* (6598), 313–318.

(132) Mukhopadhyay, M. *J. Chem. Technol. Biotechnol.* **2009**, *84* (1), 6–12.

(133) Harris, K. D. M.; Tremayne, M.; Kariuki, B. M. *Angew. Chem. Int. Ed.* **2001**, *40* (9), 1626–1651.

(134) Wilmer, C. E.; Leaf, M.; Lee, C. Y.; Farha, O. K.; Hauser, B. G.; Hupp, J. T.; Snurr, R. Q. *Nat. Chem.* **2012**, *4* (2), 83–89.

(135) Farha, O. K.; Eryazici, I.; Jeong, N. C.; Hauser, B. G.; Wilmer, C. E.; Sarjeant, A. A.; Snurr, R. Q.; Nguyen, S. T.; Yazaydın, A. Ö.; Hupp, J. T. *J. Am. Chem. Soc.* **2012**, *134* (36), 15016–15021.

(136) Thommes, M. *Chem. Ing. Tech.* **2010**, *82* (7), 1059–1073.

(137) Thommes, M.; Kaneko, K.; Neimark, A. V.; Olivier, J. P.; Rodriguez-Reinoso, F.; Rouquerol, J.; Sing, K. S. *Pure Appl. Chem.* **2015**, *87* (9–10), 1051–1069.

(138) Brunauer, S.; Emmett, P. H.; Teller, E. *J. Am. Chem. Soc.* **1938**, *60* (2), 309–319.

(139) Langmuir, I. *J. Am. Chem. Soc.* **1918**, *40* (9), 1361–1403.

(140) Tarazona, P.; Marconi, U. M. B.; Evans, R. *Mol. Phys.* **1987**, *60* (3), 573–595.

(141) Barrett, E. P.; Joyner, L. G.; Halenda, P. P. *J. Am. Chem. Soc.* **1951**, *73* (1), 373–380.

(142) Coats, A. W.; Redfern, J. P. *Analyst* **1963**, *88* (1053), 906–924.

(143) Gill, P.; Moghadam, T. T.; Ranjbar, B. *J Biomol Tech* **2010**, *21* (4), 167–193.

(144) Shaffner, T. J.; Veld, R. D. V. *J. Phys. E: Sci. Instrum.* **1971**, *4* (9), 633–637.

(145) Wang, T. C.; Vermeulen, N. A.; Kim, I. S.; Martinson, A. B. F.; Stoddart, J. F.; Hupp, J. T.; Farha, O. K. *Nat Protoc* **2016**, *11* (1), 149–162.

(146) Sutrisno, A.; Huang, Y. *Solid State Nucl. Magn. Reson.* **2013**, *49–50*, 1–11.

(147) Hoffmann, H. C.; Debowski, M.; Müller, P.; Paasch, S.; Senkovska, I.; Kaskel, S.; Brunner, E. *Materials (1996-1944)* **2012**, *5* (12), 2537–2572.

(148) Mali, G. *Metal-Organic Frameworks* **2016**.

(149) Marchetti, A.; Chen, J.; Pang, Z.; Li, S.; Ling, D.; Deng, F.; Kong, X. *Adv. Mater.* **2017**, *29* (14), 1605895.

(150) Howarth, A. J.; Peters, A. W.; Vermeulen, N. A.; Wang, T. C.; Hupp, J. T.; Farha, O. K. *Chem. Mater.* **2017**, *29* (1), 26–39.

(151) Armaroli, T.; Bécue, T.; Gautier, S. *Oil Gas Sci. Technol.* **2004**, *59* (2), 215–237.

(152) Woody, R.W. *Meth. Enzymol.* **1995**, *246*, 34–71.

(153) Castiglioni, E.; Biscarini, P.; Abbate, S. *Chirality* **2009**, *21* (1E), E28–E36.

(154) Bettencourt-Dias, A. de; Viswanathan, S. *Dalton Trans.* **2006**, No. 34, 4093–4103.

(155) Liu, W.; Jiao, T.; Li, Y.; Liu, Q.; Tan, M.; Wang, H.; Wang, L. *J. Am. Chem. Soc.* **2004**, *126* (8), 2280–2281.

(156) Bünzli, J.-C. G. *Eur. J. Inorg. Chem.* **2017**, *2017* (44), 5058–5063.

(157) Bünzli, J.-C. G. *Trends Chem* **2019**, *1* (8), 751–762.

(158) Roy, S.; Chakraborty, A.; Maji, T. K. *Coord. Chem. Rev.* **2014**, *273–274*, 139–164.

(159) Li, B.; Chen, B. In *Lanthanide Metal-Organic Frameworks*; Cheng, P., Ed.; Springer: Berlin, Heidelberg, 2015; pp 75–107.

(160) Makhmudiyarova, N. N.; Ishmukhametova, I. R.; Tyumkina, T. V.; Ibragimov, A. G.; Dzhemilev, U. M. *Tetrahedron Lett.* **2018**, *59* (33), 3161–3164.

(161) Barger, C. J.; Motta, A.; Weidner, V. L.; Lohr, T. L.; Marks, T. J. *ACS Catal.* **2019**, *9* (10), 9015–9024.

(162) Rieter, W. J.; Pott, K. M.; Taylor, K. M. L.; Lin, W. *J. Am. Chem. Soc.* **2008**, *130* (35), 11584–11585.

(163) Huxford-Phillips, R. C.; Russell, S. R.; Liu, D.; Lin, W. *RSC Adv.* **2013**, *3* (34), 14438–14443.

(164) Escudero, A.; Becerro, A. I.; Carrillo-Carrión, C.; Núñez, N. O.; Zyuzin, M. V.; Laguna, M.; González-Mancebo, D.; Ocaña, M.; Parak, W. J. *J. Nanophotonics* **2017**, *6* (5), 881–921.

(165) Pili, S.; Rought, P.; Kolokolov, D. I.; Lin, L.; da Silva, I.; Cheng, Y.; Marsh, C.; Silverwood, I. P.; García Sakai, V.; Li, M.; Titman, J. J.; Knight, L.; Daemen, L. L.; Ramirez-Cuesta, A. J.; Tang, C. C.; Stepanov, A. G.; Yang, S.; Schröder, M. *Chem. Mater.* **2018**, *30* (21), 7593–7602.

(166) Kalinke, L. H. G.; Cangussu, D.; Mon, M.; Bruno, R.; Tiburcio, E.; Lloret, F.; Armentano, D.; Pardo, E.; Ferrando-Soria, J. *Inorg. Chem.* **2019**, *58* (21), 14498–14506.

(167) de Bettencourt-Dias, A. *Inorg. Chem.* **2005**, *44* (8), 2734–2741.

(168) Reineke, T. M.; Eddaoudi, M.; Fehr, M.; Kelley, D.; Yaghi, O. M. *J. Am. Chem. Soc.* **1999**, *121* (8), 1651–1657.

(169) Serre, C.; Millange, F.; Thouvenot, C.; Gardant, N.; Pellé, F.; Férey, G. *J. Mater. Chem.* **2004**, *14* (10), 1540–1543.

(170) Chandler, B. D.; Cramb, D. T.; Shimizu, G. K. H. *J. Am. Chem. Soc.* **2006**, *128* (32), 10403–10412.

(171) Wu, J.-Y.; Yeh, T.-T.; Wen, Y.-S.; Twu, J.; Lu, K.-L. *Cryst. Growth Des.* **2006**, *6* (2), 467–473.

(172) de Lill, D. T.; de Bettencourt-Dias, A.; Cahill, C. L. *Inorg. Chem.* **2007**, *46* (10), 3960–3965.

(173) Horrocks, W. DeW.; Sudnick, D. R. *J. Am. Chem. Soc.* **1979**, *101* (2), 334–340.

(174) Li, Y.; Zhang, S.; Song, D. *Angew. Chem. Int. Ed.* **2013**, *52* (2), 710–713.

(175) Xiao, Y.; Wang, L.; Cui, Y.; Chen, B.; Zapata, F.; Qian, G. *J. Alloys Compd* **2009**, *484* (1), 601–604.

(176) Chen, B.; Yang, Y.; Zapata, F.; Lin, G.; Qian, G.; Lobkovsky, E. B. *Adv. Mater.* **2007**, *19* (13), 1693–1696.

(177) Zhou, Y.-Y.; Shi, Y.; Geng, B.; Bo, Q.-B. *ACS Appl. Mater. Interfaces* **2017**, *9* (6), 5337–5347.

(178) Ebrahim, F. M.; Nguyen, T. N.; Shyshkanov, S.; Gładysiak, A.; Favre, P.; Zacharia, A.; Itskos, G.; Dyson, P. J.; Stylianou, K. C. *J. Am. Chem. Soc.* **2019**, *141* (7), 3052–3058.

(179) Chen, B.; Wang, L.; Zapata, F.; Qian, G.; Lobkovsky, E. B. *J. Am. Chem. Soc.* **2008**, *130* (21), 6718–6719.

(180) Zhang, S.-Y.; Shi, W.; Cheng, P.; Zaworotko, M. J. *J. Am. Chem. Soc.* **2015**, *137* (38), 12203–12206.

(181) Cui, Y.; Xu, H.; Yue, Y.; Guo, Z.; Yu, J.; Chen, Z.; Gao, J.; Yang, Y.; Qian, G.; Chen, B. *J. Am. Chem. Soc.* **2012**, *134* (9), 3979–3982.

(182) Li, Y.-J.; Wang, Y.-L.; Liu, Q.-Y. *Inorg. Chem.* **2017**, *56* (4), 2159–2164.

(183) Liu, Z.; Zhang, L.; Sun, D. *Chem. Commun.* **2020**, *56* (66), 9416–9432.

(184) Yaghi, O. M.; O'Keeffe, M.; Ockwig, N. W.; Chae, H. K.; Eddaoudi, M.; Kim, J. *Nature* **2003**, *423* (6941), 705–714.

(185) Yaghi, O.M. *J. Am. Chem. Soc.* **2016**, *138* (48), 15507–15509.

(186) Cheetham, A. K.; Férey, G.; Loiseau, T. *Angew. Chem. Int. Ed.* **1999**, *38* (22), 3268–3292.

(187) Titi, H. M.; Marrett, J. M.; Dayaker, G.; Arhangelskis, M.; Mottillo, C.; Morris, A. J.; Rachiero, G. P.; Friščić, T.; Rogers, R. D. *Sci. Adv.* **2019**, *5* (4), eaav9044.

(188) Ma, S.; Zhou, H.-C. *Chem. Commun.* **2010**, *46* (1), 44–53.

(189) Herm, Z. R.; Bloch, E. D.; Long, J. R. *Chem. Mater.* **2014**, *26* (1), 323–338.

(190) Horcajada, P.; Gref, R.; Baati, T.; Allan, P. K.; Maurin, G.; Couvreur, P.; Férey, G.; Morris, R. E.; Serre, C. *Chem. Rev.* **2012**, *112* (2), 1232–1268.

(191) Horcajada, P.; Serre, C.; Vallet-Regí, M.; Sebban, M.; Taulelle, F.; Férey, G. *Angew. Chem. Int. Ed.* **2006**, *118* (36), 6120–6124.

(192) Liu, Y.; Howarth, A. J.; Vermeulen, N. A.; Moon, S.-Y.; Hupp, J. T.; Farha, O. K. *Coord. Chem. Rev.* **2017**, *346*, 101–111.

(193) Majewski, M. B.; Peters, A. W.; Wasielewski, M. R.; Hupp, J. T.; Farha, O. K. *ACS Energy Lett.* **2018**, *3* (3), 598–611.

(194) Howarth, A. J.; Liu, Y.; Hupp, J. T.; Farha, O. K. *CrystEngComm* **2015**, *17* (38), 7245–7253.

(195) Kim, H.; Yang, S.; Rao, S. R.; Narayanan, S.; Kapustin, E. A.; Furukawa, H.; Umans, A. S.; Yaghi, O. M.; Wang, E. N. *Science* **2017**, *356* (6336), 430–434.

(196) Li, H.; Eddaoudi, M.; O'Keeffe, M.; Yaghi, O. M. *Nature* **1999**, *402* (6759), 276–279.

(197) Xuan, W.; Zhu, C.; Liu, Y.; Cui, Y. *Chem. Soc. Rev.* **2012**, *41* (5), 1677–1695.

(198) Rosi, N. L.; Kim, J.; Eddaoudi, M.; Chen, B.; O'Keeffe, M.; Yaghi, O. M. *J. Am. Chem. Soc.* **2005**, *127* (5), 1504–1518.

(199) Joseph, N.; Lawson, H. D.; Overholt, K. J.; Damodaran, K.; Gottardi, R.; Acharya, A. P.; Little, S. R. *Sci. Rep.* **2019**, *9* (1), 1–11.

(200) Otake, K.; Cui, Y.; Buru, C. T.; Li, Z.; Hupp, J. T.; Farha, O. K. *J. Am. Chem. Soc.* **2018**, *140* (28), 8652–8656.

(201) Feng, D.; Wang, K.; Wei, Z.; Chen, Y.-P.; Simon, C. M.; Arvapally, R. K.; Martin, R. L.; Bosch, M.; Liu, T.-F.; Fordham, S.; Yuan, D.; Omary, M. A.; Haranczyk, M.; Smit, B.; Zhou, H.-C. *Nat. Commun* **2014**, *5* (1), 1–9.

(202) Phan, A.; Doonan, C. J.; Uribe-Romo, F. J.; Knobler, C. B.; O'Keeffe, M.; Yaghi, O. M. *Acc. Chem. Res.* **2010**, *43* (1), 58–67.

(203) Xue, D.-X.; Cairns, A. J.; Belmabkhout, Y.; Wojtas, L.; Liu, Y.; Alkordi, M. H.; Eddaoudi, M. *J. Am. Chem. Soc.* **2013**, *135* (20), 7660–7667.

(204) Hanna, S. L.; Zhang, X.; Otake, K.; Drout, R. J.; Li, P.; Islamoglu, T.; Farha, O. K. *Cryst. Growth Des.* **2019**, *19* (1), 506–512.

(205) Jiang, H.; Jia, J.; Shkurenko, A.; Chen, Z.; Adil, K.; Belmabkhout, Y.; Weselinski, L. J.; Assen, A. H.; Xue, D.-X.; O'Keeffe, M.; Eddaoudi, M. *J. Am. Chem. Soc.* **2018**, *140* (28), 8858–8867.

(206) Chen, Z.; Weseliński, Ł. J.; Adil, K.; Belmabkhout, Y.; Shkurenko, A.; Jiang, H.; Bhatt, P. M.; Guillerm, V.; Dauzon, E.; Xue, D.-X.; O'Keeffe, M.; Eddaoudi, M. *J. Am. Chem. Soc.* **2017**, *139* (8), 3265–3274.

(207) AbdulHalim, R. G.; Bhatt, P. M.; Belmabkhout, Y.; Shkurenko, A.; Adil, K.; Barbour, L. J.; Eddaoudi, M. *J. Am. Chem. Soc.* **2017**, *139* (31), 10715–10722.

(208) Yang, Q.-Y.; Li, K.; Luo, J.; Pan, M.; Su, C.-Y. *Chem. Commun.* **2011**, *47* (14), 4234–4236.

(209) Zhang, L.; Yuan, S.; Feng, L.; Guo, B.; Qin, J.-S.; Xu, B.; Lollar, C.; Sun, D.; Zhou, H.-C. *Angew. Chem. Int. Ed.* **2018**, *57* (18), 5095–5099.

(210) Wang, Y.; Feng, L.; Fan, W.; Wang, K.-Y.; Wang, X.; Wang, X.; Zhang, K.; Zhang, X.; Dai, F.; Sun, D.; Zhou, H.-C. *J. Am. Chem. Soc.* **2019**, *141* (17), 6967–6975.

(211) Zhang, Y.; Zhang, X.; Lyu, J.; Otake, K.; Wang, X.; Redfern, L. R.; Malliakas, C. D.; Li, Z.; Islamoglu, T.; Wang, B.; Farha, O. K. *J. Am. Chem. Soc.* **2018**, *140* (36), 11179–11183.

(212) Furukawa, H.; Gándara, F.; Zhang, Y.-B.; Jiang, J.; Queen, W. L.; Hudson, M. R.; Yaghi, O. M. *J. Am. Chem. Soc.* **2014**, *136* (11), 4369–4381.

(213) Feng, D.; Wang, K.; Su, J.; Liu, T.-F.; Park, J.; Wei, Z.; Bosch, M.; Yakovenko, A.; Zou, X.; Zhou, H.-C. *Angew. Chem. Int. Ed.* **2015**, *54* (1), 149–154.

(214) Reinsch, H.; Stassen, I.; Bueken, B.; Lieb, A.; Ameloot, R.; De Vos, D. *CrystEngComm* **2015**, *17* (2), 331–337.

(215) Mondloch, J. E.; Bury, W.; Fairen-Jimenez, D.; Kwon, S.; DeMarco, E. J.; Weston, M. H.; Sarjeant, A. A.; Nguyen, S. T.; Stair, P. C.; Snurr, R. Q.; Farha, O. K.; Hupp, J. T. *J. Am. Chem. Soc.* **2013**, *135* (28), 10294–10297.

(216) Bon, V.; Senkovskyy, V.; Senkovska, I.; Kaskel, S. *Chem. Commun.* **2012**, *48* (67), 8407.

(217) Yuan, S.; Lu, W.; Chen, Y.-P.; Zhang, Q.; Liu, T.-F.; Feng, D.; Wang, X.; Qin, J.; Zhou, H.-C. *J. Am. Chem. Soc.* **2015**, *137* (9), 3177–3180.

(218) Jiang, J.; Gándara, F.; Zhang, Y.-B.; Na, K.; Yaghi, O. M.; Klemperer, W. G. *J. Am. Chem. Soc.* **2014**, *136* (37), 12844–12847.

(219) Ptak, M.; Zarychta, B.; Stefańska, D.; Ciupa, A.; Paraguassu, W. *Dalton Trans.* **2019**, *48* (1), 242–252.

(220) Lyu, J.; Gong, X.; Lee, S.-J.; Gnanasekaran, K.; Zhang, X.; Wasson, M. C.; Wang, X.; Bai, P.; Guo, X.; Gianneschi, N. C.; Farha, O. K. *J. Am. Chem. Soc.* **2020**, *142* (10), 4609–4615.

(221) Zhang, J.-P.; Zhou, H.-L.; Zhou, D.-D.; Liao, P.-Q.; Chen, X.-M. *Natl Sci Rev* **2018**, *5* (6), 907–919.

(222) Sakata, Y.; Furukawa, S.; Kondo, M.; Hirai, K.; Horike, N.; Takashima, Y.; Uehara, H.; Louvain, N.; Meilikhov, M.; Tsuruoka, T.; Isoda, S.; Kosaka, W.; Sakata, O.; Kitagawa, S. *Science* **2013**, *339* (6116), 193–196.

(223) Mason, J. A.; Oktawiec, J.; Taylor, M. K.; Hudson, M. R.; Rodriguez, J.; Bachman, J. E.; Gonzalez, M. I.; Cervellino, A.; Guagliardi, A.; Brown, C. M.; Llewellyn, P. L.; Masciocchi, N.; Long, J. R. *Nature* **2015**, *527* (7578), 357–361.

(224) Dai, F.; Wang, X.; Wang, Y.; Liu, Z.; Sun, D. *Angew. Chem. Int. Ed.* **2020**.

(225) Sheldrick, G. M. *Acta Cryst C* **2015**, *71* (1), 3–8.

(226) Sheldrick, G. M. *Acta Cryst A* **2015**, *71* (1), 3–8.

(227) Rietveld, H. M. *J. Appl. Crystallogr.* **1969**, *2* (2), 65–71.

(228) Coelho, A. Coelho Software: Brisbane, Australia 2017.

(229) Clark, S. J.; Segall, M. D.; Pickard, C. J.; Hasnip, P. J.; Probert, M. I. J.; Refson, K.; Payne, M. C. *Z. Kristallogr. Cryst. Mater.* **2005**, *220* (5/6), 567–570.

(230) Perdew, J. P.; Burke, K.; Ernzerhof, M. *Phys. Rev. Lett.* **1996**, *77* (18), 3865–3868.

(231) Grimme, S. *J. Comput. Chem.* **2006**, *27* (15), 1787–1799.

(232) Monkhorst, H. J.; Pack, J. D. *Phys. Rev. B.* **1976**, *13* (12), 5188–5192.

(233) Drout, R. J.; Howarth, A. J.; Otake, K.; Islamoglu, T.; Farha, O. K. *CrystEngComm* **2018**, *20* (40), 6140–6145.

(234) Almáši, M.; Zeleňák, V.; Kuchár, J.; Bourrelly, S.; Llewellyn, P. L. *Colloids Surf. A Physicochem. Eng. Asp.* **2016**, *496*, 114–124.

(235) Zheng, H.-Q.; Liu, C.-Y.; Zeng, X.-Y.; Chen, J.; Lü, J.; Lin, R.-G.; Cao, R.; Lin, Z.-J.; Su, J.-W. *Inorg. Chem.* **2018**, *57* (15), 9096–9104.

(236) Lian, X.; Yan, B. *RSC Adv.* **2016**, *6*, 11570-11576

(237) Li, J.; Yuan, X.; Wu, Y.; Ma, X.; Li, F.; Zhang, B.; Wang, Y.; Lei, Z.; Zhang, Z. *Chem. Eng. J.* **2018**, *350*, 637–644.

(238) Yaghi, O. M.; O'Keeffe, M.; Ockwig, N. W.; Chae, H. K.; Eddaoudi, M.; Kim, J. *Nature* **2003**, *423* (6941), 705–714.

(239) Yaghi, O. M. *J. Am. Chem. Soc.* **2016**, *138* (48), 15507–15509.

(240) Wang, C.; An, B.; Lin, W. *ACS Catal.* **2019**, *9* (1), 130–146.

(241) Jiang, H.; Jia, J.; Shkurenko, A.; Chen, Z.; Adil, K.; Belmabkhout, Y.; Weselinski, L. J.; Assen, A. H.; Xue, D.-X.; O'Keeffe, M.; Eddaoudi, M. *J. Am. Chem. Soc.* **2018**, *140* (28), 8858–8867.

(242) Abednatanzi, S.; Gohari Derakhshandeh, P.; Depauw, H.; Coudert, F.-X.; Vrielinck, H.; Van Der Voort, P.; Leus, K. *Chem. Soc. Rev.* **2019**, *48* (9), 2535–2565.

(243) Cui, Y.; Xu, H.; Yue, Y.; Guo, Z.; Yu, J.; Chen, Z.; Gao, J.; Yang, Y.; Qian, G.; Chen, B. *J. Am. Chem. Soc.* **2012**, *134* (9), 3979–3982.

(244) de Lill, D. T.; Gunning, N. S.; Cahill, C. L. *Inorg. Chem.* **2005**, *44* (2), 258–266.

(245) Zhang, Z.; Zaworotko, M. J. *Chem. Soc. Rev.* **2014**, *43* (16), 5444–5455.

(246) Yang, X.; Liang, T.; Sun, J.; Zaworotko, M. J.; Chen, Y.; Cheng, P.; Zhang, Z. *ACS Catal.* **2019**, *9* (8), 7486–7493.

(247) Richardson, F. S. *Chem. Rev.* **1982**, *82* (5), 541–552.

(248) Guo, Z.; Song, X.; Lei, H.; Wang, H.; Su, S.; Xu, H.; Qian, G.; Zhang, H.; Chen, B. *Chem. Commun.* **2015**, *51* (2), 376–379.

(249) Wang, X.; Li, J.-L.; Jiang, C.; Hu, P.; Li, B.; Zhang, T.; Zhou, H.C. *Chem. Commun.* **2018**, *54*, 13271-13274

(250) Yin, H.-Q.; Yin, X.-B. *Acc. Chem. Res.* **2020**, *53* (2), 485–495.

Appendix 2

Single Crystal X-Ray Diffraction (scXRD) Analysis

Table A.1. Crystal data and structure refinement for Y-MOF-76

Empirical formula	$C_9H_3O_7Y$
Formula weight	312.02
Temperature/K	298(2)
Crystal system	tetragonal
Space group	$P4_322$
a/Å	10.2435(3)
b/Å	10.2435(3)
c/Å	14.4778(4)
α/°	90
β/°	90
γ/°	90
Volume/Å^3	1519.15(10)
Z	4
ρ_{calc}g/cm^3	1.364
μ/mm^{-1}	5.592
F(000)	608.0
Radiation	Cu$K\alpha$ (λ = 1.54178)
2θ range for data collection/°	10.58 to 145.082
Index ranges	$-12 \le h \le 12$, $-12 \le k \le 12$, $-17 \le l \le 17$
Reflections collected	22798
Independent reflections	1509 [R_{int} = 0.1075, R_{sigma} = 0.0347]
Data/restraints/parameters	1509/63/73
Goodness-of-fit on F^2	1.128
Final R indexes [I>=2σ (I)]	R_1 = 0.0418, wR_2 = 0.0967
Final R indexes [all data]	R_1 = 0.0562, wR_2 = 0.1086
Largest diff. peak/hole / e Å^{-3}	1.20/-0.71
Flack parameter	0.22(6)

Rietveld Refinement Analysis of CU-45

Table A.2. Crystallographic parameters of the CU-45 structure determined by Rietveld refinement.

	CU-45
Empirical Formula	$Y_3(OH)_4(BTC)(HCOO)_2$
Molecular Weight	622.89
Crystal system	cubic
a / Å	36.431(2)
b / Å	36.431(2)
c / Å	36.431(2)
α (°)	90
β (°)	90
γ (°)	90
Volume / Å^3	48351(7)
Space group	$Fd\bar{3}m$
ρ_c (g cm^{-3})	0.738(9)
Radiation type	Cu$K\alpha$ (λ = 1.54178)
R_{wp}	0.095
R_p	0.067
R_{Bragg}	0.033
χ^2	3.46

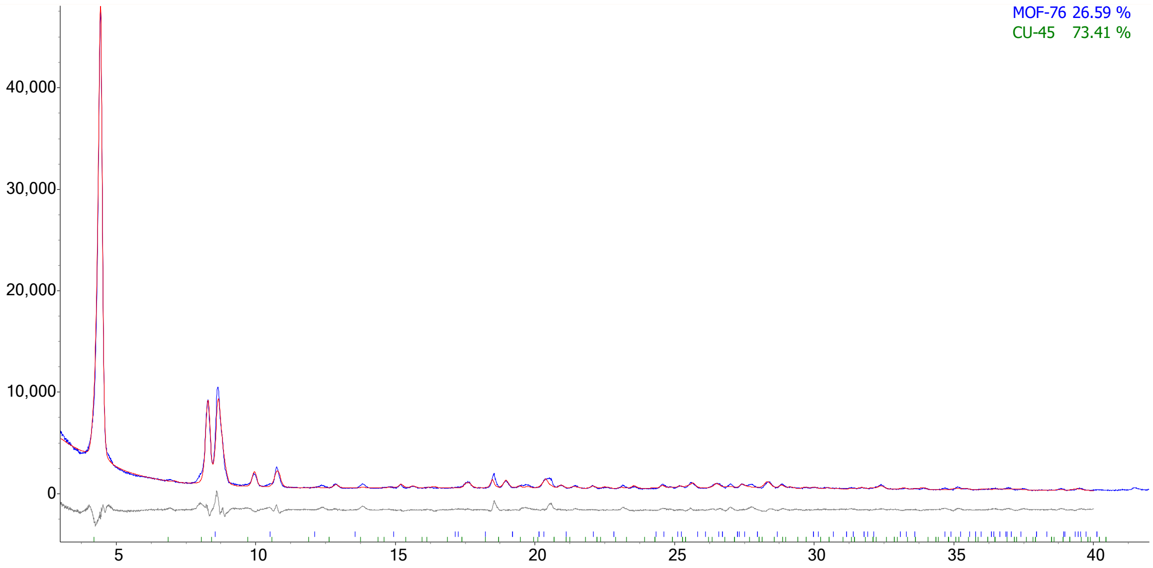

Figure A2.1. Rietveld refinement of CU-45. The calculated and experimental diffraction profiles are shown in red and blue, respectively. The difference curve is shown in grey.

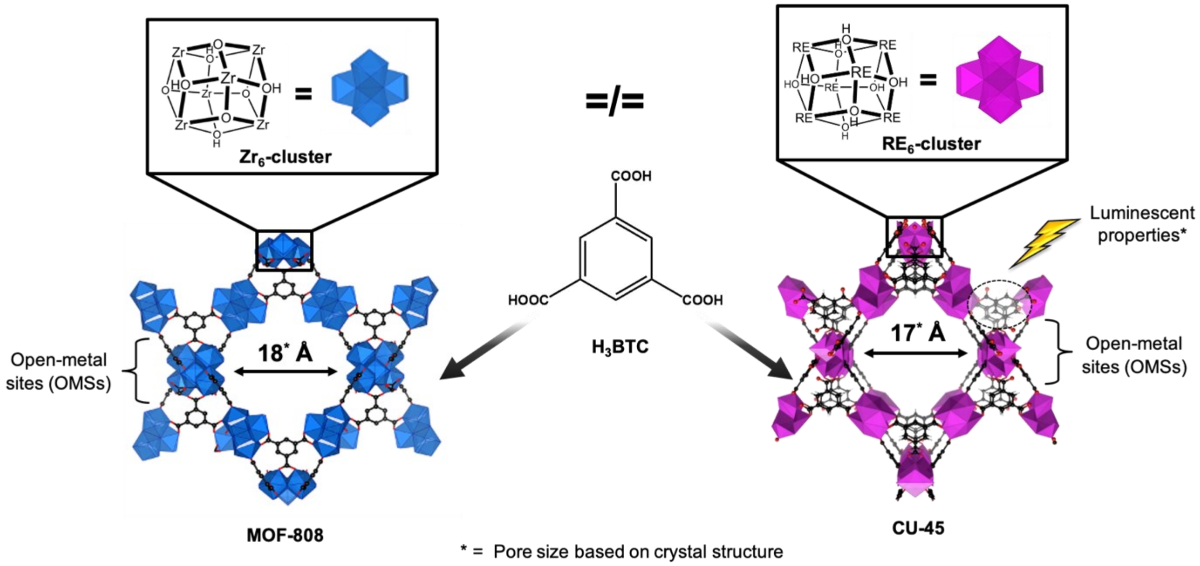

Figure A2.2. Isostructural MOFs, Zr_6-based MOF-808 and Y_6-based CU-45.

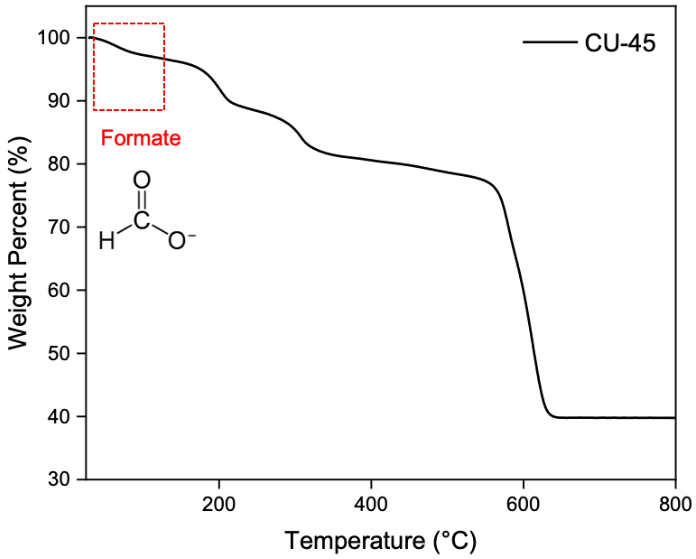

Figure A2.3. TGA curve of CU-45 measured from 25 to 800 °C under air.

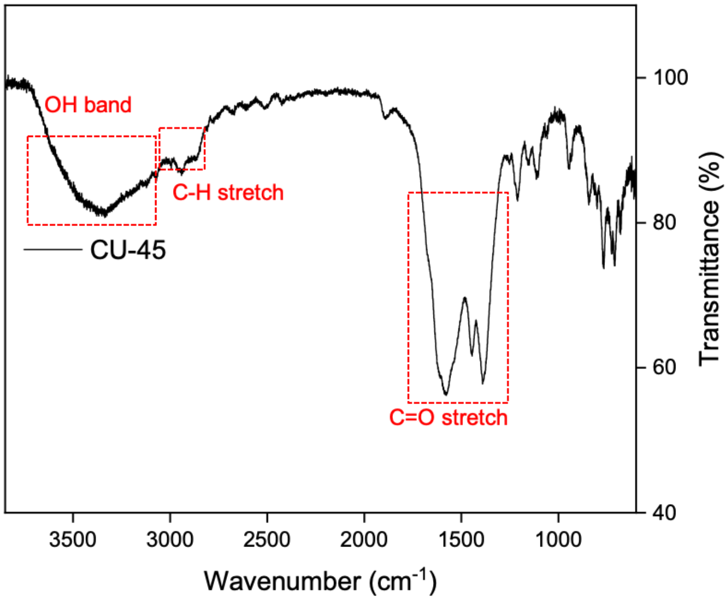

Figure A2.4. DRIFTS spectrum of CU-45 performed with KBr background.

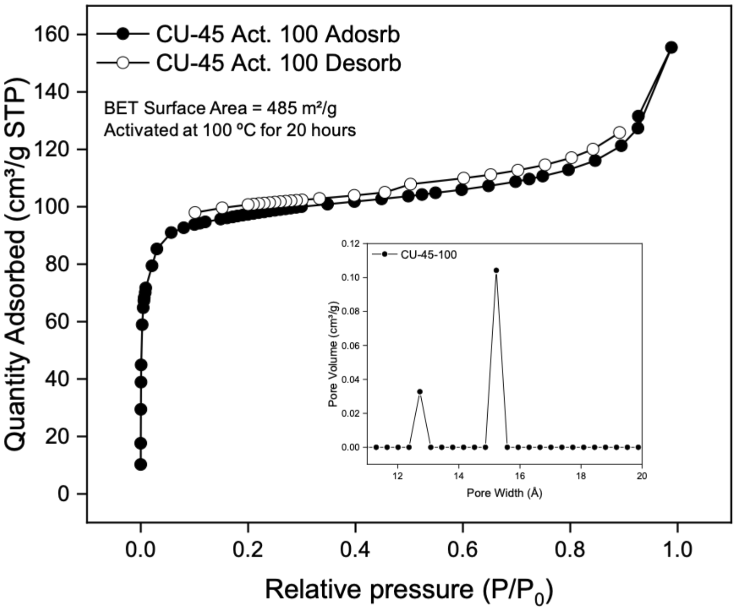

Figure A2.5. N_2 sorption isotherm and PSD analysis of CU-45.

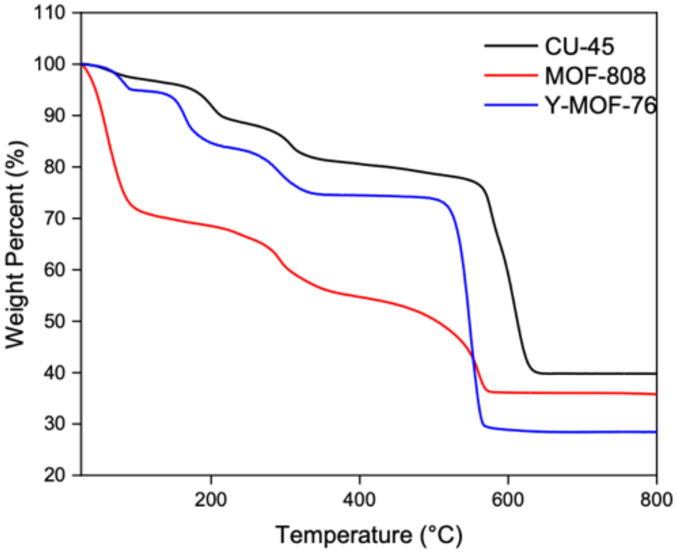

Figure A2.6. TGA curves of CU-45 (black), MOF-808 (red), and Y-MOF-76 (blue) measured from 25 to 800 °C under air.

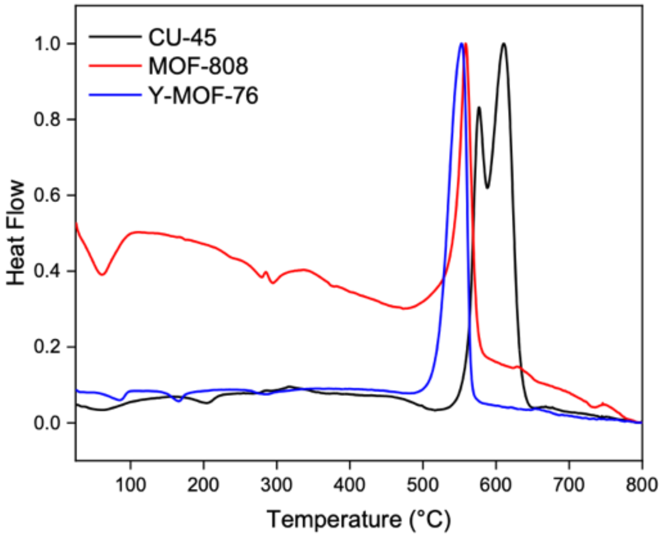

Figure A2.7. DSC curves of CU-45 (black), MOF-808 (red), and Y-MOF-76 (blue) measured from 25 to 800 °C under air.

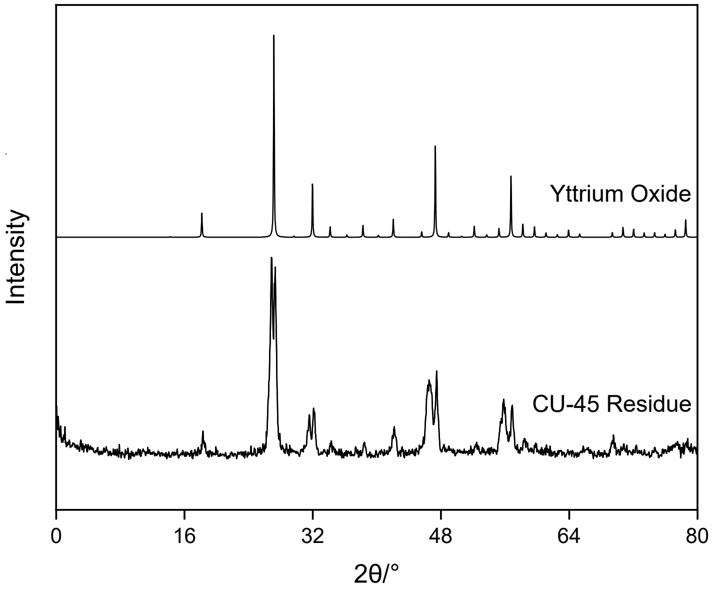

Figure A2.8. PXRD pattern of CU-45 residue and yttrium oxide.

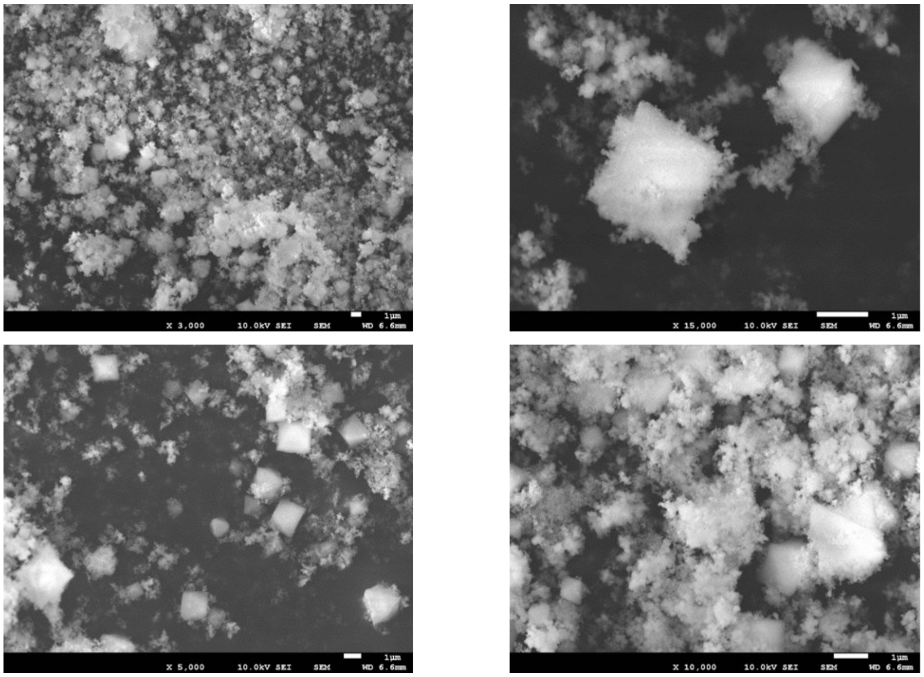

Figure A2.9. SEM images of CU-45 synthesized *de novo*.

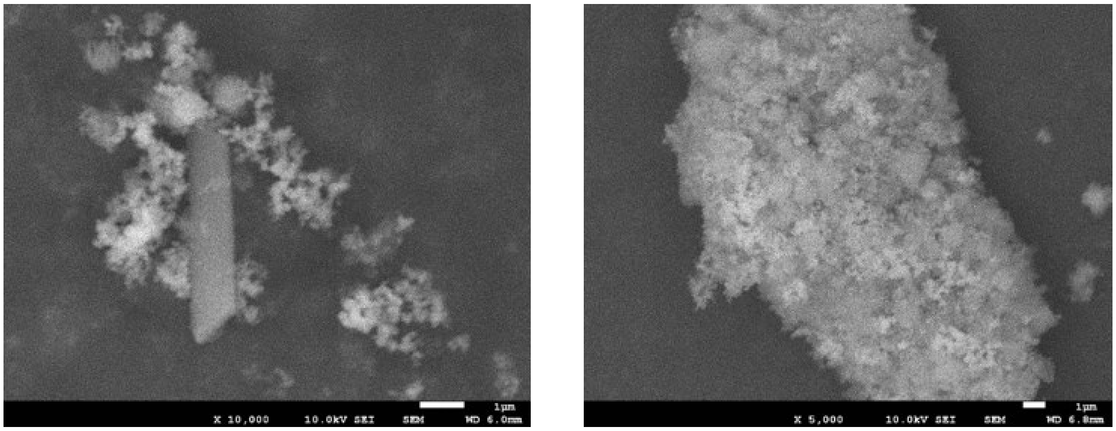

Figure A2.10. SEM images of CU-45 after soaking in water for 24 hours.

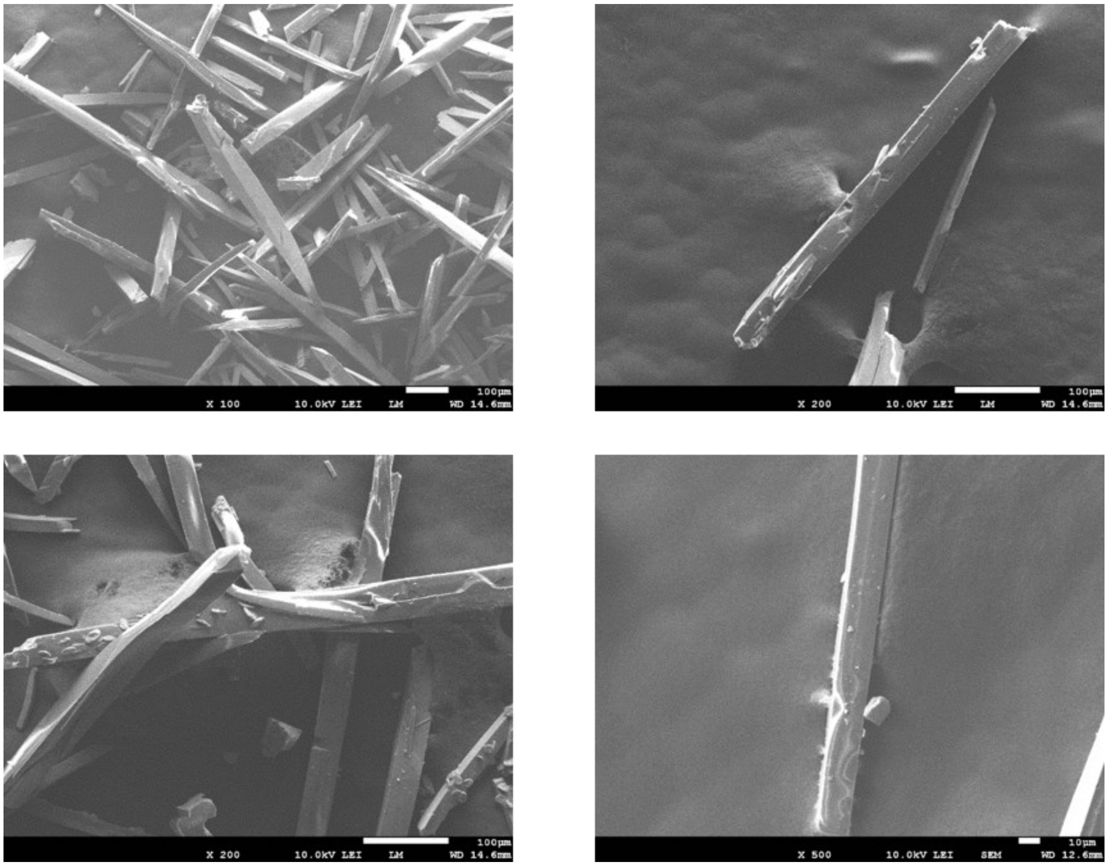

Figure A2.11. SEM images of Y-MOF-76 synthesized *de novo*.

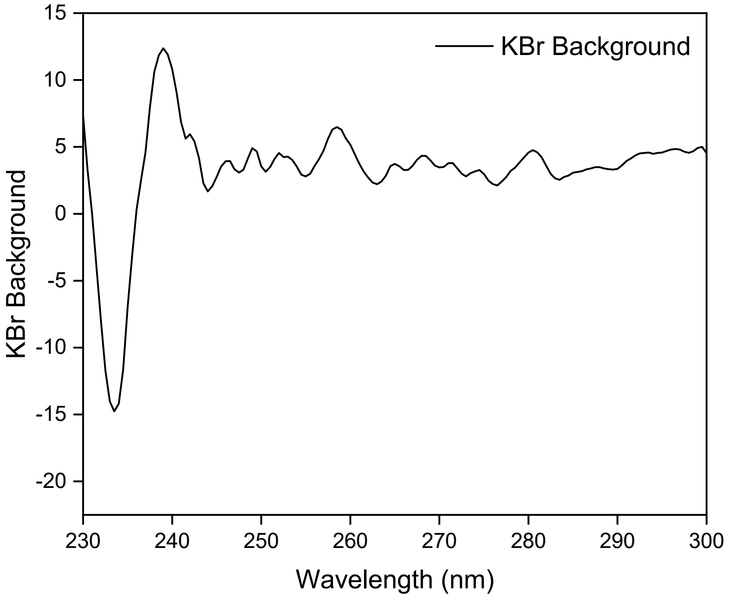

Figure A2.12. solid-state CD spectrum of KBr background.

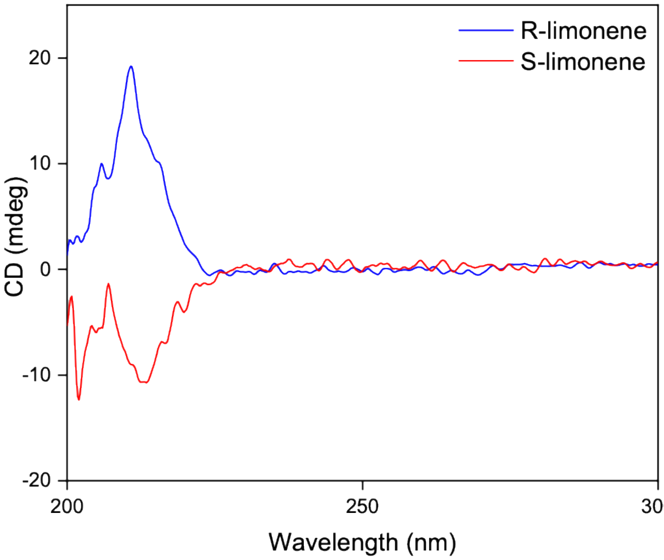

Figure A2.13. CD spectrum of R- and S-limonene performed in hexanes.

The calculated electronic energies of crystalline and gas-phase reagents were used to compute enthalpies for several possible transformations of CU-45 into MOF-76:

$Y_6(OH)_8(BTC)_2(HCOO)_4 + 4\ BTC \rightarrow 6\ Y(BTC)(H_2O) + 4\ HCOOH + 2H_2O$

$\Delta H = 113.94\ kJ\ mol^{-1}$

$Y_6(OH)_8(BTC)_2(HCOO)_4 \rightarrow 2\ Y(BTC)(H_2O) + 2Y_2O_3 + 4\ HCOOH$

$\Delta H = 49.61\ kJ\ mol^{-1}$

$Y_6(OH)_8(BTC)_2(HCOO)_4 \rightarrow 2\ Y(BTC)(H_2O) + 4/3\ Y(HCOO)_3 + 4/3\ Y_2O_3 + 2\ H_2O$

$\Delta H = -240.78\ kJ\ mol^{-1}$

$Y_6(OH)_8(BTC)_2(HCOO)_4 + 2\ H_2O \rightarrow 2\ Y(BTC)(H_2O) + 1/3\ Y(HCOO)_3 + Y_2O_3 + 5/3\ Y(OH)_3 + 3\ HCOOH$

$\Delta H = -223.68\ kJ\ mol^{-1}$

It is evident from the calculated enthalpies that the reactions yielding yttrium formate and/or yttrium oxide as by-products are more thermodynamically favorable and thus more likely to occur experimentally.

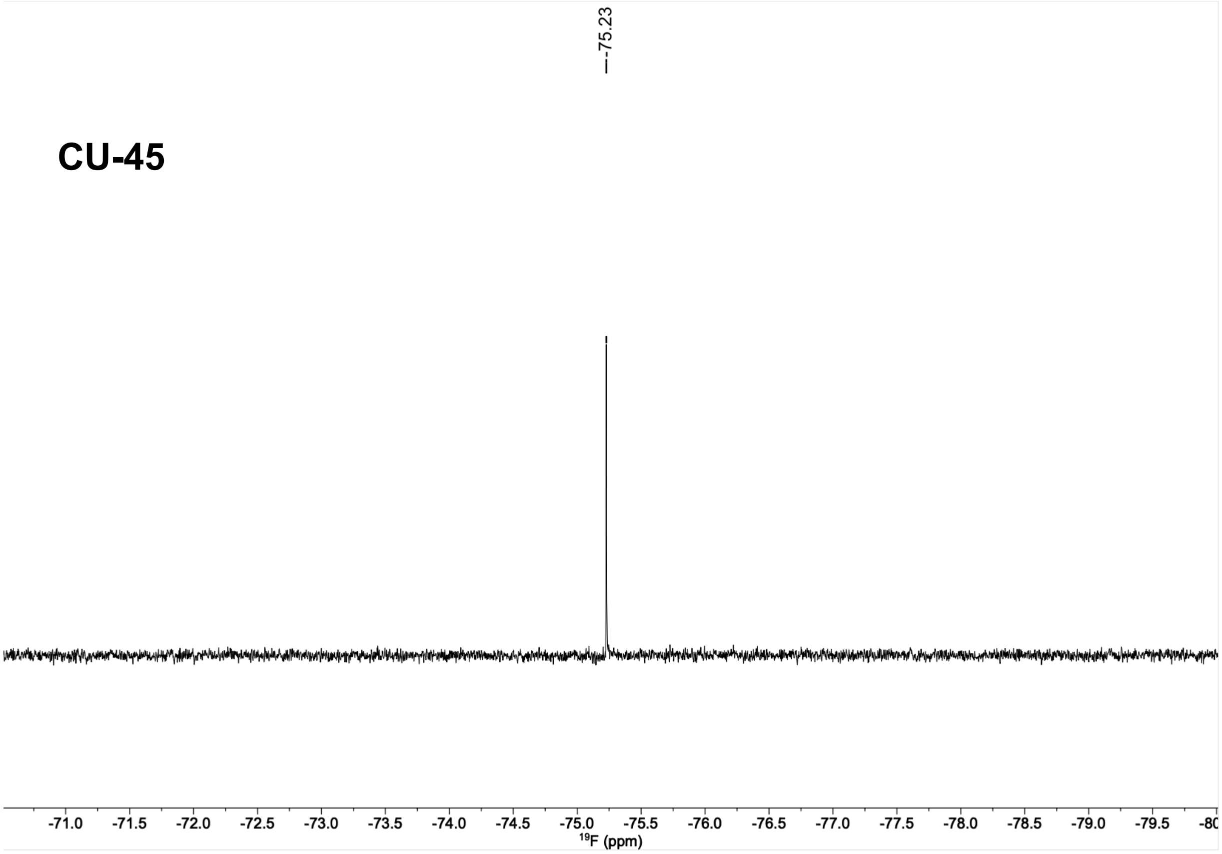

Figure A2.14. ^{19}F NMR of CU-45 triflouroacetic acid as capping ligand.

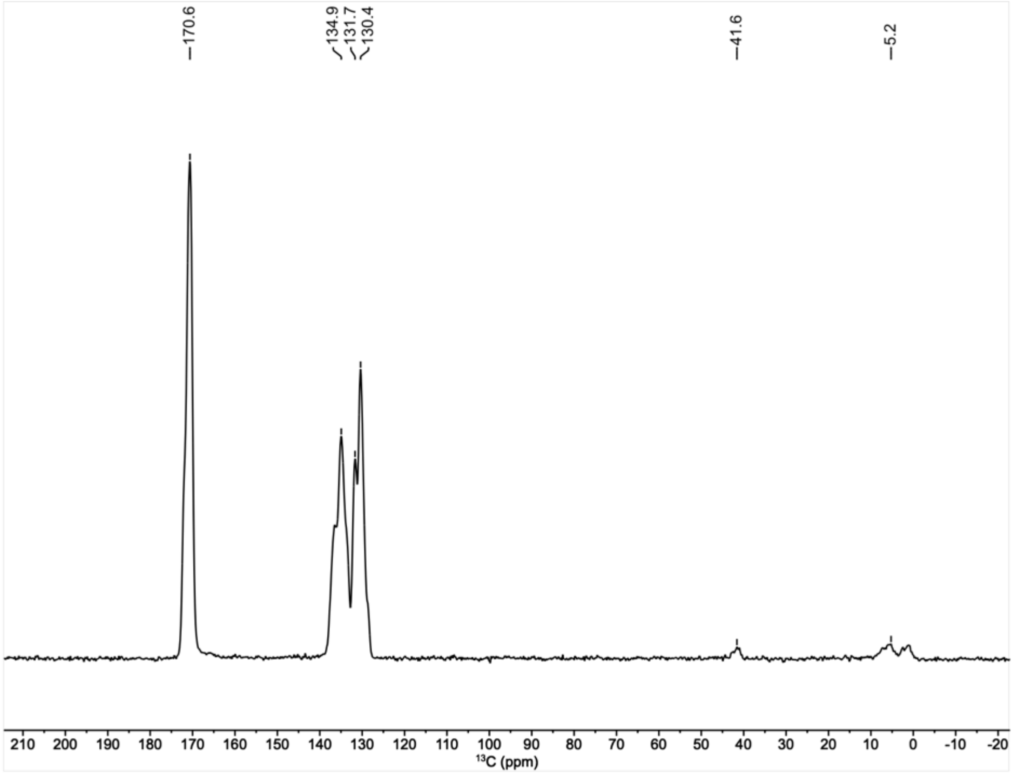

Figure A2.15. ^{13}C SS-NMR spectrum of H_3BTC linker.

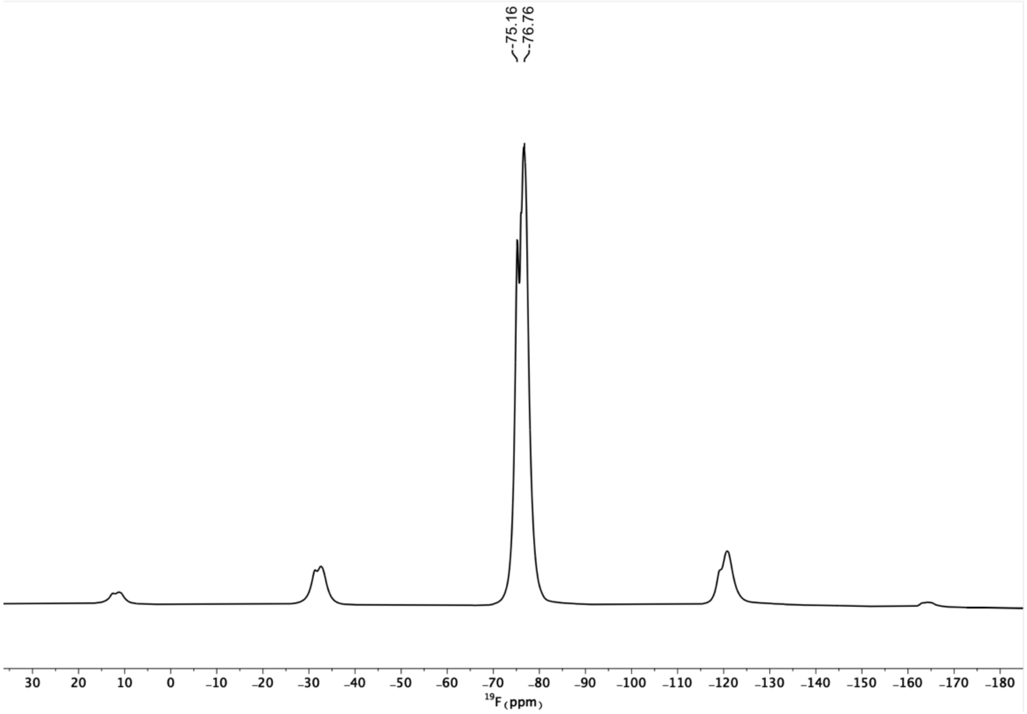

Figure A2.16. ^{19}F SS-NMR of Y(TFA)$_3$ spinning at 16.5 kHz.

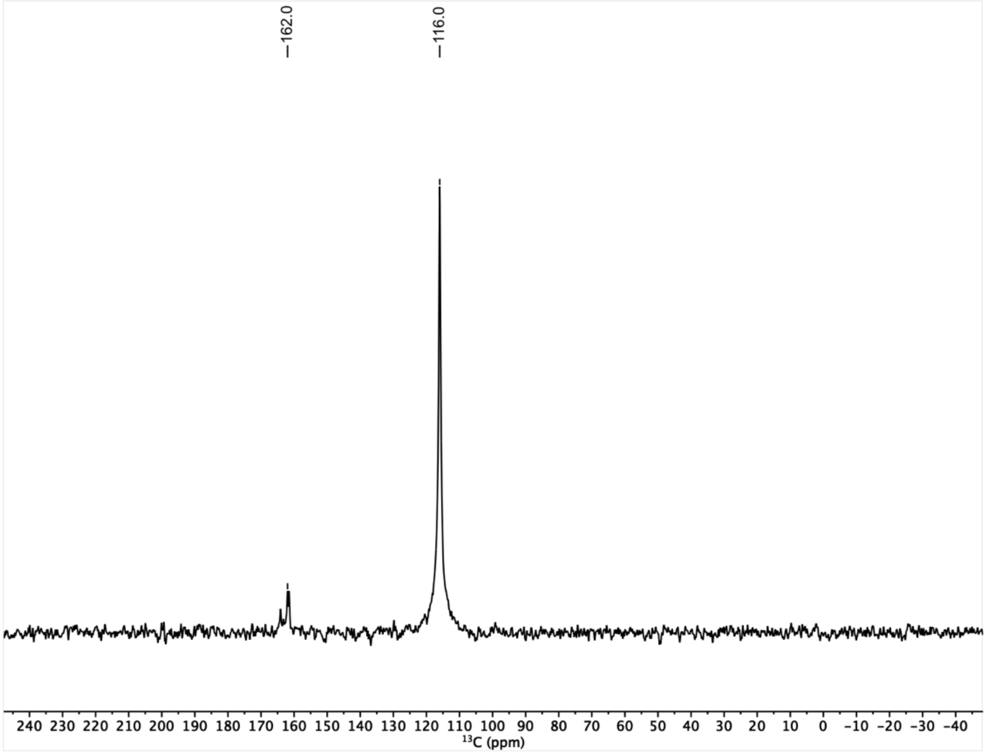

Figure A2.17. ^{13}C SS-NMR of Y(TFA)$_3$ cross-polarized from ^{19}F.

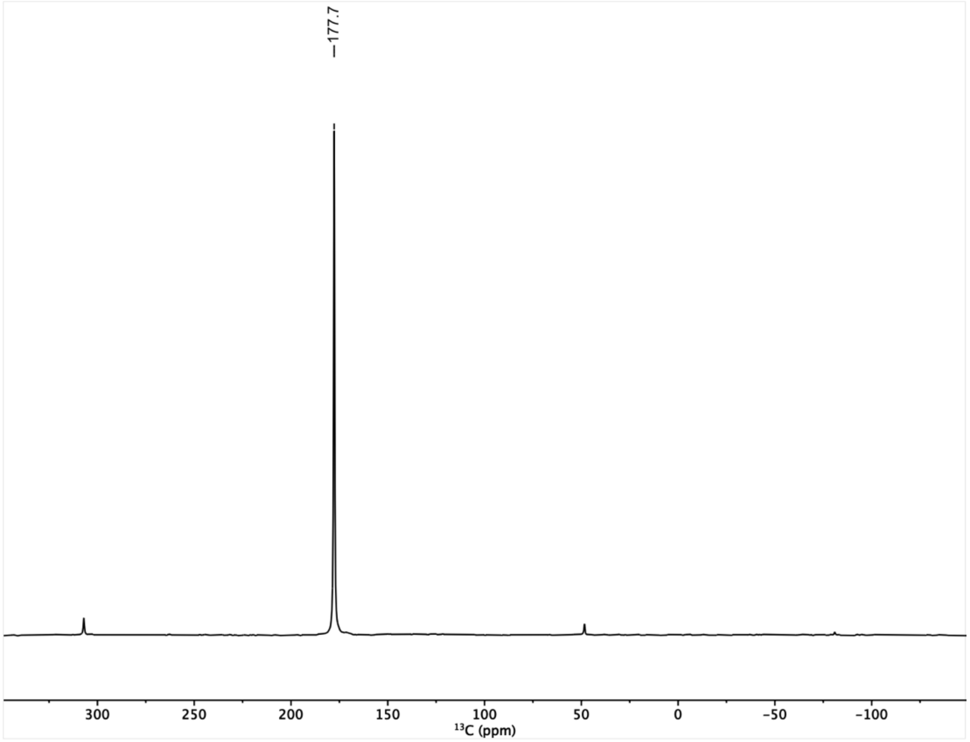

Figure A2.18. ^{13}C SS-NMR of $Y(HCOO)_3$.